TAMPEREEN TEKNILLINEN YLIOPISTO
TAMPERE UNIVERSITY OF TECHNOLOGY

TUOMAS KOSKINEN

ARTIFICIAL FLAW DETECTION WITH ULTRASOUND IN AUSTENITIC STAINLESS STEEL

Master of Science thesis

Examiner:
Assoc. Prof. Minnamari Vippola
Examiner and topic approved by the Faculty Council of the Faculty of Engineering Sciences
on 4th November 2015

ABSTRACT

TUOMAS KOSKINEN: Artificial Flaw Detection with Ultrasound in Austenitic Stainless Steel
Tampere University of Technology
Master of Science Thesis, 83 pages, 5 Appendix pages
February 2016
Master's Degree Programme in Materials Science
Major: Metallic materials
Examiner: Associate Professor Minnamari Vippola

Keywords: ultrasound, artificial flaw, defect, austenitic, stainless steel

Ultrasonic testing is the main tool to inspect and verify the structural integrity of the primary circuit components in nuclear power plants during in-service inspection. However, the in-service inspection is usually done in a short time during the outages in limited accessibility, which sets the need for efficient inspection procedure. Primary circuit components are made from austenitic stainless steel and designed mechanical integrity and corrosion resistance in mind. While material properties of austenitic stainless steel promote these aspects they reduce the capability of ultrasonic testing, due to scattering, diffraction and attenuation of ultrasound.

In order to validate an inspection method and to train inspectors, reference points are needed. However, there are not enough real flaws available to be used for these purposes. For this reason artificial flaws must be used. Artificial flaws must reflect same or similar reflection indication so it can be used as a reference point. Otherwise this could lead to a false indications or missing of real flaws during in-service inspection. Unfortunately ultrasonic testing is highly dependent on the geometry of the component, the type of the flaw and the material in which ultrasound propagates; therefore numerous artificial flaws are needed to cover all probable flaw types and locations.

The aim of this thesis is to study artificial flaws and acquire wider knowledge on ultrasonic indications of these flaws. Another objective is to conduct an experiment with an austenitic steel weld with electric-discharge machined (EDM) notches as artificial flaws. The results of the experiment are then compared to the results from CIVA simulation. The focus is on mechanical and thermal fatigue type of flaws and also EDM notch for artificial flaws. Mechanical and thermal fatigue flaws were selected due to their occurrence during the service life of a primary circuit. These flaws can also be produced in well controlled manner as well as the EDM notches.

TIIVISTELMÄ

TUOMAS KOSKINEN: Keinotekoisten vikojen havaitseminen ultraäänellä austeniittisessa ruostumattomassa teräksessä
Tampereen teknillinen yliopisto
Diplomityö, 83 sivua, 5 liitesivua
Helmikuu 2016
Materiaalitekniikan diplomi-insinöörin tutkinto-ohjelma
Pääaine: Metallimateriaalit
Tarkastaja: Associate Professor Minnamari Vippola

Avainsanat: ultraääni, keinovika, austeniittinen, ruostumaton teräs

Ultraäänitarkastusta käytetään ydinvoimaloissa pääasiassa primääripiirin rakenteellisen eheyden varmistamisessa määräaikaistarkastuksissa. Määräaikaistarkastukselle on yleensä varattu tiukka aikaraja ja tietyissä tilanteissa luotaaminen voi olla hankalaa tilanpuutteen takia. Tästä syystä tehokkaan tarkastussuunnitelman laatiminen on tärkeää. Primääripiirin komponentit on valmistettu austeniittisesta ruostumattomasta teräksestä ja suunnittelu on fokusoitu mekaaniseen ja korroosion kestävyyden optimointiin. Vaikka austeniittisen ruostumattoman teräksen materiaaliominaisuudet edesauttavat edellä mainittuja ominaisuuksia, nämä materiaaliominaisuudet ja erityisesti austeniitin rakenne haittaavat ultraäänitarkastusta sironnan, diffraktion ja vaimenemisen johdosta.

Jotta tarkastusmenetelmä voidaan pätevöidä ja kouluttaa tarkastajia, tarvitaan vertailuvikoja vertailukohteeksi. Ideaalissa tilanteessa vertailuvikoina käytettäisiin oikeita käytön aikana muodostuneita vikoja. Näitä vikoja ei kuitenkaan ole riittävästi edellä mainittuihin tarkoituksiin ja useimmissa tapauksissa komponentit voivat olla kontaminoituneita ja täten radioaktiivisia, jolloin komponentin puhdistus voi olla kallista tai jopa mahdotonta. Tästä syystä vertailuvikoina käytetään useimmiten keinovikoja. Keinovikojen tulee heijastaa ultraääntä samalla tai lähes samalla tavalla kuin todelliset viat, sillä vääränlaista vertailuvikaa käytettäessä saatetaan jättää todellinen vika huomioimatta tai tulkita olematon vika todelliseksi viaksi. Ultraäänitarkastuksen haittapuolena on kuitenkin sen riippuvuus komponentin geometriasta, vian tyypistä ja materiaalista, jossa ultraääniaalto etenee. Näistä riippuvuuksista johtuen keinovikoja tarvitaan paljon kattamaan laajasti eri vikatyypit ja niiden sijainnit komponentissa.

Tämän diplomityön tarkoitus on tutkia keinovikoja austeniittisessä teräksessä ja hankkia laajempaa tietoa ultraäänen käyttäytymisestä näissä vioissa. Tutkimusosiossa tarkastellaan austeniittista hitsiä, johon on koneistettu kipinätyöstöuria. Hitsin tarkastustuloksia verrataan CIVA-simulaatioon. Vikatyypeistä keskityttiin mekaanisen ja termisen väsymisen vikoihin, sillä ne ovat yleisimpiä vikatyyppejä ydinvoimalan primääripiirin komponenttien elinkaaren ajalla ja niitä voidaan valmistaa kontrolloidusti myös keinotekoisesti. Mitattavaksi keinoviaksi valittiin kipinätyöstöura sen helposti kontrolloitavan valmistuksen takia.

PREFACE

This master's thesis was carried out at VTT Technical Research Centre of Finland Ltd in Espoo as a part of SAFIR2018 WANDA -project and was part of Master of Science degree at Tampere University of Technology in Materials Science.

At first I want to thank VTT for this great opportunity to study NDT and especially ultrasonic methods and their use in nuclear power plants. Greatest lesson for me during these six months was that there is still an immense amount to learn on this subject.

Thank you, Minnamari Vippola for great instructions and comments, which gave me perspective during the writing of this thesis.

Thank you, Esa Leskelä, my instructor at VTT, for excellent advices, instructions and helpful comments to this thesis.

I would also like to thank, Tarja Jäppinen, Kari Lahdenperä, Jonne Haapalainen and other VTT employees for guiding and helping me with my questions.

Lastly I would like to thank all my friends and family for supporting me through my studies and my dear Iina who has believed in me and cheered me through this work.

Espoo, 24.2.2016

Tuomas Koskinen

CONTENTS

LIST OF FIGURES

LIST OF SYMBOLS AND ABBREVIATIONS

λ	wavelength
a	Amplitude
AISI	American Iron and Steel Institute
BCC	Body-Centered Cubic
BEM	Boundary Element Method
BTR	Brittle Temperature Range
CCC	Copper Contamination Cracking
dB	Decibel
DDC	Ductility-dip cracking
EBSD	Electron Back Scattering Diffraction
EDM	Electric discharge machining
EMAT	Electromagnetic Acoustic Transducer
f	frequency
FCC	Face-Centered Cubic
FDM	Finite Difference Model
FEM	Finite Element Model
GBS	Gaussian Beam Superposition
GTD	Geometrical Theory of Diffraction
HAZ	Heat Affected Zone
IASCC	Irradiation Assisted Stress Corrosion Cracking
ISI	In-Service Inspection
MGB	Migrated Grain Boundary
NDE	Non-destructive Evaluation
NDT	Non-destructive Testing
NPP	Nuclear Power Plant
PA	Phased Array
POD	Probability of Detection
SCC	Stress Corrosion Cracking
SGB	Solidification Grain Boundary
SNR	Signal-to-noise Ratio
SOV	Separation of Variables
SSGB	Solidification Subgrain Boundary
TOFD	Time-of-flight Diffraction
TRL	Separate Transmit-Receive Longitudinal wave probe
TRS	Separate Transmit-Receive Shear wave probe
v	Wave velocity
ZCC	Zinc Contamination Cracking

1. INTRODUCTION

Austenitic stainless steel is used in wide range of applications in nuclear power plants. The main reason for its use originates from its physical properties and the ability to resist different forms of corrosion. It also has good weldability thus allowing its very versatile use in a vast range of applications. In nuclear power plants, structural integrity of the weld must be monitored during the lifetime of the component. For this in-service inspection, ultrasonic methods are applied.

Unfortunately, the crystal structure of austenitic weld hinders the propagation of ultrasonic beam, causing deviation, attenuation and scattering. This is problematic, since it is often difficult to determine the size and the position of the possible flaw. In worst case scenarios flaws needed to be noticed may be completely undetected. This is why it is important to have mockups with known flaws, allowing the possibility to compare a possible flaw to a known flaw to estimate its size, shape and location. Real flaws are hard to come by and producing crack like artificial flaws may be difficult, time-consuming and expensive in some scenarios. Electric-discharge machined (EDM) notches offer cheaper and simpler way to mimic real flaws to some degree. Also ultrasonic simulation can be used as a supporting tool to validate these flaws and justify the inspection methods technically.

This thesis has been divided into a literature section and an experimental section. In the literature section, the focus was on austenitic stainless steel, ultrasonic inspection, simulation and artificial flaws. The agenda was to clarify the phenomena behind the difficulties of ultrasonic inspection in austenitic stainless steels and the simulation of ultrasound in these welds. In artificial flaws the focus was mainly on flaws which occur during the service life of components in nuclear power plants.

In experimental section, EDM notches of the same size were machined in and near the weld. The base material was AISI 316L stainless steel, which is widely used in nuclear power plants. The weld was scanned from both sides of the weld with two different linear phased array probes with shear wave probe, 2D matrix array TRL probe and two conventional shear wave probes. Lastly the weld was modelled in CIVA software and simulated with linear phased array scan and compared to the experimental results.

2. AUSTENITIC STAINLESS STEEL

Stainless steel is an iron-based metal alloy, which has a wide range of different kinds of applications. The word *stainless* comes directly from its property to resist corrosion in environments where typical ferritic steel would corrode. This property comes from the adding of chromium, which forms a thin chromium oxide film on the surface of the steel. Stainless steel can be divided into three types according to their phase, martensitic, ferritic and austenitic. There are also some special applications such as duplex stainless steel, which contains about 50% of austenite and 50% of ferrite. Precipitation hardenable stainless steels are considered as their own group as well. This chapter concentrates on austenitic stainless steel, which is one of the most common types of stainless steels. [1–3]

Austenitic stainless steel that contains at least 8 wt% of nickel and 18 wt% of chromium is also known as AISI300 series, which is the most widely used grade of stainless steel. It is known for its excellent resistance of corrosion, heat and creep. In addition, austenitic stainless steel has good fabricability and cold working properties due to the deformation induced martensitic transformation strengthening the steel. This type of stainless steel has an austenitic phase which has a face-centered cubic (FCC) crystal structure. It is also non-magnetic. [4–6]

Since the combination of these properties, austenitic stainless steels are widely used in nuclear industry. These applications are, such as primary circuits and the internal structures supporting the nuclear core. The wide use of austenitic stainless steel in the critical components of nuclear power plants (NPP) sets the need for wider understanding of the materials in order to develop precise and effective non-destructive testing (NDT) methods to assure the safe operation of NPPs. [7]

In the following chapters 2.1 – 2.5, austenitic stainless steel is discussed in more detail. First formation and crystal structure of austenite is explained and then the mechanical and chemical properties are discussed. Two steel grades, AISI 316 and AISI 321 are gone through in more detail and last welding and the flaws in the austenitic stainless steel welds are discussed.

2.1 Formation and crystal structure of austenite

Phase transformation of steel is a crucial process to understand when considering the following grain structure and the properties of the steel. Phase transformation usually takes place when sufficient heat is applied to the steel followed by cooling down in a

certain time, such as manufacturing and welding of the steel. Welding for instance, plays a vital role in joining austenitic stainless steel pipes in NPPs. [8]

Typical steel in normal room temperature is in ferrite phase which is also called the α-phase. This phase has a body-centered-cubic (BCC) crystal structure. On the other hand, austenitic stainless steel has an austenitic phase, referred as the γ-phase. This γ-phase has a FCC crystal structure and it is normally unstable in room temperature, leading to its phase transformation to ferrite. To prevent this phase transformation, alloying elements need to be added in order to retard the kinetics of the $\gamma \rightarrow \alpha$ transformation thus making γ-phase stable or metastable in room temperature. [6,9]

As mentioned above, austenite has a FCC structure, which can be seen in Figure 1. Ferrite's crystal structure, BCC, can be seen in Figure 2. When comparing these two crystal structures it can be noted that in phase transformation, there needs to be a volumetric change. This change is about 1%, which can cause internal stresses during the γ to α transformation. [10]

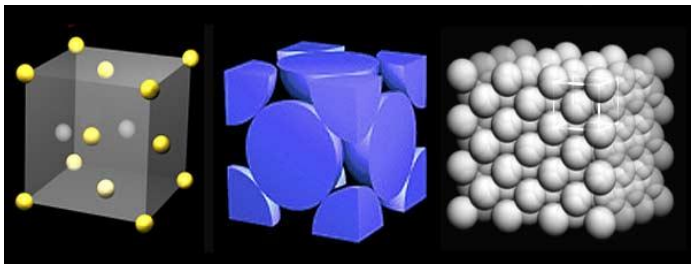

Figure 1 FCC [11]

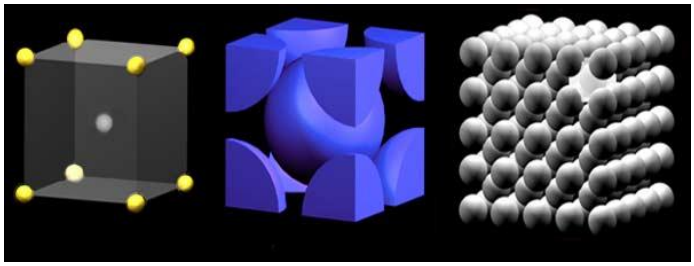

Figure 2 BCC [11]

The BCC structure is more loosely packed compared to the FCC structure and largest cavities are tetrahedral cavities between the connecting corner atoms and the center atom. On the other hand, in the FCC structure largest cavity is shaped as an octahedron and it is slightly larger than the tetrahedral cavity in the BCC structure. These cavities can be seen in Figure 3. The size of the cavity determines the maximum size of the interstitial atom that can fit into the lattice structure. Therefore these cavities limit the elements which can be used as alloying elements. [10]

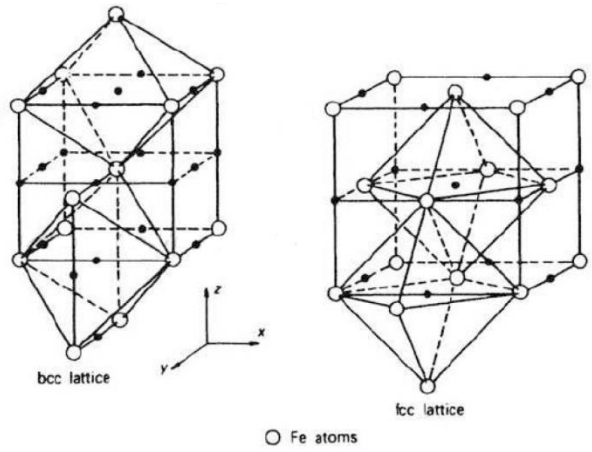

Figure 3 Volumetric cavities [10]

Since there are a number of alloying elements influencing the phase transformation, it is usually simplified to iron binary equilibrium diagram. This phase diagram plots temperature against the relative concentration of carbon. This kind of phase diagram shows the threshold field in which certain phase is in stable condition. This leads to the observation that alloying elements can either expand or contract the γ-field. The elements expanding the γ-field, hence favoring the austenitic phase, are called γ-stabilizers and the elements contracting this field by favoring the ferrite phase are called α-stabilizers. [9]

The form of the field in the diagram is determined to some degree on the electronic structure of the alloying element. Nickel, manganese and cobalt initiate open form of the γ-field in the phase diagram. Especially both nickel and manganese added in high concentrations completely eliminate the BCC α-iron phase replacing it with the austenitic γ-phase. These two elements change the kinetics of γ- to α-phase transformation enough for γ-phase to be stable in room temperature. Also obtaining metastable austenite by quenching from γ-phase to room temperature is easier with nickel and manganese as alloying elements. The γ-field can also be expanded with carbon and nitrogen, where the γ-field has grown but is limited by compound formation. This effect is broadly used in heat treatments of steel to obtain a homogenous solid solution. [9]

Closed and contracted γ-fields are caused by alloying elements restricting the formation of the γ-phase. These elements are usually strong carbide formers such as titanium vanadium, molybdenum and chromium. Silicon, aluminum, beryllium and phosphorous are ferrite formers, which function similarly to the strong carbide formers, closing the γ-field as well. When the γ-field is contracted to a small closed area, it is usually referred as the gamma loop. This gamma loop can be seen in Figure 4. A_3 is the temperature in which BCC ferrite transforms to FCC austenite and A_4 is the temperature in which FCC austenite transforms back to BCC ferrite. [9,10]

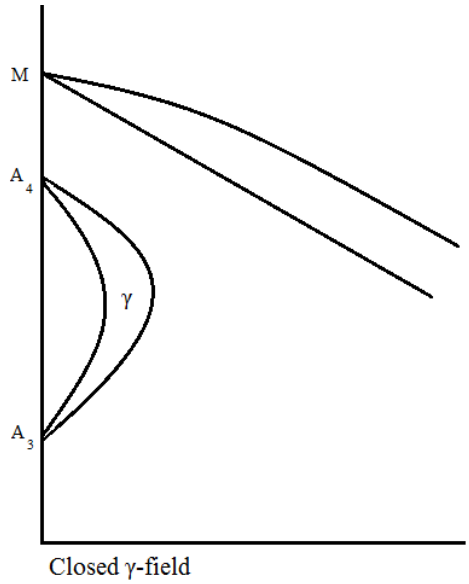

Figure 4 Gamma loop [9]

Thermodynamically this can be explained by calculating the enthalpy change ΔH, which describes the heat absorbed when a unit of solute is dissolving in γ-phase H_γ minus the heat absorbed when a unit of solute is dissolving in α-phase H_α. Thus $\Delta H = H_\gamma - H_\alpha$. This enthalpy change can be used with fractional concentrations of an alloying element when following relation holds:

$$\frac{C_\alpha}{C_\gamma} = \beta e^{\frac{\Delta H}{RT}}, \quad (1)$$

where C_α and C_γ are the fractional concentrations and β is a constant. [9]

2.2 Properties of austenitic stainless steel

2.2.1 Mechanical properties

Austenitic stainless steel has a wide variety of applications such as chemical processing, food processing and welding construction. Mechanical properties of austenitic, ferritic and martensitic stainless steel can be seen in Table 1.

Table 1 Mechanical properties of stainless steels; 409 is ferritic, 410A is martensitic and 304 and 316L are austenitic [2]

AISI number	Tensile Strength (MPa)	Yield Strength (MPa)	Ductility (%EL in 50mm)
409	380	205	20
410A	725	415	20
304	515	205	40
316L	485	170	40

Compared to other stainless steels, austenitic is more ductile than martensitic and ferritic stainless steels. In yield and tensile strength, austenitic has better tensile strength but slightly lower yield strength on average than ferritic. Martensitic has the highest value for tensile and yield strength but it lacks in ductility. Because of these mechanical properties austenitic stainless steel is fairly easy to work, thus making it the most common type of stainless steel in use. [2]

2.2.2 Chemical properties

One of the main properties for austenitic stainless steel is its resistance to corrosion. This resistance comes from the thin chromium oxide layer on the surface of the steel. However, this chemical process only happens in an atmosphere containing oxygen. Regardless stainless steel can corrode depending on the circumstances and the types of corrosion. Typical ways for stainless steels to corrode are pitting, stress corrosion cracking (SCC) and intergranular corrosion. [6]

Pitting corrosion is caused by localized depletion of chromium in an environment containing even small amounts of chloride. This forms a small pit which starts to corrode as an anode with significant rise in current density. This attracts chloride anions leading to acidifying the pit and formation of highly localized and corrosive environment. For first generation NPPs, the heat-transfer tubes in the steam generator were made from austenitic stainless steel. However, the environment was highly susceptible to pitting corrosion along with stress corrosion cracking, due to high temperature and pressure. The alloy of these components was changed to a nickel based Alloy 600. [12,13]

SCC needs favourable environmental conditions and tensile stress to form. It is important to note that even the residual stresses and stresses from uneven contraction and expansion from thermal changes may be sufficient to trigger SCC. These can be prevented with reduction of external loads or with heat treatments to remove residual stresses. Since either the environment or the tensile stresses can be controlled, SCC should be easily controlled. However, in NPPs it can cause problems in certain situations. In high neutron irradiation conditions, austenitic stainless steel is susceptible to irradiation-assisted stress corrosion cracking (IASSC), which is a special form of SCC in NPPs. Especially Si segregation from radiation induced segregation has been shown to contribute to IASCC. [7,14]

Intergranular corrosion occurs along the grain boundaries of the alloy. Stainless steel becomes susceptible to intergranular corrosion when it is heated around 500 - 800 °C for a long enough time. For example, welding can cause this kind of heat input. This forms chromium carbides along the grain boundary thus preventing the distribution of chromium evenly and causing depletion of chromium in the vicinity of the grain boundaries. This phenomenon can be seen in Figure 5. When there is not enough chromium to form the CrO -layer, stainless steel becomes vulnerable to intergranular corrosion. Since

sensitizing can happen during welding, there are no specific places for this type of corrosion to occur in an NPP. When the weld is done according to the appropriate procedure, this process can be avoided. [14]

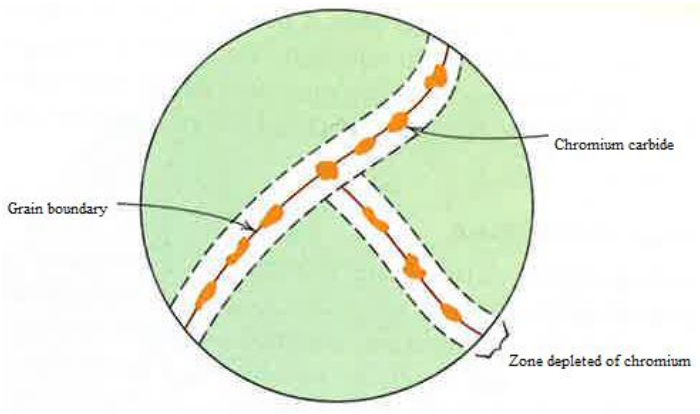

Figure 5 Chromium depletion in a grain boundary [14]

2.3 Specific austenitic stainless steel grades

In AISI grades, the 300 series is specifically for austenitic stainless steel. Since austenitic stainless steel is the most common type of stainless steels only the most relevant of its grades to this topic will be discussed.

2.3.1 AISI grade 316

Alloy AISI 316 (EN 1.4401) possesses a good corrosion resistance and can maintain its strength also in high-temperature environments such as in NPPs. These properties are due to the high amounts of alloying elements within the stainless steel. Alloy 316 also contains molybdenum which increases pitting corrosion resistance. Other versions of this grade are 316L (EN 1.4404), in which the L stands for lower carbon content and 316N (EN 1.4406) where the N states that nitrogen is added as an interstitial to the alloy. For alloy 316L lower carbon content is especially advantageous in welding applications, since it lowers carbide precipitation during welding. Composition for 316 grade can be seen in Table 2, however it can vary slightly depending on the steel manufacturer. [15,16]

Table 2 Composition of 316 in wt% [17]

C	Si	Mn	P	S	Ni	Cr	Mo
≤ 0,08	≤ 1,0	≤ 2,0	≤ 0,045	≤ 0,03	10,0-14,0	16,0-18,0	2,0-3,0

2.3.2 AISI grade 321

Grade 321 (EN 1.4541) has very similar properties to grade 316, but preventing carbides from precipitating is achieved with titanium instead of molybdenum. Titanium also improves the temperature properties of this alloy. Typical uses for this grade are high-temperature and corrosive environments like oil refinery components and welded pressure vessels. Composition of this alloy can be seen in Table 3, the titanium content is at least five times the carbon and nitrogen content but maximum of 0,7 wt%. [18]

Table 3 Composition of 321 in wt% [17]

C	Si	Mn	P	S	Ni	Cr	Ti
≤ 0,08	≤ 1,0	≤ 2,0	≤0,045	≤0,03	9,0-12,0	17,0-19,0	5(C + N) min., 0,7 max

2.4 Welding of austenitic stainless steel

Most common ways to weld austenitic stainless steels are fusion welding and resistance welding. In fusion welding heat is applied through the electrode and the welded metal. In resistance welding heat is applied through the electric current flowing through the welded parts and pressure is applied to the welded joint by the electrodes. Even though austenitic stainless steel can be readily welded with resistance welding, it is not very suitable for piping welds. Thus, fusion welding is discussed in more detail in this chapter. [19]

In fusion welding the idea is to deposit a small amount of molten steel between the parts to be joined. When it solidifies it welds the two parts together. There are a lot of variables affecting the weld result, which makes welding susceptible to different kinds of flaws and cracks when welding process is done incorrectly. Most austenitic stainless steels are considered to have a good weldability and it is also possible to use a wide range of different welding methods like with any stainless steel. Austenitic stainless steel has 50% greater thermal expansion rate than carbon steel, hence it may cause unwanted stresses if not taken account for when heat is applied during welding process. Compared to carbon steel, lower current can be applied, since the resistivity of stainless steel is higher. [8,20,21]

2.4.1 Solidification and crystal structure of welds

Weld area can be divided into three zones: fusion zone, heat affected zone (HAZ) and unaffected base material. Fusion zone is the area of the weld wherein actual melting, solidification and joining happens. HAZ is the zone where the heat from the fusion welding affects the microstructure. The size of the HAZ is affected by the heat from

welding process thus the size of the area is dependent on the welding speed and heat input in general. [22]

The microstructure of the weld is dependent on the solidification behavior of the fusion zone and then it is influenced by solid-state transformations. The fusion zone can solidify in austenitic stainless steels by two ways, either primary ferrite or primary austenite. After solidifying the microstructure is heavily affected by cooling rate and composition which drive the phase transformation. [22]

In primary austenite solidification, resulting microstructure can either be fully austenitic or austenitic with ferrite at cell and dendrite boundaries. In latter case, ferrite forms at the end of austenitic solidification process as a eutectoid reaction. However, this reaction requires large enough quantity of elements such as Cr and Mo to promote the ferrite formation. Comparison between fully austenitic and primary austenite with ferrite in cell and dendrite boundaries can be seen in Figure 6 and Figure 7 respectively. [22]

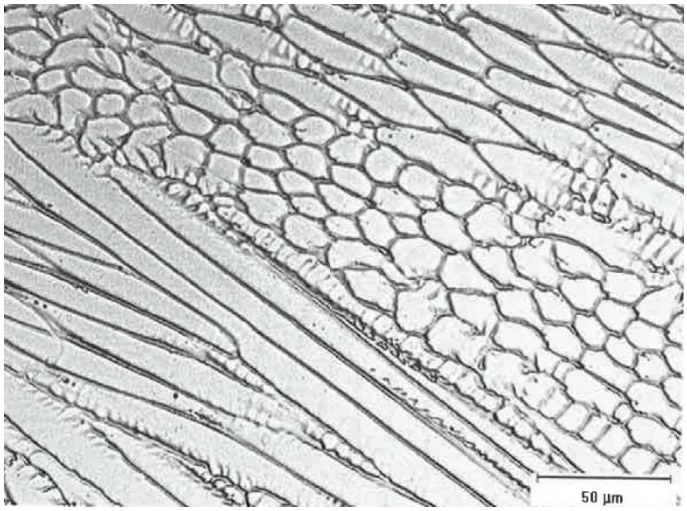

Figure 6 Fully austenitic fusion zone [22]

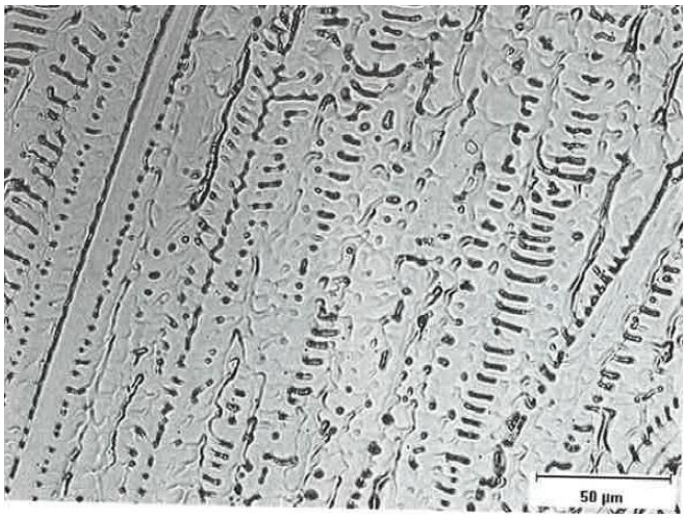

Figure 7 Primary austenite, ferrite at cell and dendrite boundaries [22]

As the solidification occurs as primary ferrite, austenite forms at ferrite solidification boundaries via peritectic-eutectic reaction. The amount of austenite is defined by Cr_{eq}/Ni_{eq} and the cooling rate of the weld. As the fusion zone cools down through the delta ferrite and austenite field, austenite consumes ferrite via diffusion-controlled reaction. This can lead to formation of skeletal ferrite where ferrite to austenite transformation has driven ferrite-promoting elements to ferrite phase and the temperature is low enough to retard the diffusion of austenite-promoting elements. [22]

Solidification as completely ferrite is fairly rare in austenitic stainless steels. Also the most of the filler metals are composed in a way to promote the primary ferrite and austenite formation. [22]

2.5 Possible flaws in austenitic stainless steel welds

To get a better understanding of the flaws present in austenitic stainless steel welds it is beneficial to comprehend the interfaces within these welds. Lippold and Damian divide these boundaries into three types: solidification subgrain boundaries (SSGB), solidification grain boundaries (SGB) and migrated grain boundaries (MGB). SSGB has low dislocation density due to solidification along the preferred crystallographic direction. SGB on the other hand has dissimilar growth direction and orientation. This leads to high angular misorientation, thus dislocation network develops along the SGB. In MGB, the high angular grain boundary has migrated away and it uses grain growth as its driving force. MGBs are most typical in fully austenitic welds since ferrite usually prevents migration away from original SGB. [22]

Weldability of austenitic stainless steels is generally good. However, like any other steel, there exist a few problems which may occur during and after welding. These are solidification cracking, HAZ and weld metal liquation cracking, ductility dip cracking, reheat cracking and corrosion and contamination induced cracking. Although austenitic stainless steel has good corrosion resistance, welding may expose it to certain types of corrosion. [20]

2.5.1 Weld solidification cracking

For austenitic stainless steels, weld solidification cracking is one of the most typical types of flaw. According to generalized theory, this type of cracking occurs when continuous liquid films separate grains in combination with high enough tensile stresses. Welds that are primary austenite and contain no ferrite are the most prone to weld solidification cracking. Also high impurity levels, such as S and P, increase the susceptibility for this kind of cracking. Welding process itself has an influence on cracking tendency. Heat input, travel speed and weld bead shape affect the susceptibility, since residual tensile stresses can cause cracking when weld metal contracts during cooling. For example high heat, too fast travel speed and concave bead shape raise the probability to

weld solidification cracking. However composition and most importantly Cr_{eq}/Ni_{eq} relation has the strongest influence on weld solidification cracking. This is related to the fact that Cr is ferrite promoting element and ferrite lowers the probability of solidification cracking. Weld solidification crack in fully austenitic weld can be seen in Figure 8. Weld solidification cracks usually form in SGBs. Since there is no residual ferrite, these grain boundaries tend to be straight so there are no resisting factors for crack propagation. [20,23]

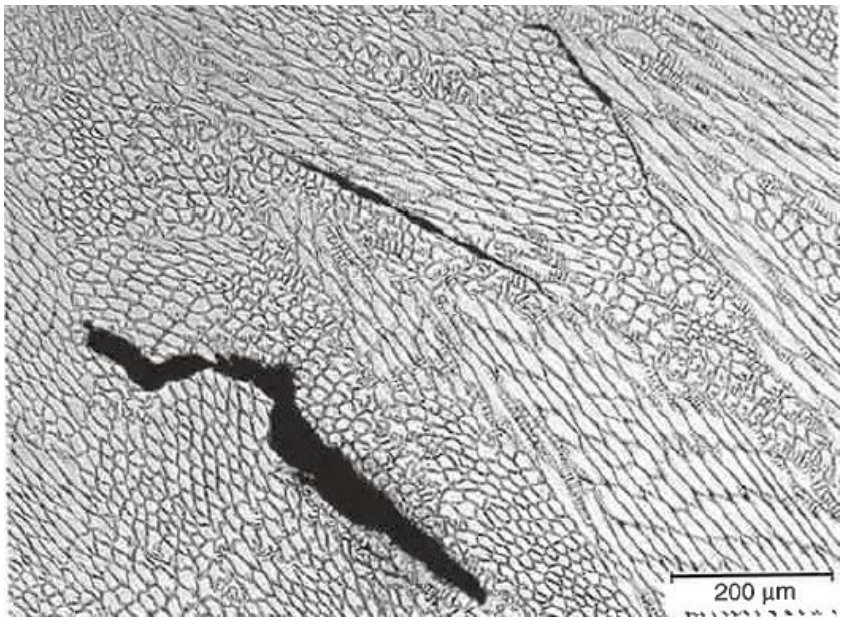

Figure 8 Fully austenitic weld crack [20]

Since solidification cracks form along SGBs or SSGBs fracture surface reminds more of a dendritic structure. Flat crack shape is possible in fully austenitic welds mainly due to the straight shape of the boundary. These cracks form in the temperature range between liquidus and solidus temperature, which is called brittle temperature range (BTR). [20]

2.5.2 HAZ liquation cracking

On the boundary between fusion zone and HAZ there is a partially melted zone. HAZ liquation cracking occurs when liquid films form along the grain boundaries in a partially melted zone. The reason for liquation is usually caused when impurities segregate to the grain boundary. Like weld solidification cracking, HAZ liquation cracking occurs also in the range of BTR. [20]

2.5.3 Weld metal liquation cracking

Weld metal liquation cracks are also called microfissures or microcracks. These cracks are hard to detect due to their small size. Microfissures are usually formed in fully austenitic multipass welds, during remelting and solidification of MGBs. Temperature

range is in BTR. The difference to solidification cracking is that in liquation cracking fracture surface does not form dendritic morphology. [20]

2.5.4 Ductility-dip cracking

Ductility-dip cracking (DDC) occurs along MGBs in alloys which have FCC crystal structure. In DDC there is sudden drop in ductility slightly above the half of the melting temperature of the material whereas in normal situation ductility would gradually increase till solidus temperature. Highly restrained and thick welds are the most susceptible for DDC. Research made by Nissley et al. by using strain-to-fracture test pointed out that the susceptibility to DCC is related to temperature, strain and to some extent, stroke rate. Also recrystallization was previously proposed as a recovery mechanism for ductility at higher temperatures. However the mechanism behind DCC is not yet fully understood. [20,24]

2.5.5 Reheat cracking

Reheat cracking takes place usually during stress-relief heat treatment. Fortunately this is not usually problematic for most of the austenitic steel grades but for steels that form carbides during the heat treatment. These are usually heat resisting steels with slightly higher carbon content. [20]

Heat input from welding dissolves carbides into high temperature HAZ. When the weld is reheated in stress relieving, carbides precipitate into the grain. When stress is relieved, but interior of the grain is still overly strengthened due to carbides, reheat crack occurs. [20]

2.5.6 Corrosion induced cracking

Corrosion resistance of austenitic stainless steel was discussed in chapter 2.2.2 Chemical properties. These same properties apply also to the welds of austenitic stainless steel. They are susceptible to intergranular corrosion, sensitization, stress corrosion cracking and pitting like the base metal [25]. Here the special cases in weld corrosion, knifeline attack and selective ferrite attack will be discussed in more detail.

Knifeline attack is a special case of intergranular attack. The weld appears to be cut with a knife adjacent to fusion zone. This is due to carbides dissolving into the region. However, when temperature drops chromium carbides form faster than the other carbides, forming a sensitized region. [25]

In selective ferrite attack, substance such as terephthalic acid, corrode the ferrite in stainless steel. This reaction corrodes ferrite network from the weld thus causing serious damage to structural integrity of the weld. [25]

2.5.7 Contamination induced cracking

Contamination induced cracking occurs when contaminant enters the grain boundary of austenitic stainless steel. Lippold and Damian define three types of contamination cracking: copper contamination cracking (CCC), zinc contamination cracking (ZCC) and helium-induced cracking. [20]

CCC occurs when molten copper penetrates into the grain structure from the surface of the stainless steel. However, copper as an alloying element does not cause this kind of cracking. Wetting of the grain boundaries is important for this phenomenon to happen, which is most effective close to 1100 °C. Thus CCC can be observed just next to the fusion boundary. [20]

ZCC is similar to CCC but in contrast to CCC zinc penetrates the grains, according to Lippold and Damian, by evaporation or by condensation. Reason for this may be the melting temperature of the zinc which is only 419,5 °C and boiling temperature 906 °C, compared to the melting temperature of copper 1083 °C. [20]

Helium-induced cracking is a special case. Helium forms inside the steel due to neutron-irradiation. Helium is the emitted alpha particle from the resulting neutron capture and decay of ${}^{12}_{5}B$ or ${}^{59}_{28}Ni$ isotopes. Since helium cannot dissolve into steel very well, it forms bubbles and other impurities into the grain boundaries, which induce a crack when a proper amount of stress is applied. [20]

3. ULTRASONIC EXAMINATION

A bat is most renowned for its ability to navigate with ultrasound. In nature ultrasound is used besides navigation also for communication. In both of these situations the animal has to take into account the same problems that are faced in the ultrasonic inspection as well; attenuation, scattering and distortion. However, using ultrasound is very advantageous in situations where normal sight is obstructed or there is high audible background noise. Ultrasonic examination is based on an idea to send ultrasonic sound waves to the material to examine the signal which has reflected or diffracted from a surface or a discontinuity. The other way is to examine the transmitted signal. [26,27]

As an examination method, ultrasound has lots of options so it is fairly versatile. The inspector can use large variety of ultrasonic transducers depending on the desired application. Also it is possible to use the shape of the part in advantage and to use reflections in a way that the ultrasound can reach the desired area in the right angle. There are a lot of options for the coupling medium and it is also possible to automatize the process in certain applications. Ultrasonic examination is a cost effective and fast method, however it requires skilled operator for qualified use and it is hard to interpret with high accuracy. [27,28]

In the chapters 3.1 - 3.4 is discussed the theory behind ultrasonic testing, how ultrasound is generated in the ultrasonic transducers, how welds are inspected with ultrasound and how austenitic stainless steel is inspected with ultrasound.

3.1 Theory behind ultrasonic testing

Ultrasound is a mechanical wave like any other sound. The most classical way to describe the wave motion is a rock dropped in water. The surface of the water is disturbed and the waves move outwards from the disturbed point. This disturbance is transmitted from particle to particle so the wave propagates. However, the particle returns to its equilibrium position after transmitting, thus the net motion of particles is zero so only the energy is transmitted forward. Since the particles transfer the energy from one to another there needs to be a medium for this propagation to happen. [29,30]

The velocity of the propagation depends on the density of the medium. In steels, the grain size affects the density, hence it affects the velocity of the sound wave as well. The denser the medium the faster is the transmission. For example speed of sound in austenitic stainless steel is approximately 5672 m/s with 120 µm grain size. For comparison, in the air the wave velocity is approximately 330 m/s. [30,31]

Wavelength λ can be defined as the distance between two corresponding points in the waves. Amplitude a is the maximum displacement from the equilibrium position and velocity v determines how fast the energy propagates through the medium. Frequency f is the reciprocal of the period T, hence $f = 1/T$. These all are related together by the formula below. [30]

$$\lambda = \frac{v}{f} \tag{2}$$

Ultrasound is type of sound which has higher frequency than the hearing of the human ear. Hence all frequencies over 20 kHz are considered as ultrasounds. The intensity (amplitude) of a sound wave is determined by decibels (dB). Decibel is a logarithmic scale relative to human hearing threshold of 1 kHz. [30]

3.1.1 Wave form

Wave form can be categorized into longitudinal wave and transverse wave. In a longitudinal wave (or compressional wave), the wave propagates parallel to the direction of the disturbance. The disturbance vibrates in a way it compresses the particles into the direction which the wave will propagate, resulting in compression and rarefaction regions. This is demonstrated in Figure 9. In this figure v is the wave velocity. [29,30]

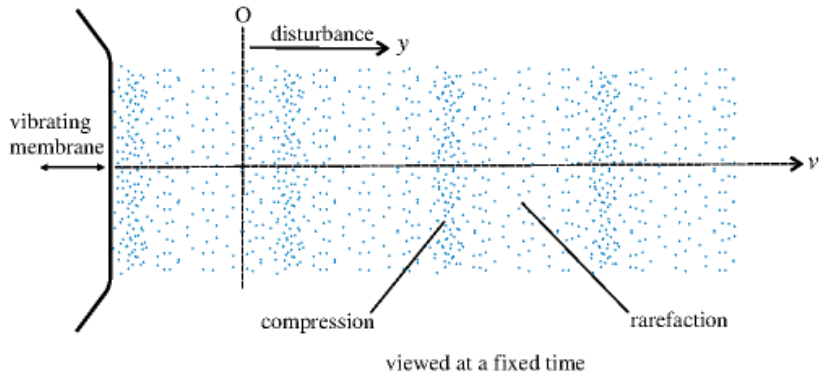

Figure 9 Longitudinal wave [29]

Unlike in longitudinal wave, the disturbance from equilibrium in transverse wave (or shear wave) is perpendicular to the propagation direction. As seen in Figure 10 the disturbance can be also negative from the equilibrium. This is different from longitudinal wave, since there is no compression or rarefaction in transverse wave. Sound velocity of a transverse wave is approximately half of the velocity of a longitudinal wave in the same material. This can be used as an advantage to increase resolution, since when velocity slows down, but frequency stays the same, the wavelength shortens. This allows the detection of smaller flaws.[29,30,32]

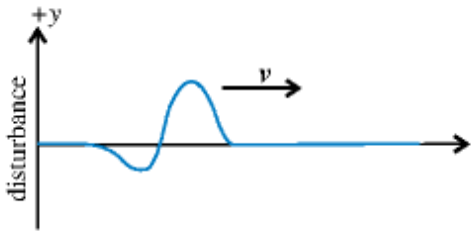

Figure 10 Transverse wave [29]

A special case for transverse wave is a surface wave (or Rayleigh wave). It is generated through a mode conversion when the waves reflect in a certain angle. [33]

3.1.2 Reflection of sound waves

According to Huygens' principle: "each point on a wavefront can be considered as a point source which is responsible for the subsequent progress of the wave". These point sources on the original wavefront generate secondary wavelets, which produce a new wavefront. Mansfield uses this principle to derive the laws of reflection and refraction. [29]

In Figure 11 the reflection of sound waves in a surface is demonstrated. According to Mansfield, the law of reflection is: "The angles of incidence and reflection of waves which are incident on a plane surface are equal, with the reflected waves propagating in the plane which is defined by the incident wave and the normal to the reflection surface at the point of incidence." This means that when a point from the wavefront BA reaches the plane surface AC it produces a secondary wavelet. These secondary wavelets produce a reflected wavefront CD. Since the waves are traveling in a same medium thus they have the same velocity, triangles BAC and DCA are congruent. This means that the incident wave angle θ_i and reflected wave angle θ_r are the same. [29]

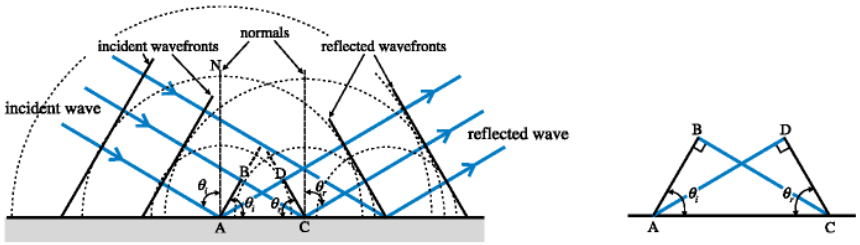

Figure 11 Reflection of a wave at a surface [29]

As seen in Figure 12, the secondary wavelets are produced at the interface between two mediums. These secondary wavelets continue to propagate in the second medium. However, the velocity is different between the two mediums so the travel distance is shorter in the other medium in the given time. This causes the wave to refract according to Snell's law: [29]

$$\frac{\sin\theta_1}{v_1} = \frac{sin\ \theta_2}{v_2} \quad (3)$$

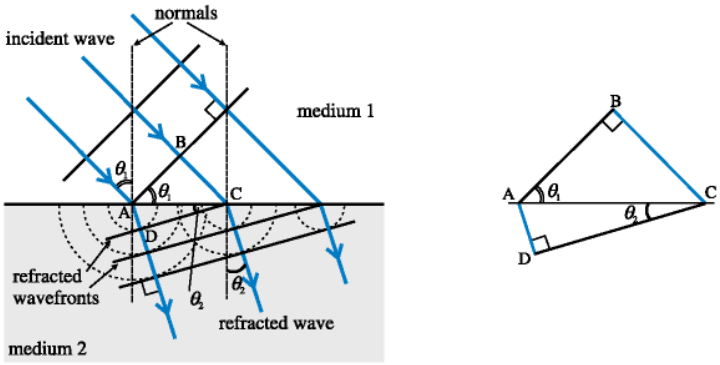

Figure 12 Refraction of a wave between two mediums [29]

At the boundary of medium 1 and medium 2 a component of originally transmitted longitudinal is converted into a shear wave. It must also be taken into account that longitudinal wave has greater velocity than shear wave. Therefore there is an angle in which longitudinal wave has a refraction angle of 90° and it does not penetrate into the material. However shear wave does, due to its lower velocity. This incident angle is called the first critical angle and it can be used when only shear wave is desired in the inspection. [32]

The second critical angle is the incident wave angle for shear wave when its refraction angle is 90°. At this case no sound wave is penetrated into the material. When there are no critical angles, both shear wave and longitudinal wave refract into the second medium as seen in Figure 13. [32]

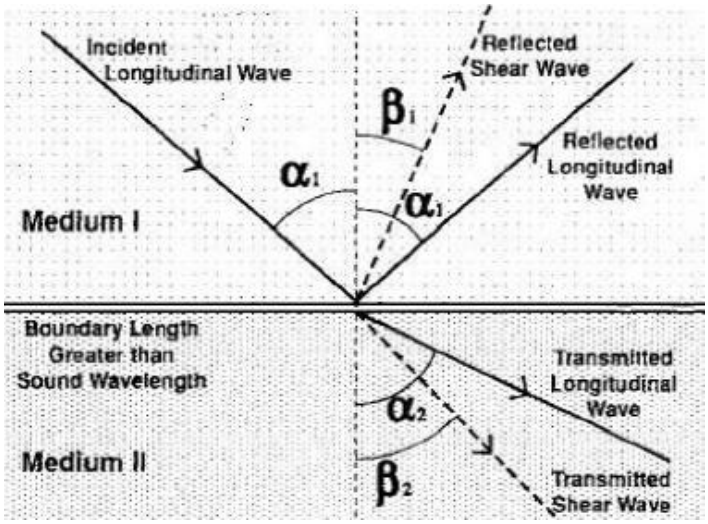

Figure 13 Wave mode conversion [32]

At the second critical angle mainly with solid-gas and solid-liquid interfaces Rayleigh waves are produced. These waves decay rapidly toward the interior of the material (z-direction) as seen in equation 4.

$$u_z = A_3 e^{-\propto z} \cos(ky - \omega t) \quad (4)$$

In this equation, A_3 is the amplitude of the displacement field, $\propto$ the attenuation factor, k the wave number and ω the angular frequency. However Rayleigh waves propagate along the surface of the body fairly easily. These surface waves are mainly transverse thus surface wave is rather a special case of shear wave, also the wave velocity is slower than the normal shear wave. These surface waves can be used in the NDT inspection to scan the surface. [32,33]

3.1.3 Attenuation of ultrasound

The intensity of ultrasound decreases with the distance from the transducer. This intensity loss happens when the wave is absorbed, scattered or spread. Also the geometry and acoustic beam divergence affect the attenuation of ultrasound. [34–36]

In monocrystalline structure absorption from internal friction and thermal conductivity is the most common reason for attenuation. However, in polycrystalline structure, scattering is the major reason for attenuation. Unlike in the case of absorption, amplifying the signal in order to compensate the attenuation from scattering causes the increase in the noise levels. This is due to the fact that when amplifying the signal, the receiver picks up also the scattered waves. [35]

Scattering occurs at different acoustic boundaries. These boundaries are formed mainly from the change of density or elastic moduli. Grain boundaries within the steel are a good example of these kinds of boundaries. Size relation between the grain and wavelength affect the attenuation, thus probe frequency affects the attenuation as well. When the wave length is larger than the grain diameter attenuation is considerably lower. However, this also means that smaller flaws get missed since the sensitivity goes down as well. This can be compensated by using shear waves, so the wavelength lowers. [37]

Anisotropic materials, such as austenitic welds, deform the acoustic beam due to the different direction of energy transfer versus the direction of wave propagation. This causes the deviation of the beam from the wave normal and attenuation of the ultrasound. Demonstration of this phenomenon can be seen in Figure 14. Unlike in the isotropic case, refraction does not follow Snell's law, which causes problems when inspecting an anisotropic weld, since it is harder to predict at which point the ultrasonic beam is actually scanning. [35]

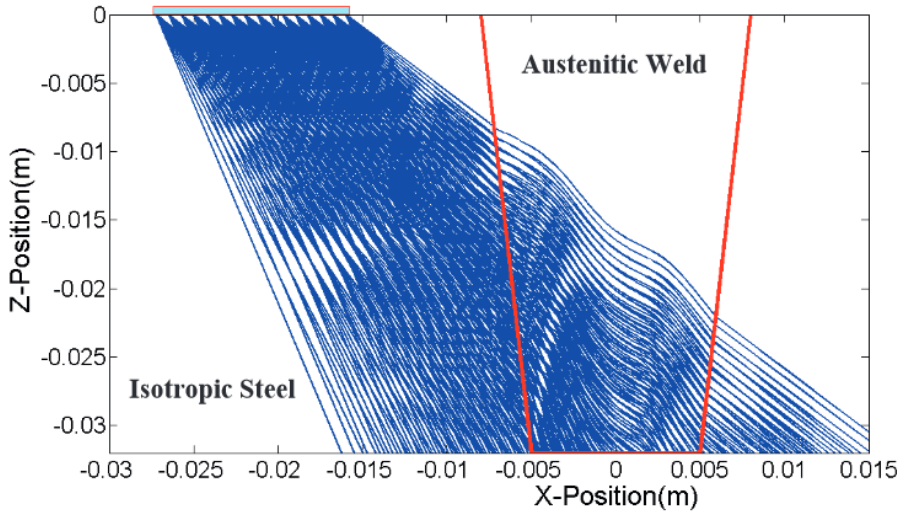

Figure 14 Ultrasonic ray pattern in inhomogeneous austenitic weld material [38]

3.1.4 Interference

There are two types of interference, constructive interference and destructive interference. In constructive interference two waves in the same phase are added together. This does not change the frequency of the wave but the amplitude is increased. In destructive interference the waves are out of phase by half of a period. This causes the waves to cancel each other out. For example, pulse repetition rate may be setup in a way that the successive sound waves interfere with each other destructively by reflecting from a flaw or back wall. This may lead to a dead zone and missing of the flaw. [29,39]

3.2 Generation of ultrasound

There are several ways to generate ultrasonic waves. Piezoelectricity, electrostriction, magnetostriction, electromagnetic acoustic transducer (EMAT) and laser are several of them. Piezoelectricity is the most common way of producing ultrasound thus it is covered more in detail in the following chapter. [40]

When stress is applied to piezoelectric component in addition to strain, also a difference of potential between opposing faces of the crystal is produced. This phenomenon is direct piezoelectric effect. This effect is used when ultrasonic waves reach the piezoelectric component causing stress to the surface. This stress produces potential difference, which can be detected with a flaw detector attached to the piezoelectric transducer. This phenomenon works also the other way around, meaning that potential difference to piezoelectric crystal induces a strain. Strain causes disturbance to the molecules near the surface of the piezoelectric crystal, which in turn starts an ultrasonic wave. This process can work with really high frequency, enabling ultrasound generation. [40]

The sound pulse generated from the piezoelectric crystal is approximately 1 µs long. The pulse has different frequencies, which can be rectified or smoothed. The shape of the sound beam depends on the wavelength of the sound and the diameter of the transducer. Effect of the diameter *Δ* can be seen in Figure 15. When the wavelength is considerably higher than the transducer diameter also diffraction increases. As the wavelength goes down diffraction has lesser effect. *L* demonstrates longitudinal wave, *T* transverse wave and *S* surface wave. [32]

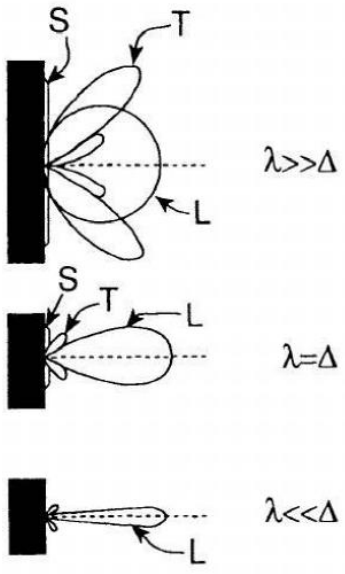

Figure 15 Effect of transducer diameter Δ to beam distortion [32]

Sound beam is divided into two zones, near field (Fresnel zone) and far field (Fraunhofer zone), which can be seen in Figure 16. This division is done since the beam intensity is not uniform. In addition to intensity fluctuations there is a dead zone right under the transducer. The reason and the length for this dead zone comes from the length of the pulse. When a transducer is emitting a pulse it cannot receive an echo pulse until the transmitted pulse has died down. Therefore also the damping property of the transducer crystal is important so that the crystal does not resonate for too long thus lengthening the size of the dead zone. [32]

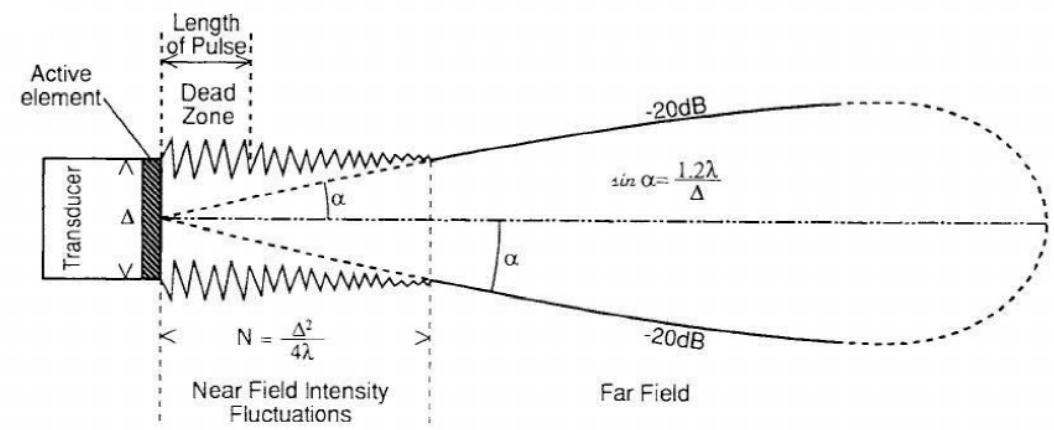

Figure 16 Near field and far field of the sound beam [32]

As seen in Figure 16, near field length N can be calculated using the relation between the transducer diameter and the wavelength.

Since piezoelectricity is related to stress and strain, Cartz relates these piezoelectric constants α and β to Young's Modulus with equation:

$$E = \frac{1}{\alpha\beta}. \tag{5}$$

For a good transmitter, β should be large and for receiver α should be large. However, relation to E prevents both of them to be large. This is why dual crystal transducers are used when good transmission and receiving is desired. [32]

3.3 Weld inspection with ultrasound

Ultrasonic testing is used to examine the structural integrity of a weld and the surrounding base material. The main purpose for ultrasonic testing is discontinuity detection; it can also be used to determine the thickness of a material, study elastic moduli or metallurgical structure and process variable evaluation on a component. Ultrasonic testing has a high sensitivity to detect flaws and determine their size, good penetration power even in very thick components, quick to deploy as well as use and a need to access to only one surface of the component. However, there are some disadvantages such as too rough surface, unfavorable geometry and internal structure which cause distortion or attenuation of ultrasound. Ultrasound is not favorable detecting volumetric flaws, but excels in planar cases, when compared to radiography, which is another volumetric structural integrity evaluation method. [41,42]

3.3.1 Conventional ultrasonic inspection

The most common way to inspect welds with ultrasonic testing is the pulse-echo method with angled beam. Pulse-echo method was first used in World War I to locate objects

under water such as submarines. The idea is to send an ultrasonic pulse from the transducer into the material. The sound pulse propagates in the solid until it faces the back wall or a discontinuity, in which case it reflects back to the transducer. The time period between the transmitted pulse and received echo is measured. When the sound velocity for the material is known, the distance can be measured. This distance measured can be either the thickness of the material or the location of a discontinuity. In c section of Figure 17, a situation where a flaw is as large or larger as the sound beam diameter so the sound cannot propagate any further is demonstrated. In sections d and e the sound is completely or partially refracted from the flaw or the back wall so it does not reach back to the transducer. In section f the effect of attenuation where the structure of the material causes only noise also known as “grass” shown on the screen is demonstrated. [43]

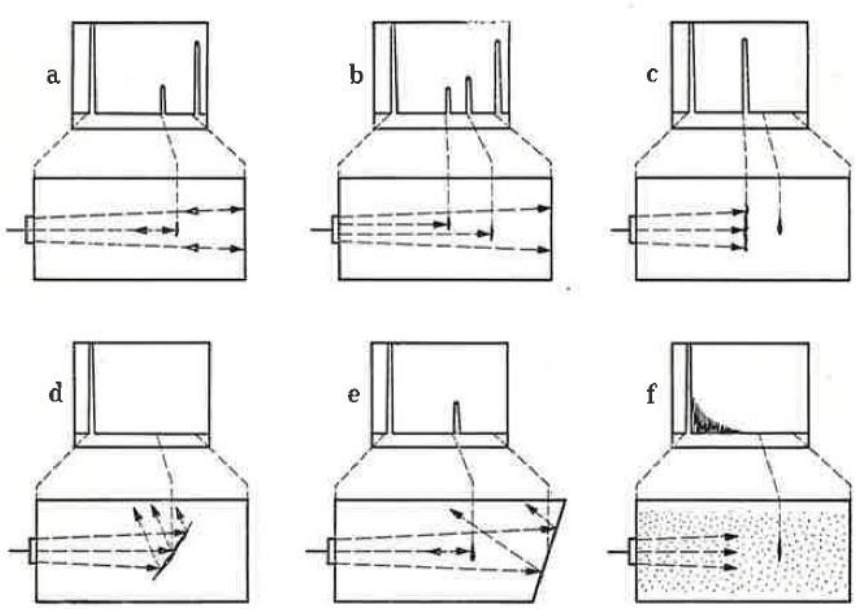

Figure 17 Screen pictures obtained by the pulse echo method [43]

The angle of the wedge is usually chosen according to the first critical angle so that the longitudinal wave does not penetrate into the specimen but only the shear wave does. Shear wave can be generated also directly using EMAT. Shear wave can be used to inspect the weld directly (half skip) or it can be reflected from the back wall of the specimen (full skip) as seen in Figure 18. In order to reach the area near the weld root beam angels over 45 degrees are used. This is due to weld crown which usually prevents moving the transducer on top of it close enough. In some cases weld crown can be grind off, so that inspection directly on top of the weld is possible. [44–46]

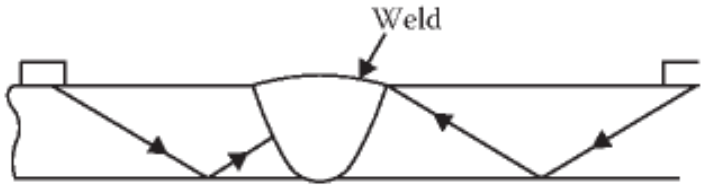

Figure 18 Reflection from back wall [45]

Since different wave modes have different propagation velocities it is necessary to take account these aspects when designing the inspection procedure. Otherwise these unaccounted wave modes may cause confusion or even mislead to false flaw indications when these waves are reflecting from the walls. [45,46]

There are also normal probes, which are not that common when inspecting welds. The sound beam is normal to the surface hence the name, normal probe. The problem with the normal probes in weld inspection is the angle the sound beam converges with the flaw. Cracks and lack of fusion in welding are more or less perpendicularly aligned to the inspection plane, thus the reflecting area for the normal sound beam is smaller than the cases with angled probes. Normal probe is used to scan near the weld in case of laminations in the base metal, which could interfere with angled beam.[43,47]

3.3.2 Phased array ultrasonic technique

In the conventional ultrasonic testing, only a single element or dual element (transmitter receiver) transducers are used. One element generates ultrasonic beam with one angle so multiple probes with different angles are needed to detect the flaws with different orientations. In order to scan wider areas, the transducer must be moved for example by hand or by a robot carefully along to surface area to cover the whole weld volume. In the ultrasonic phased array testing there is an array of multiple elements which can be used separately to transmit and receive ultrasonic signal. When an element in an array is driven, it generates a spherical wave and combination of these waves from other elements form a traveling wave pulse, according to Huygens' principle discussed in chapter 3.1.2 Reflection of sound waves. The angle and focus of the traveling wave pulse can be controlled by delaying the single element wave pulse as seen in Figure 19. These delays are also called focal laws. The advantage compared to a conventional ultrasonic transducer is the possibility to utilize multiple angles and focusing depths with a single probe. In addition, there is a possibility to scan a group of elements electronically thus covering a larger area with a single scan. Since the scanning is done with multiple elements the amount of received data is substantially larger than with conventional A-scan. Often this received data from inspection is stored digitally, allowing later review and processing of data. [28]

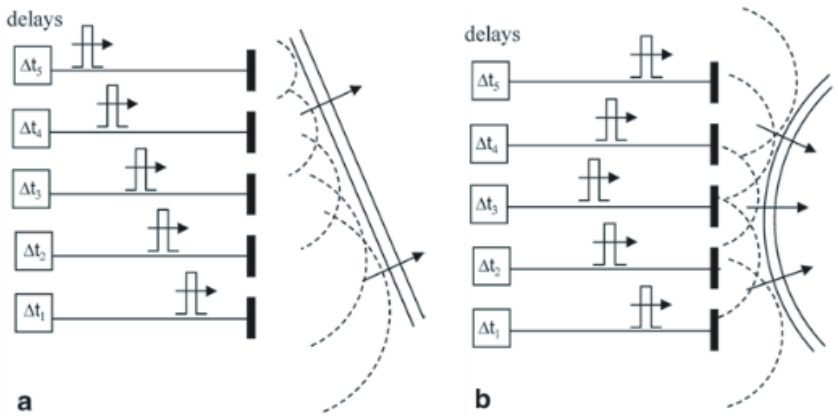

Figure 19 Element delays used to steer (a) and to focus (b) the sound beam [28]

The arrays can be either linear arrays or 2D matrix arrays. The main difference between these two is that the 2D gives more options to steer the sound beam path. Linear array can change the steering angle or focus the beam cylindrically while 2D array can change the steering, tilt, and skew angles as well as focus of the beam. [28]

Special case of phased array is the sampling phased array. This new technique reduces the dead zone and enhances the inspection of anisotropic materials such as stainless steel. In this method one element is transmitting sound pulse at a time and all the other elements act as receiver elements. [48]

3.3.3 Time-of-Flight Diffraction Technique

The Time-of-Flight Diffraction (TOFD) uses a set of two angle probes arranged in a V-shaped transmission. One probe is a transmitter and the other is a receiver. Since these two transducers are separated from each other they don't need sound dampening like normal transducers, hence TOFD transducers are cheaper to manufacture. When measuring the size of a flaw or a discontinuity, TOFD uses the time-of-flight of the diffracted signals from the tips of discontinuities instead of the signal amplitude. When the velocity of the sound in the material is known, distance between these two points can be calculated. The TOFD setup and signal are demonstrated in Figure 20. As seen on the figure, wave on the surface travels first to the receiver, which causes the first spike to be plotted. Second amplitude spikes are from diffractions from the flaw tips and the latter is the bottom echo. The plotting is done with high frequency RF-signal, which is not generally used in conventional ultrasonic testing. Also in contrast to conventional angle inspection, TOFD uses longitudinal waves instead of shear waves. Longitudinal waves propagate faster than shear waves thus they have shorter time of flight, reducing the interfering signals. [49,39]

Scanning can be done manually by hand or automated with a robot. The scanning rig needs to be designed in a way so that the probes maintain a constant distance and alignment to each other during the scanning procedure. In order to generate a position

related B-scan, information on probe location can be provided by using encoders to track probe movement along the inspection surface. [39]

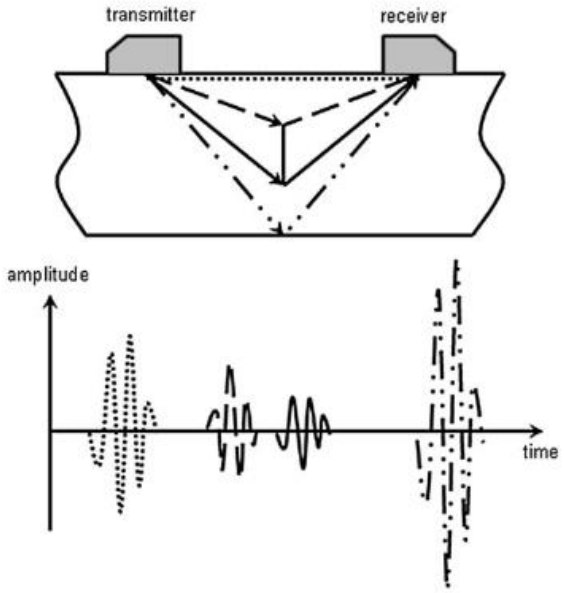

Figure 20 TOFD techinque [49]

By changing center frequency, transducer size and nominal probe angle TOFD is able to inspect thicknesses up to 70 mm effectively. When thickness is greater than 70 mm, wall thickness needs to be divided into more than one inspection zones to cover the variety of different depth regions. Orientation of the flaw has a little effect on the detectability since compared to pulse echo method the amplitude drops significantly less when tilt and skew angle of the flaw increase. TOFD saves and digitalizes the inspection data for later use, which can also be considered as an advantage. [39,50,51]

3.3.4 Flaw evaluation

Not every flaw found in a weld leads to an automatic rejection of the weld. There are procedures and standards which determine which size of a flaw is within the acceptance limits. To measure the size of a flaw the ultrasonic device needs to be calibrated in order for the results to be consistent. The used probe has an effect on the flaw detection as well. The probe frequency determines the wavelength of ultrasound and general rule in ultrasonic inspection is that the flaw size should be at least one half the wavelength in order to be easily detected. Cracks are usually propagating into the material so in order to measure the height of the flaw an angular wedge needs to be used. This allows ultrasonic beam to scan the flaw from its side and allowing larger reflecting area than with normal probe. [46,52,53]

The flaw acceptance limits depend on the application of the specimen and in the most cases the combination of the size of the flaw and the echo amplitude. In the highest

quality standards high enough echo amplitude alone can lead to the rejection of the weld. The shape of discontinuities can be most simply classified as point, elongated or complex. Point has no significant extent in any direction whereas elongated extends in one direction. Complex discontinuity can be divided into two sub-classifications, the planar -classification, where it has extent in two directions and the volumetric classification where it extends in the third direction as well. [46]

When evaluating the structural integrity of a material, accurate sizing of the flaw becomes important. To comprehend the whole situation both the height and the length of the discontinuity can be measured by using maximum echo height techniques, probe movement sizing techniques, tip diffraction techniques or synthetic aperture focusing technique (SAFT). These techniques can also be used alongside with each other to acquire the most accurate result for both the height and the length. [54]

Maximum echo height techniques are distance-gain-size (DGS) and distance-amplitude-correction (DAC). In DGS the maximum echo height is determined by using a reference reflector perpendicular to beam axis and the same sound path range as the discontinuity being measured. The acquired DGS curve is determined theoretically for certain probe type, transducer diameter and frequency. Accuracy can be improved by using smaller and smoother reference reflector. Like DGS, DAC is set up by using a standardized reference block. The idea is that the same reflector produces different amplitudes at different distances from the transducer. Echo amplitude can then be compared to the DAC curve to evaluate if the found flaw is bigger or smaller than the reference from the calibration block. DGS has an advantage over DAC when testing at long ranges, since DGS does not require calibration block the size of the testing distance. Since the accuracy of maximum echo height sizing is related to the discontinuity perpendicularity to the sound beam axis, length sizing is more accurate than height sizing with this method. [46,54]

For probe movement sizing techniques, 6 dB drop from maximum is fairly common method. Probe location is documented when the maximum echo amplitude from the discontinuity has dropped approximately 6 dBs, correlating to 50% of the maximum amplitude. This indicates that at this point the tip of discontinuity would be approximately in the middle of the sound beam. This method is relatively accurate, but if the discontinuity shows irregularities sizing errors may be significant. [54]

Tip diffraction techniques such as TOFD and single probe diffraction technique are considered special sizing techniques alongside synthetic aperture focusing technique (SAFT). In single probe diffraction, crack height can be measured by measuring the diffracted signal from a crack tip and a bottom corner of a crack. When bottom corner of a flaw is detected the probe is moved to find the crack tip, which causes the signal to peak and flaw height can be measured by trigonometric calculation. Tip diffraction techniques are fairly accurate. However, when using TOFD for size measurement, geometry, attenuation and sensitivity must be taken accounted for. In SAFT it is possible

to superimpose signals from the flaw thus improving signal/noise ratio. This on the other hand, increases the accuracy to measure the position of the flaw. [54,55]

As stated before, there is also interfering noise from microstructure grains and other sources which cause coming ultrasonic wave to scatter at the interface. This structural noise can lead to missing an existing flaw. Signal-to-noise ratio (SNR) is often used to measure the detectability of a flaw. Anderson et al. state in their report a reliable signal response should usually be twice the noise, hence the SNR should be at least 2 to 1 [56]. However, the report also states that standards ASTM E213-09 (2009), *Standard Practice for Ultrasonic Testing of Metal Pipe and Tubing* and ASTM E2192-13 (2013) *Standard Guide for Planar Flaw Height Sizing by Ultrasonics* considering dual-element probes determine SNR of 3 to 1 as a minimum requirement for flaw to be considered as detectable. On the other hand, according to the report, standard ASTM E273-10 (2010), *Ultrasonic Testing of the Weld Zone of Welded Pipe and Tubing* determines SNR as 2,5. Therefore, there is no clear statement which would be the absolute limit for "good" SNR. [56,57]

SNR calculation can be seen in equation 6.

$$SNR = \sqrt{\frac{16}{\rho v_{metal} w_x w_y \Delta t}} \frac{A_{flaw}(f_0)}{FOM(f_0)} \tag{6}$$

Where v_{metal} is the speed of sound in metal, $w_x w_y$ are lateral beam widths at the flaw depth, Δt the pulse duration, $A_{flaw}(f_0)$ the scattered amplitude of a flaw at center frequency (peak frequency) and $FOM(f_0)$ the noise of figure of merit at center frequency (noise peak amplitude). SNR increases when the flaw size increases, beam is more focused or the pulse shortens, usually by increasing frequency. SNR decreases in materials with high density and/or high acoustic velocity. [57]

3.4 Ultrasonic testing of austenitic stainless steel

Austenitic welds are transversely isotropic. This means that the elastic properties are independent on direction on one plane as in Figure 21 the XY-plane. The elastic properties are dependent on the plane perpendicular to it. In austenitic welds the isotropic XY-plane is along the welding direction. Because of this inhomogeneous anisotropic columnar grain structure, it is difficult to detect flaws in or in the vicinity of the weld, since this structure affects the propagation of the ultrasound. For example, shear wave may be reflected from the fusion line. Also it can be reflected due to grain structure of austenite, causing a false flaw indication and excess attenuation. Longitudinal wave is more favorable in these situations even though it also suffers from attenuation. Mode conversions on the fusion line and columnar grains from longitudinal to shear waves cause problems in evaluating the weld. It is possible to use mode conversion as an advantage in inspection. When shear wave probe is set to first critical angle, longitudinal

wave is also produced into the material. This refracted longitudinal wave can be used to inspect the weld. This procedure requires experienced operator, since it is important to distinguish the shear wave and the lateral wave from each other. [46,58]

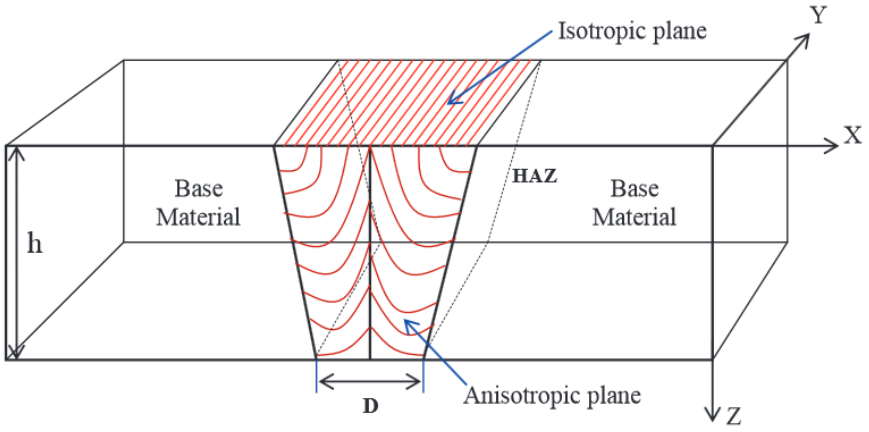

Figure 21 Transverse isotropic symmetry of austenitic weld [58]

Creeping wave is a special case of refracted longitudinal wave, used to detect surface and near-surface flaws. These waves can provide high sensitivity even with anisotropic welds. Flaws located near or on the surface of the back wall can be detected with secondary creeping wave, which is generated by shear waves from the primary creeping wave. This phenomenon is demonstrated in Figure 22. Since creeping waves are constantly generating shear waves, causing energy loss as they propagate, they cannot be used over large distances. [59]

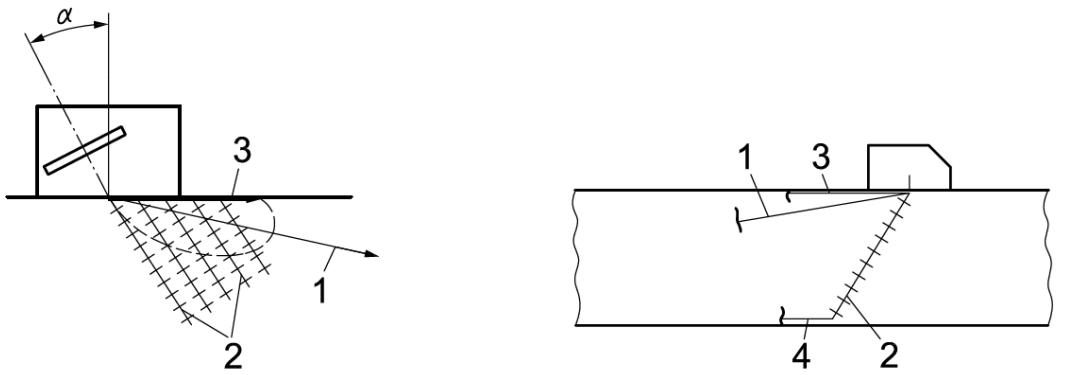

Figure 22 Generation of creeping waves and secondary creeping waves. 1 longitudinal wave, 2 shear wave, 3 primary creeping wave, 4 secondary creeping wave [59]

The procedure to inspect welds in austenitic stainless steel is the same as for any steel. Most commonly angled probes are used. To calibrate the range setting correctly with

angled probes, a calibration block must be used as for ferritic steel. However, for stainless steel welds also the calibration block needs to be austenitic for accurate measurement result. This is due to the fact that austenite has different crystal structure besides different sound propagation as well. [59]

When calibrating the sensitivity of a probe to austenitic steel welds a proper reference block must be used. Weld parameters have significant impact on the ultrasonic properties in the weld so the weld in the reference block should be as identical as possible in welding procedure to ensure right heat input, deposition rate and the number of weld runs made. Artificial reflectors can be side-drilled holes or flat-bottomed holes to represent reflectors inside the weld. Surface notches can be used to represent surface defects on the scanning and the opposite surface. When drilling holes, it should be noted that when adjacent holes are too close to each other, they may cause interfering signals due to beam spread. An example of a reference block for austenitic welds can be seen in Figure 23, the weld crown and root can be grinded off, if necessary. [59]

Same methods can be used to inspect austenitic welds as for ferritic welds. However, attenuation, skewing and scattering of ultrasound in austenitic stainless steel must be taken accounted for as well as the lower SNR. In worst cases, austenitic weld might be impossible to inspect properly with a conventional method. To compensate these factors, preferably dual element probes are used. In this set up there are two elements from which one is acting as a transmitter and the other as a receiver and the idea is to focus the sound beam to a certain depth. These elements need to be acoustically and electronically isolated from each other. In order to increase SNR even further, longitudinal wave is used instead of the conventional shear wave in angle inspections. This type of probe is called transmit-receive longitudinal (TRL) probe. For the shear wave the probe is simply called transmit-receive shear (TRS) probe. The frequency of a probe is normally around 2 MHz and when the depth exceeds 20 mm, a probe with frequency around 1 MHz is used. The TRL/TRS probe can be either conventional ultrasound or phased array application. The more sophisticated method is to use dual matrix array probes (DMA), which uses matrix phased array probes with one transmitting and another receiving. Lowering the frequency is also one of the methods to lessen the scattering from the crystal structure, thus lessening the noise. [59–61]

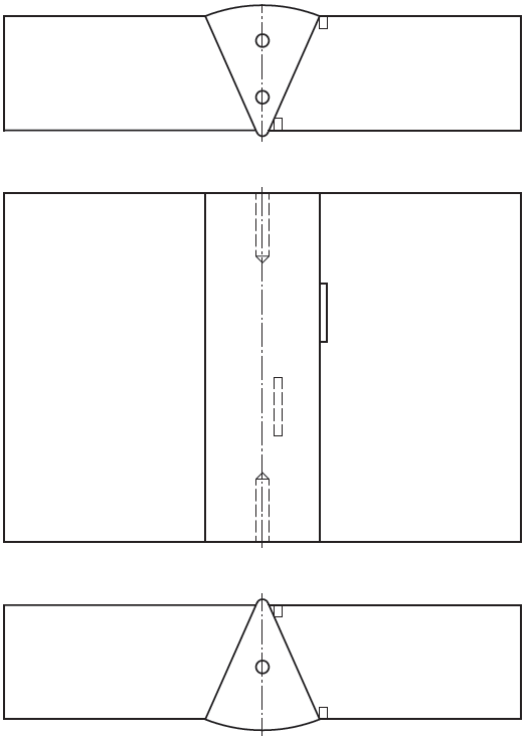

Figure 23 Reference block with machined holes and notches [59]

Kolkoori lists in his thesis properties which cause the difficulties to inspect austenitic welds. First of all elastic properties affects the energy flow. Dimensions and anisotropy of columnar grains affects when wave length corresponds to the grain size causing noise, which then hinders the flaw detection. Also inhomogeneous columnar grain structure curves the ultrasound path. Since the ultrasound path is curved and not linear, measuring the flaw position has been proven difficult. For shear crack the sound path deviation compared to isotropic case can be seen in Figure 24. [58]

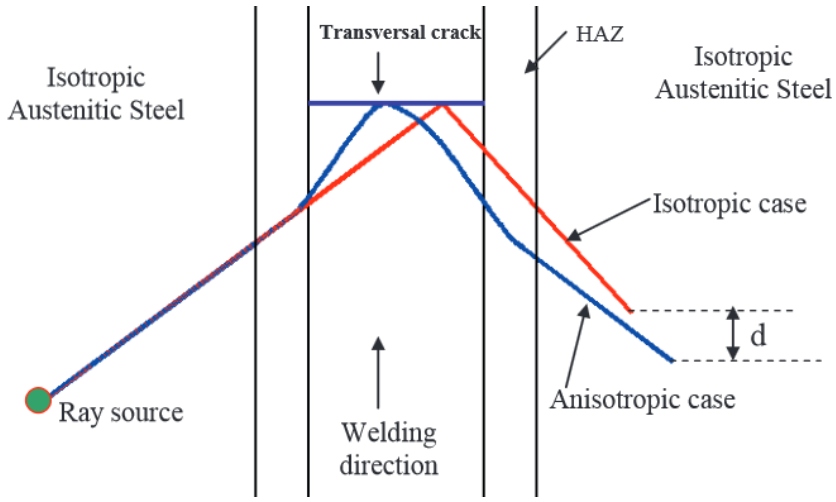

Figure 24 Ultrasound wave path in anisotropic weld [58]

4. SIMULATION

The use of simulation tools in ultrasonic non-destructive testing has been on the rise. There are also commercial software products to simulate ultrasound and its propagation. The most common are CIVA, which evaluates the ultrasonic beam using semi analytical solutions and a finite element simulation tool ATHENA with the combination of MINA model. [62,63]

The simulation tools are useful when determining parameters for ultrasonic probes and scan plans for the components. Simulation can also be used to aid analyzing the results. Probe evaluation is especially useful with phased array probes. For example CIVA can be used to calculate focal laws or to verify the setup to minimize unwanted lobe generation. Simulation also saves money and time in situations where a weld should be used to verify a certain probe or method. This is especially important when calculating probability of detection (POD) curves, which need a lot of reference points. POD will be discussed later on in chapter 5.5. Simulation methods can also be used to develop inspection procedures and for technical justification. Simulation calculations are based on elastic stiffness matrix of the solid which has been transformed from crystallographic coordinate system to calculated coordinate system. Computational simulation of ultrasonic testing is based on mathematical models, which are not discussed in depth in this thesis. [62–64]

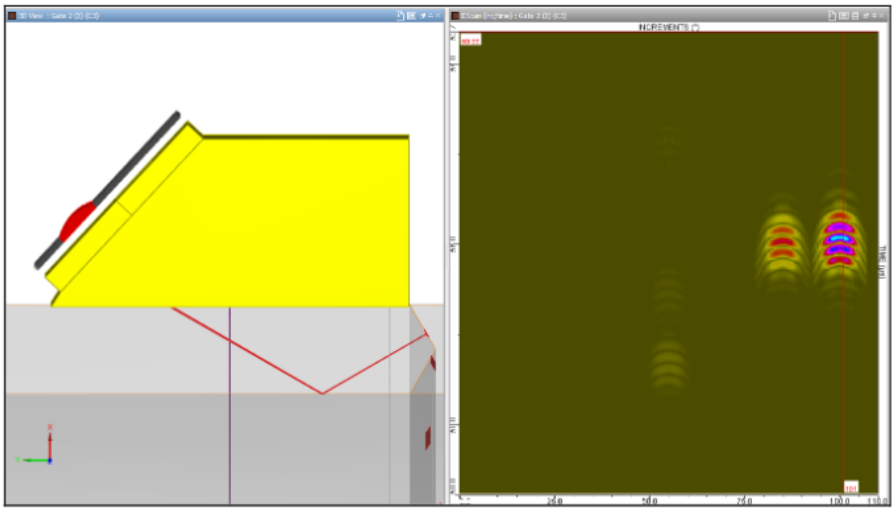

Figure 25 CIVA simulation tool [64]

Simulation can be used to determine ray path, ultrasonic field computation and computation of response from flaws. There are few different methods to carry out the calculations for the simulation, by numerical methods, approximated methods or analytical

methods. Numerical methods consist of Elastodynamic Finite Integration Technique (EFIT), Finite Element Model (FEM), Finite Difference Model (FDM) or Boundary Element Method (BEM). Gaussian Beam Superposition (GBS) is considered approximation method and ray tracing as an analytical method. [58,62]

Numerical methods require a lot of computing power and a high amount of memory. EFIT is used to model ultrasonic wave propagation thus it is time domain modeling tool. In FEM the geometry is discretized into a mesh of elements. The finer the mesh is the more accurate the result, however computational time increases as there are more elements to be calculated. In FDM the elastodynamic wave propagation is calculated by solving differential equations. Thus it is the most complicated numerical method and it is usually carried out by using a supercomputer, however the advantage of this model is its ability to calculate the scattering of ultrasound in the near field. FDM is usually used to study inhomogeneous anisotropic cases. BEM uses boundary integral equations, in which the elements are either line or surface types depending on the dimension of the problem. [58]

GBS as an approximated approach uses computation time less than the numerical approaches. It is based on Gaussian wave packets which are superposition of different wave vectors. It has been used to calculate focused beam fields of phased array ultrasonic transducers. [58]

Ray tracing is originally a numerical method in which complete wave propagation phenomena is taken into account. However, calculations are only carried out at the interfaces which effect the wave propagation. This saves computational time needed and makes it an analytical method. [63]

CIVA uses ray tracing in displaying the results. However, the computation is based on so called “pencil method”. In this method ultrasonic beam is described as a cone of rays from a single point source, as a tip of a pencil. These rays can be described as a four component pencil vector. The vector itself does not take the loss of amplitude into account, so it is applied later into the final divergence factor. This allows CIVA simulation to be used with complex structures and with arbitrary transducers, thus widening the possible uses for this software. [65]

To model flaws in a test specimen, CIVA uses different defect response models. These models are called Kirchoff, Geometrical Theory of Diffraction (GTD), Born and Separation of Variables (SOV). These different models are used to calculate different problems more efficiently, thus saving computational time. [66]

Kirchoff model is valid when the size of the flaw is greater than the wavelength. This model is used to calculate the response from specular reflections of crack-like flaws and volumetric cavities, such as semi-elliptical and multi-facetted flaws. When using two separate probes, such in tandem or TOFD inspection, the flaw orientation is important

for Kirchoff model to work. The transmitter and the receiver need to be in the same half-space determined by the orientation of the flaw. If the flaw is in too steep an angle and the probes are too far apart from each other, the model is not applicable. The example of this situation can be seen in Figure 26. CIVA version 11 upgraded the Kirchoff model to approximate flaws embedded in the anisotropic material, before the upgrade, the approximation was fairly strong and un-accurate. However, this problem still exists with the GTD and SOV models. [66]

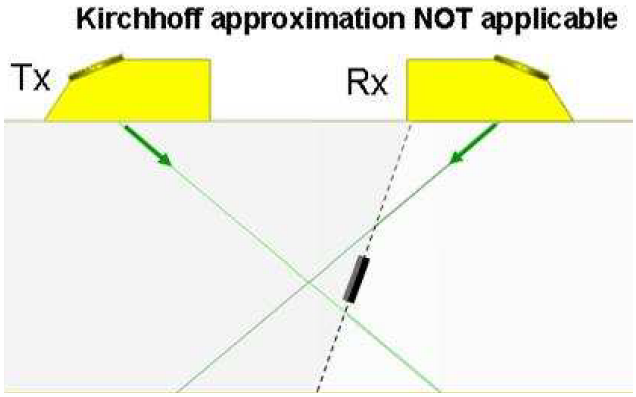

Figure 26 Example of the situation where Kirchoff model is not applicable [66]

GTD is based on the geometrical ray theory aiming at predicting the diffracted echoes from the flaws. Hence, GTD is designed especially TOFD and tandem inspection in mind. It is more accurate in prediction of diffraction from the flaw edges and inspection setups using shear waves. [66]

CIVA offers the possibility to combine Kirchoff and GTD modes to utilize the benefits of the two models. This gives the possibility to account the diffraction and specular reflections in the same simulation for planar and multi-facetted flaws. [66]

Born model simulates echoes scattered by a solid inclusion. It models the interactions between the ultrasonic beam and the flaw, which has similar material properties as the base material. This model is limited by the size of the flaw. The model does not allow calculations for flaws which have higher *ka* (wavenumber times the largest dimension of a flaw) ratio than 5. [66]

SOV model is specially designed to model scattering from a cylindrical cavity, such as side drilled holes or spherical solid inclusions. This model takes creeping waves formed from the cylindrical cavity into account unlike the Kirchoff model. However, the validity of this model has not been proved for 3D configuration or anisotropic material. [66]

Even though simulation has its advantages with speed, cost and versatility it should not be used only as a measure to validate a procedure. When used in combination with real specimens the model can fill the gaps in the experimental results, thus lessening the required amount of test specimens. Simulation can also be used to extrapolate the exper-

iment data in order to cover wider range of parameters. Beside from testing purposes using simulation is a valid method to train personnel and study the behavior of ultrasound in various cases. [67]

4.1 Simulation of austenitic stainless steel welds

As stated before, austenitic welds have anisotropic and a dendritic structure. Since the computer is a finite machine, it has difficulties to simulate irregular and random problems. However, these structures can be made with proper input data. [68]

The crystallographic texture of a weld can be characterized by using X-ray diffraction or electron back scattering diffraction (EBSD). This data can be used to model the weld accurately in the simulation. However, this is not a necessity to go through since the simulation software can approximate the weld fairly well. Especially MINA model, which was developed to describe the structural heterogeneity of a multipass shielded metal arc weld. This MINA model requires precise information on welding process in order to produce accurate results. Other way to roughly describe the anisotropic weld is to give the weld's elastic properties to an anisotropic matrix in CIVA. [68,69]

In order to describe this inhomogeneous structure, the weld is divided into finite number of anisotropic but homogeneous zones. These zones have their own elastic constants and orientation of columnar grains. The Figure 27 demonstrates the possible weld modelling of a K-chamfer weld and the black arrows in the figure stand for the orientation of the columnar grains. [68]

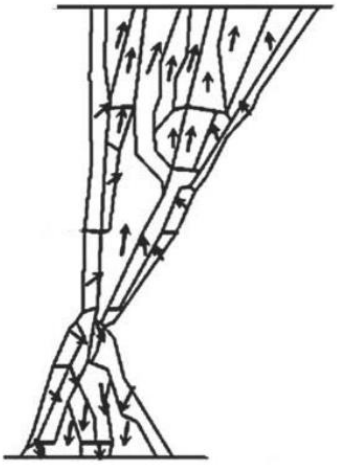

Figure 27 Austenitic weld described for ultrasonic modelling [68]

Ogilvy developed a formula to describe the grain structure of an austenitic weld mathematically. The equation can be seen below.

$$\tan\Theta = \begin{cases} \frac{-T(D+z\tan\alpha)}{x^{\eta}}, & x \geq 0 \\ \frac{T(D+z\tan\alpha)}{-x^{\eta}}, & x < 0 \end{cases} \quad (7)$$

The orientation Θ with respect to x-axis can be calculated where T is the slope of the columnar grain axis at the fusion faces, D is the half of the width of the gap between the weld root, α is the angle of weld preparation and η is a parameter set between 0 and 1 modeling the change of grain orientation as a function of the distance x from the weld center line. The resulting model can be seen in Figure 28. [65]

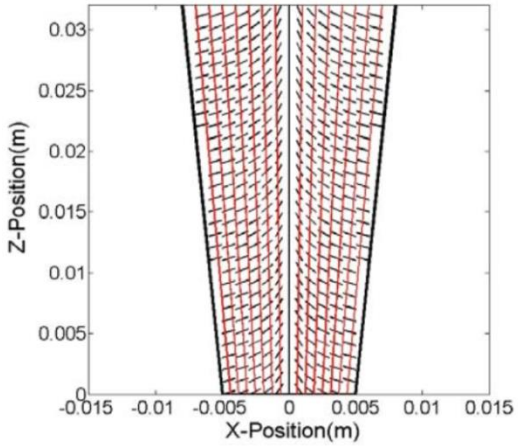

Figure 28 Approximated model of an inhomogeneous austenitic weld [65]

Structural noise is one of the main things, which cause problems when inspecting austenitic stainless steel welds. However, at this point simulation software is not fully capable to take this into account, despite the fact that CIVA can calculate attenuation and scattering. The problem is that coarse grain structure has too many initiation sites for scattering that the model cannot be used efficiently in austenitic stainless steel cases. [68,70]

The density and the crystal symmetry are the required parameters for CIVA to simulate anisotropic material. The crystal symmetry can be isotropic, cubic, transversely isotropic, orthotropic, monoclinic or triclinic. The symmetry determines how many different elasticity constant values must be entered. There is no separate model for anisotropic attenuation in CIVA, therefore the attenuation is treated the same for isotropic and anisotropic materials. [66]

Anisotropy of the austenitic weld also limits the possible use of defect response models in CIVA. Also simulating attenuation is a difficult and time consuming task, since there are a lot of factors contributing the overall loss of energy with austenitic stainless steels' grain structure one of the main factors. Attenuation due to grain scattering is not usually simulated on the grain scale, but it can be implemented as a model within the code in order to save computational time or treated as an isotropic attenuation. Despite all these limitations, modeling of an austenitic weld can be considered fairly reliable. [66]

5. DETECTION OF DIFFERENT KIND OF FLAWS

The main purpose for an NDT method is to find flaws e.g. for condition monitoring purposes. In order to evaluate the effectiveness of a certain method there needs to be enough knowledge of the searched flaw in order to evaluate and measure it properly. Since flaws are numerous in type, this thesis focuses mainly on cracks caused by in-service operation environment of an NPP. These types are: intergranular stress corrosion cracking, thermal and mechanical fatigue. [52]

To measure the size of cracks with ultrasound accurately has been proven difficult. Cracks have a variety of characteristics which include location, orientation, size, opening of a crack tip, residual stresses and fracture surface roughness among others. These have an effect on the propagation, reflection, diffraction, transmission, attenuation and diffusion of ultrasound which may hinder the detectability of a flaw. [71]

5.1 Influence of surface roughness, shape and size on flaw detection

In natural flaws the surface is never exactly planar caused by irregularities, which is why the production of artificial flaws which resemble real flaws is difficult. The crack surface roughness has a significant effect on the detectability of a crack. When the surface is rough, it decreases the scattered amplitude. As a smooth surface reflects a strong coherent field, a rough surface destroys the summation of the waves as the phase varies with the flaw surface. Effect of a crack surface roughness to an amplitude distribution can be seen in Figure 29. [71]

The surface roughness of a crack may influence positively to flaw detection in some situations. Due to a rough surface there are corners and smooth sections in numerous directions. In a case of misorientation, the angle is not that effective as for a smooth flaw surface. Unlike in a smooth flaw, where the pulse may be continuous the rough surface may cause scattering of the pulse. The rough surface of a flaw may also cause loss of diffracted pulses. Even though the flaw may be noticeable it is hard to determine its actual size. [71]

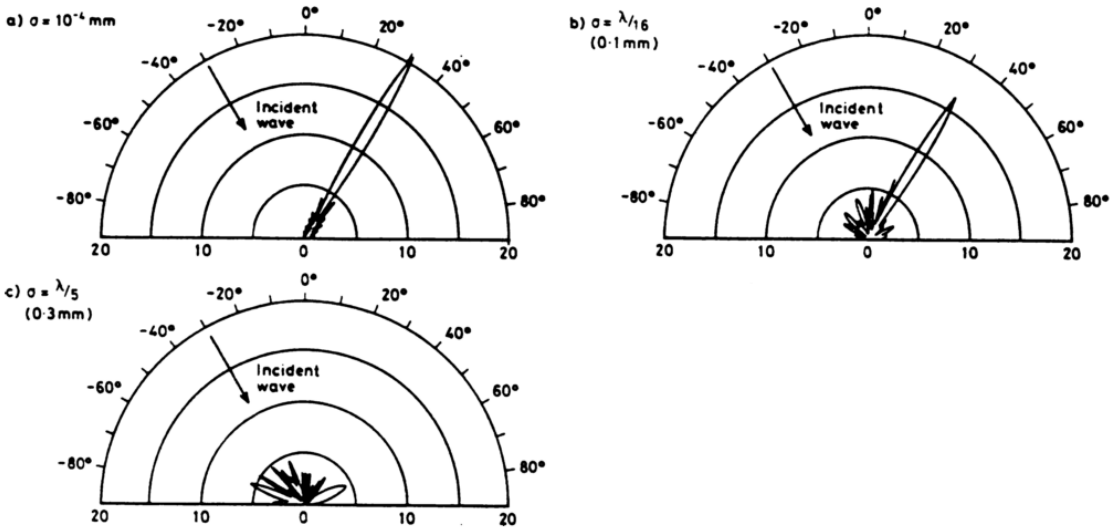

Figure 29 Polar plots of scattered amplitude distributions. 2MHz monochromatic wave is incident at 30°, σ represents different roughness values. [71]

Wåle divides cracks according to their macroscopic shape to five types: straight, winding, bend, bilinear and branched. Illustration of these types can be seen in Figure 30. As seen from the figure, manufacturing defects is not a straight forward process, especially if the result is needed to represent an actual flaw as much as possible. The more the branched shape, the harder it is to control the manufacturing process. [52]

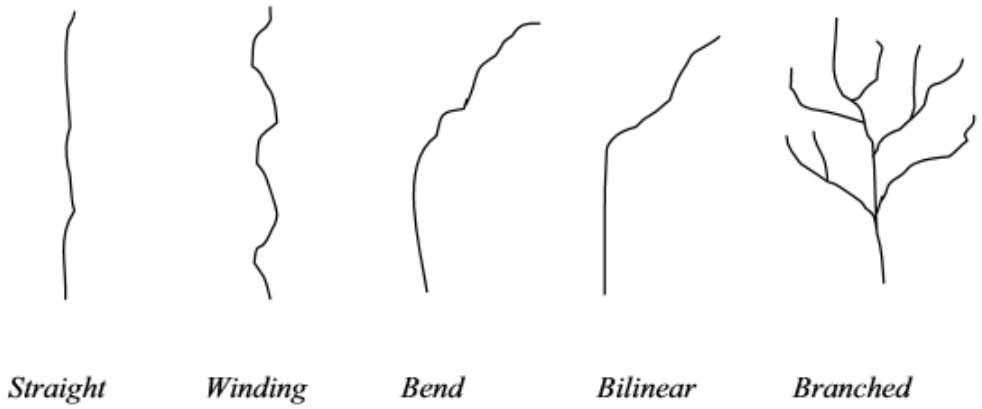

Figure 30 Different crack shapes [52]

5.2 Influence of crack opening and loading on flaw detection

Crack opening means the characteristic whether the crack is open from its tip to the opening corner of a crack or closed partially or through its whole length. If the crack is totally open the whole crack surface is free to oscillate the ultrasonic reflection, thus the echo amplitude is high. If the crack is partially or fully closed this oscillation is restricted lowering the surface area of reflection thus lowering the echo amplitude. So the crack exists, but in an ultrasonic inspection the structural integrity of a specimen may

not seem flawed. In situations where crack is partially open, sizing of the crack may prove difficult since signal amplitude varies along the crack. [71]

As stated above, studies have shown that increase in crack opening causes the rise of echo amplitude as well. Moreover, the crack depth increases the echo amplitude. This is reasonable indication since the surface area of the crack increases. To conclude, larger cracks with large opening are easier to detect. [71]

Loading conditions have an effect on the peak amplitude received from the reflection of the ultrasound from the crack. When crack is under compressive stress the amplitude is lowered. On the other hand, under tension the echo amplitude rises, this phenomenon can be seen in Figure 31. This is due to the fact that under compression the flaw faces come closer to each other. On tensile case, these faces are pulled apart thus widening and opening the existing flaw. In a case where crack is already tight and has a rough surface, change in the loading conditions has a more significant effect. Due to high points of crack surface already touching each other makes it a closed or partially closed crack. Of course when the crack is fully opened, reflected echo cannot gain more amplitude. [71]

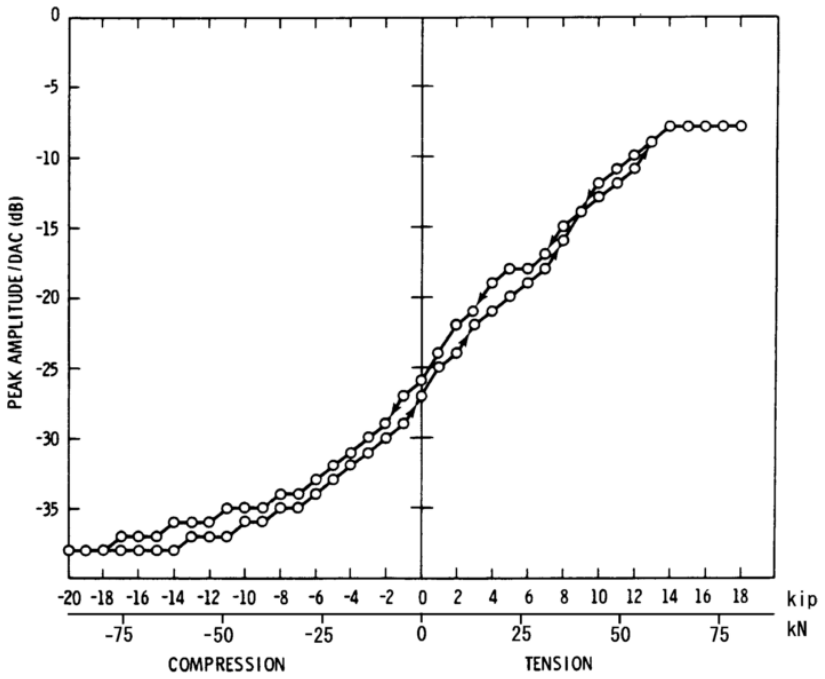

Figure 31 Different loading conditions affecting the obtained echo amplitude [71]

In in-service inspection (ISI) there are residual stresses present. These have to be considered since compressive stresses close the flaw and make it hard or impossible to detect. Cracks formed due to fatigue (mechanical or thermal) are the most susceptible on the effect of compressive stresses. Especially crack tips of thermal fatigue cracks are considered the most challenging since the crack tip is surrounded by a plastic zone

which is under compression. On the other hand tensile stresses open the flaw and might even lead to false rejection of the inspected component. [71]

5.3 Positional and orientation influence on flaw detection

Since the austenitic weld causes attenuation and scattering of ultrasonic beams the position of the flaw is also important. If the inspection is done through the weld the attenuation and scattering may cause the flaw to be missed. This is why it is strongly advised to inspect the weld from both sides to ensure the structural integrity of the specimen. Unfortunately, this is not always possible due to limited access caused by nearby components such as supports or difficult geometry [72]. In the cases where the flaw resides in the middle of the weld or the specimen is very thick, the detection of a flaw may prove difficult or even impossible. This is why various techniques, such as a set of different dual-element angle beam probes, longitudinal waves and creeping waves, should be considered. The idea is to focus the ultrasonic beam to a certain point of the weld to maximize the sensitivity. The amount of different probes can be reduced by using a phased array probe with different set of focus depths and wave angels. [35,59]

When the tilt of the flaw in relation to the sound beam increases the field is changed to an off-specular field. The effect of the crack surface roughness is also increased with the tilt angle. In order to get an ultrasonic response from a flaw, a large enough surface area for the reflection is needed. For example, if the ultrasound hits the crack tip, the reflection is very small regardless of the actual size of the flaw. An ultrasonic echo amplitudes related to the angle of incidence can be seen in Figure 32. Thus higher echo amplitudes are achieved in combination with higher tilt angles and when the opening corner is in more favorable position. [71]

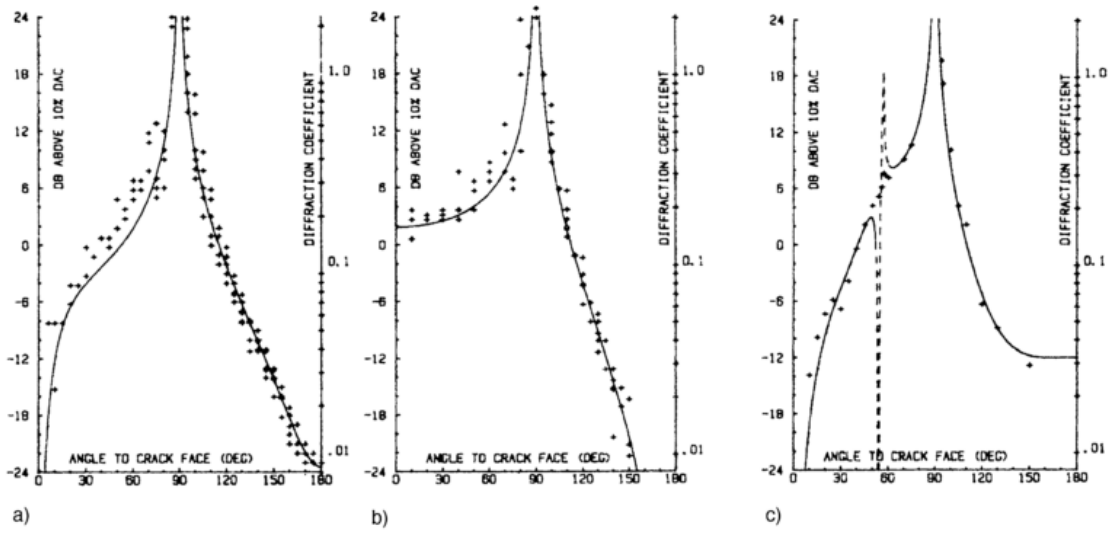

Figure 32 Pulse-echo response and the angle of incidence a) 5Mhz longitudinal b) Horizontally polarized 2,25MHz transverse and c) 2,25 transverse waves [71]

When a rough flaw is tilted to a certain point it may lead to self-shadowing phenomena. In this case a section of the surface is not directly covered by the incoming wave but the roughness of other parts from the surface shades the area. This effect diminishes the overall amplitude of the scattered field. [71]

5.4 Artificial flaws in evaluation of ultrasonic inspection

It is important to know the parameters of an artificial flaw precisely, due to application in which it is used. Artificial flaws can be used to validate certain inspection methods, for example ISIs for NPPs or to train inspectors to detect and evaluate flaws. Therefore it is necessary to manufacture artificial flaws to resemble real service-induced flaws as much as possible, so the ultrasonic indication would be similar to a real service-induced flaw. Since flaws are usually undesirable in welding it is not straightforward to produce these defects in a way that they have correct and required parameters. Using real flaws would be the ideal situation, but especially in NPP cases these parts are usually contaminated radioactively so the cleaning of these parts from radioactive substances is expensive and sometimes impossible. [73–75]

Ultrasonic testing can be used to find following flaws: Cracks, lack of fusion, lack of penetration, cavities, inclusions, pores, excess penetration, undercut, concavity, burn-trough, mismatch and lamination. Therefore artificial flaws are required to resemble these types of defects in order to validate a procedure. In this thesis the focus is on crack types which are found in ISI, excluding stress corrosion cracking. These types of cracks are artificially produced by mechanical or thermal fatigue and electric discharge machining (EDM). Although these cracks can be identified with surface inspection methods such as liquid penetrant testing, cracks usually form in places where only one surface is accessible. Such an example is the ISI of pipe welds in NPPs where a crack usually forms on the inside surface of the pipe. [73,74]

Cracks form as linear ruptures when a material is under stress. In most cases they are narrow separations, located in the weld or in the HAZ area. The types and locations of cracks vary a lot according to the welding parameters. Figure 33 shows different crack types and areas where cracks can appear in the weld. In an NPP environment, cracks can form in numerous places. These include straight pipe sections, valve bodies, pipe elbows and weld joint as well as base material. Crack growth direction is highly dependent on the component and the location, as well as the loading conditions and the local shape effect. In pipes the direction is usually either circumferential or axial. In HAZ crack growth direction is usually parallel to the weld and in the weld the direction is usually transverse. [74,75]

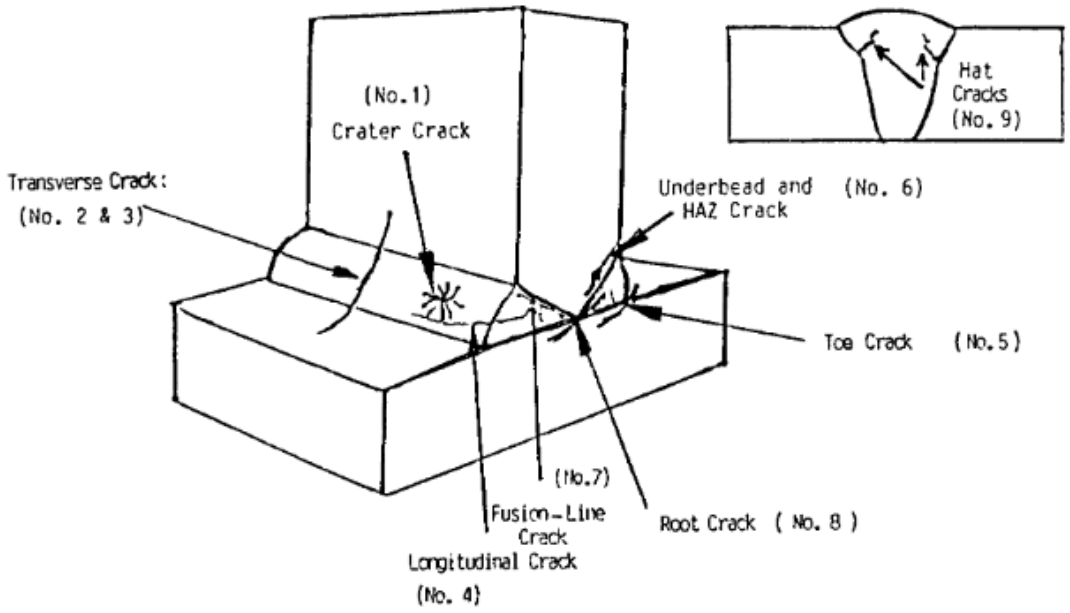

Figure 33 Crack types and possible locations [74]

5.4.1 Mechanical fatigue flaw

Cracks caused by mechanical fatigue are usually straight, with little or no branching. The surface roughness is the smoothest of the crack types, the correlation length is the highest. Cyclic loading of a specimen causes mechanical fatigue, for example vibration of steam pipes in NPPs. Residual stresses within the material, which are caused for example forming at a room temperature, makes the surface even more susceptible to cracking in combination with external cyclic tensile load. Welding causes often residual stresses, which leads to mechanical fatigue to occur near the weld fusion lines. These stresses are often parallel to the weld. In addition, geometrical stresses are higher than normal near the fusion lines. The crack parameters and comparison to other cracks can be seen in Table 4. Data for service-induced cracks are from Wåle, who collected the data from failure analysis pictures. Especially for the part for crack tip radius for mechanical fatigue is expected to be small; however statistic may have suffered from corrosion, hence the larger value. [52,76]

Mechanical fatigue cracks are produced in the same principle as the service-induced cracks by cyclic mechanical loading. The produced crack can be controlled with the number of cycles and it resembles the service-induced crack well. However, when these flaws need to be implemented to a large mock-up, doing these mechanical cycles may prove difficult. [76]

5.4.2 Thermal fatigue flaw

Thermal fatigue cracks are caused by sequential temperature changes and it is one of fatigue mechanisms in NPPs. The most typical component susceptible to thermal fatigue cracks are components in which cold and hot water mix together. Typically these are T-joints in a steam line. Turbulent mixing of the hot and cold fluid causes rapid temperature changes to the inner pipe wall. These rapid changes cause thermal expansion and contraction, leading to thermal stresses. Unlike mechanical fatigue, thermal fatigue is seldom seen near welds. In principle the mechanism for crack initiation and growth is the same as in a mechanical fatigue case, the crack is exposed to cyclic stresses. When the stresses exceed the yield strength of the material, thermally induced residual stresses are formed. [52,77]

Artificial thermal fatigue flaws are produced in the same manner as the real thermal fatigue cracks are formed. Material is exposed to rapid heating and cooling cycle, by high frequency induction heating and water or air cooling. This method causes thermal stresses to form and initiates crack growth, however thousands of heating and cooling cycles are needed in order to produce a crack. Figure 34 compares a real service-induced crack to an artificially produced thermal fatigue crack with 6500 cycles. As seen from the figure, the artificial crack is similar to the service-induced crack; both show minor branching, propagation transgranularly, small crack tip radius and narrow cracks. Largest deviation is from the larger opening of service-induced crack near the surface. Comparison of the parameters can be seen in Table 4, which shows that artificially produced crack in Figure 34 is within the parameters to be used as a reference flaw. [77]

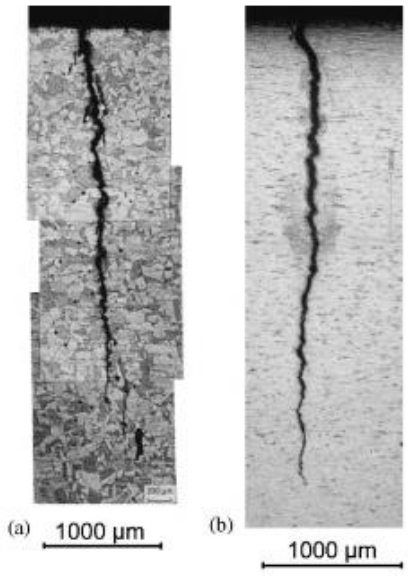

Figure 34 Comparison of (a) service-induced crack and (b)artificially produced thermal fatigue crack (6500 cycles) [77]

Table 4 Parameter comparison of service-induced thermal fatigue, mechanical fatigue and artificially produced thermal fatigue cracks.*Median value used from the data (Wåle). [52,77]

	Crack width, surface (µm)	Crack width, middle (µm)	Crack width, tip (µm)	Crack tip radius (µm)	Surface roughness R_Z (µm)
Artificial thermal fatigue	70	40	2		35-125
Service-induced thermal fatigue*	28,5	20	7	0,1	45
Service-induced mechanical fatigue*	28	20	7,5	3	13

5.4.3 EDM notch

Electric-discharge machined (EDM) notches are usually produced to a reference mock-up. Manufacturing process is nonconventional machining process, in which the material is removed very accurately in a controlled environment. Cutting is done with an electrode, which is shaped to resemble the desired flaw, only a bit shorter than the flaw desired. The electrode can either cut or burn the material in order to achieve the desired flaw shape and size. The parameters of a resulted flaw can be easily inspected with cast replica method to ensure that the desired flaw has been achieved. A typical cross-section of an EDM notch can be seen in Figure 35. [78]

Unlike thermal fatigue crack tip, EDM notch tip does not have any stresses, which affects the detection by ultrasound as stated above. When compared to thermal fatigue crack in Figure 34 it can be seen how different and multiform the shape of the crack is compared to EDM notch. Due to lack of versatility, EDM notches are normally used as robust artificial flaws, which are used when mechanical or thermal fatigue crack would be hard to produce on a certain place or the cost of producing other types of flaws is an issue. [77]

Figure 35 EDM notch [77]

According to a report from Koskinen and Leskelä was concluded that the height sizing of mechanical fatigue flaw reliably from the far side was not possible with ultrasonic methods. On the other hand EDM notch and thermal fatigue crack could be sized accurately enough from far side. They proposed that attenuation of ultrasound through the weld and properties of the mechanical fatigue crack diminished the tip diffraction signal below noticeable limit. This is uniform with the theory since the thermal fatigue crack and EDM notch had rougher surface and wider opening to the surface. In this case, the rougher surface of the thermal fatigue crack allowed amplitude from the reflection to be noticeable instead of giving interfering noise. [73]

5.5 Probability of Detection (POD)

The idea in probability of detection (POD) is to statistically represent the ability of a technique to detect a specific flaw size. For example for a flaw height of 3 mm probability of detection could be 90%, depending on the conditions. This is needed for comparative analysis of different NDT methods and flaw sizes, also to predict is it feasible to search a certain type of a flaw with certain a NDT method. A demonstration of a POD curve is seen in Figure 36. These curves are specified for a certain type of a flaw in a certain material. Also in order to establish a POD curve, numerous data points are required, hence numerous artificial flaws are required to achieve a large enough amount of data.[79]

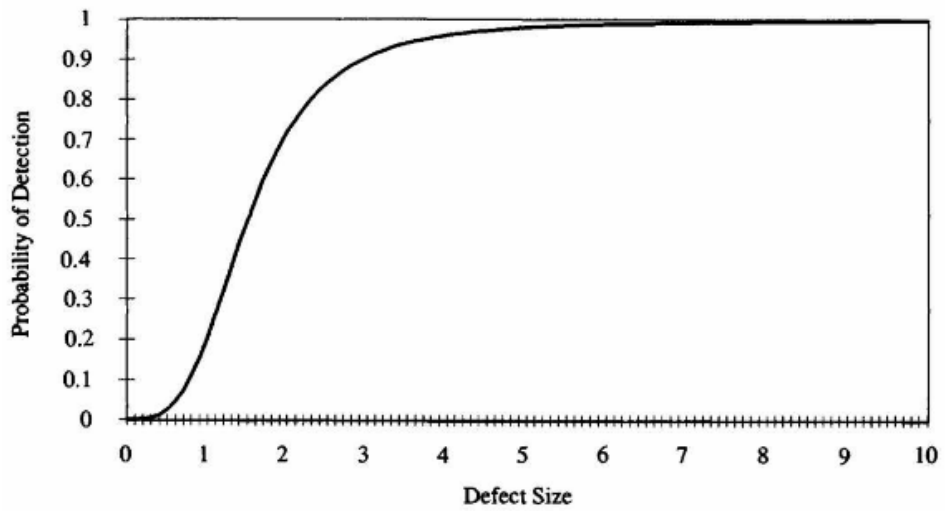

Figure 36 Example of a POD curve [79]

Detecting flaws with ultrasound or any other NDT method is not a straight forward process. Smallest detectable flaw does not mean it would be detected every time, due to numerous flaw parameters, attenuation and scattering discussed earlier affecting the detectability of the flaw. Flaws of the same size get missed and detected. This is the reason why statistics are used to describe how probable the detection of a certain size of a flaw will be. [80]

5.5.1 Calculating probability of detection

Originally NDT statistics were recorded whether the flaw was detected or not. Numerous artificial flaws were sent around to be tested for numerous NDT inspectors. The acquired data is called as a hit/miss data. POD curve can be calculated by using log-logistic distribution with the function below. [81]

$$POD(a) = \frac{e^{\frac{\pi}{\sqrt{3}}\left(\frac{\ln a - m}{\sigma}\right)}}{1 + e^{\frac{\pi}{\sqrt{3}}\left(\frac{\ln a - m}{\sigma}\right)}} \tag{8}$$

where a is the size of the flaw, m the median deviation and σ standard deviation. Variables to m and σ can also be written as:

$$m = -\frac{\alpha}{\beta} \tag{9}$$

And

$$\sigma = \frac{\pi}{\beta\sqrt{3}} \tag{10}$$

When they are adjusted to the previous equation, the result is as follows:

$$POD(a) = \frac{e^{(\alpha+\beta \ln a)}}{1+e^{(\alpha+\beta \ln a)}} \quad (11)$$

The equation is further explained in appendix A. Linearly this can be expressed as:

$$\ln\left(\frac{POD(a)}{1-POD(a)}\right) = \alpha + \beta \ln a \quad (12)$$

Where the term on the left hand side is the logarithm of the probability of success or failure of detection, hence the odds to find the flaw are related to the size of the flaw. Detailed calculation is shown in appendix A. The model is called log-odds model. [81]

$$\ln(odds) \propto \ln a \quad (13)$$

The hit/miss data gives an absolute value while the signal response from the ultrasonic testing is not absolute. The signal spike can be from structural noise or diminished due to the flaw geometry. Therefore using the signal response data to produce POD curves is recommended. In the signal response, a flaw is detected when $\hat{a}$ exceeds a pre-defined threshold $\hat{a}_{th}$. Demonstration of this threshold can be seen in Figure 37, a represents the linear dimension of a defect while $\hat{a}$ represents the response from an inspection stimulus. [81,82]

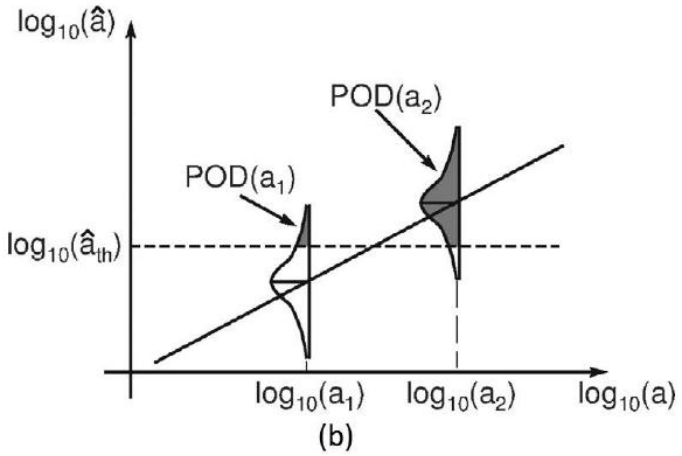

Figure 37 The decision threshold for a signal response data [82]

For the signal response approach POD function is derived from the correlation between $\hat{a}$ and a. There exists the following linear relationship between (ln (a)) and (ln ($\hat{a}$)):

$$\ln(\hat{a}) = \propto_1 + \beta_1 \ln(a) + \gamma \quad (14)$$

where γ represents an error distributed with a zero mean and standard deviation σ_γ. This means ln ($\hat{a}$) is normally distributed as N($\mu(a)$, σ_γ^2), that is with mean $\mu(a)=\alpha+\beta$ ln (a) and a constant standard deviation σ_γ. Since the signal response data is related to chance it can be expressed as below. [81,82]

$$POD(a) = Probability\ (\ln(\hat{a}) > \ln(\hat{a}_{th})) \quad (15)$$

This represents the shaded area in Figure 37. When F is a continuous cumulative distribution function and using the symmetric properties of a normal distribution, POD function for the signal response can be written as below. This function is further explained in appendix A. [81,82]

$$POD(a) = F\left[\frac{\ln(a)-\mu}{\sigma}\right] \tag{16}$$

To compute POD curves, sufficient amount of data points are needed. The data should also be relevant. Therefore it should represent the flaw sizes evenly. Figure 38 shows a typical distribution of found and missed flaws. As can be seen from the figure, there is a large group of flaws in between the smallest flaw detected $a_{smallest}$ and the largest flaw missed $a_{largest}$. [81]

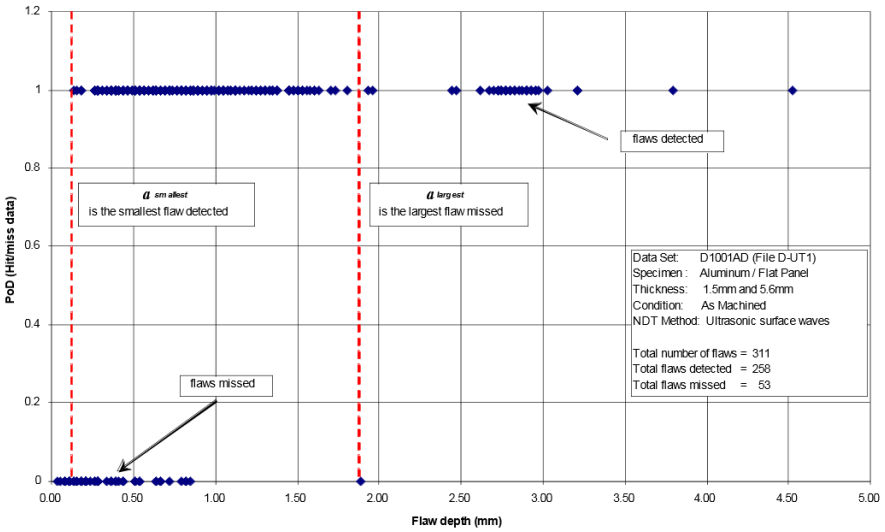

Figure 38 Hit/miss data, detected and missed flaws [81]

The flaw size distribution should focus on between these sizes, since otherwise the probability to find a very large flaw would be 100% and 0% for a very small flaw. For the hit/miss data best results are achieved with evenly distributed flaws between the smallest and the largest flaw detected. The minimum recommended amount of these flaws for this method is 60. Naturally more accurate results are achieved with increasing the amount of data points. [81]

Compared to the hit/miss data, signal response data is more forgiving in this matter. Due to higher amount of information this method provides, range of flaw sizes is not in such a large role as in the hit/miss situation. This lowers the need for a sample size to a minimum of 30 flaws. [81]

When a POD curve is derived, it can be estimated which size of flaws is feasible to search. When the crack growth rate is added to the equation, an economic inspection interval can be calculated. The ideal situation would be that flaw could be easily detect-

ed i.e. the size would be large enough for the most probable detection. However, this should be done at a point in time before the flaw size reaches the critical size, thus endangering the structural integrity. [82]

5.5.2 Confidence limit in probability of detection

The confidence limit in a POD means the approximation where the true POD curve might lie. For example a_{90} would mean the flaw size at probability of detection of 90%, $a_{90/95}$ means the flaw size with confidence level of 95%. This means that a flaw with a size of a will be detected with probability of 90% and if this experiment is repeated, 95% of the results will fall inside this confidence limit. [81,83]

POD with confidence limit can be used in combination when planning an inspection protocol. For example, if the maximum allowed flaw size a_{max} is known, then undetected flaws should be smaller than a_{max} in order to maintain structural integrity. This would mean that $a_{max} \leq a_{90/95}$. However, since POD is based on statistics, reasonable deviation of results is expected, hence the 95% confidence level is considered a reasonable level. [83]

5.5.3 Master probability of detection curves

Typically for flaw size a, the length or depth of the flaw is measured. Master probability of detection curves focus on the reflecting area of the flaw, thus $\hat{A}$ vs. A instead of $\hat{a}$ vs. a. Using the area relates to the fact that during the life of a fatigue crack it may have various shapes, but evolves to a semi-elliptical shape. This is advantageous especially when using ultrasound, since the reflecting echo indication is directly related to the reflecting area of the flaw. Considering the reflecting area, it is a fairly robust method. However, a fatigue crack can change its shape during the life of the component. Accordingly to Carboni and Cantini, studies have shown that a crack shape subjected to fatigue evolves towards a semi-elliptical shape. This enhances the viability of reflecting area to POD curves. Master POD curves are independent from the crack shape, thus they are characterized as general and versatile POD curves for evolving crack shapes so these curves can be used to estimate the flaw shapes with no experimental data. [82]

6. TESTING PROCEDURES

The agenda of the work was to scan the specimen which had same kind of an artificial flaw but within different locations around the weld. Experiments were conducted with phased array and conventional ultrasonic methods. Second phase was to compare these results with each other and also with the result from CIVA simulation.

6.1 Parameters for the test piece

The test piece was 200 mm wide and 299 mm long. Two plates were welded together so that the weld was placed in the middle of the specimen. The base material was rolled AISI 316L. The weld crown and the root were completely ground off and the whole surface of the test plate was ground evenly to a thickness of 22,1 mm. The weld itself was a 60° V-groove butt weld done with MAG welding. The width on top of the weld was measured with a ruler as 26 mm. The schematics of the specimen can be seen in Figure 39. The image of the bottom of the specimen and the EDM notches can be seen in Figure 40. The dashed line in the figure represents a surface flaw on top of the surface of the specimen. The unintended flaw is also marked as an *s* on the figure. This visible flaw could not be detected with ultrasound when the specimen was inspected for unintended flaws before the machining of the EDM notches, thus it is not presumed to affect the testing result either.

The idea was to scan the specimen from both sides of the weld, on top side of the plate and approximately from the same distance from the weld. In this thesis these sides are referred as a- and b-side, of which the a-side is the one closer to the origin. EDM notches were placed on the back side of the plate on four different locations near or in the weld. The flaw number 2 was placed in the vicinity of the weld in a way it would not be in direct contact with the weld metal. The fifth EDM notch was placed on the base material as a reference. The depths and the locations of the EDM notches were measured during the machining of the flaws approximately 5 mm, with exception of flaw number 1 with depth of 5,3 mm. The length of the flaws was 15 mm. The results were confirmed by measuring the flaw depths and locations again with a ruler.

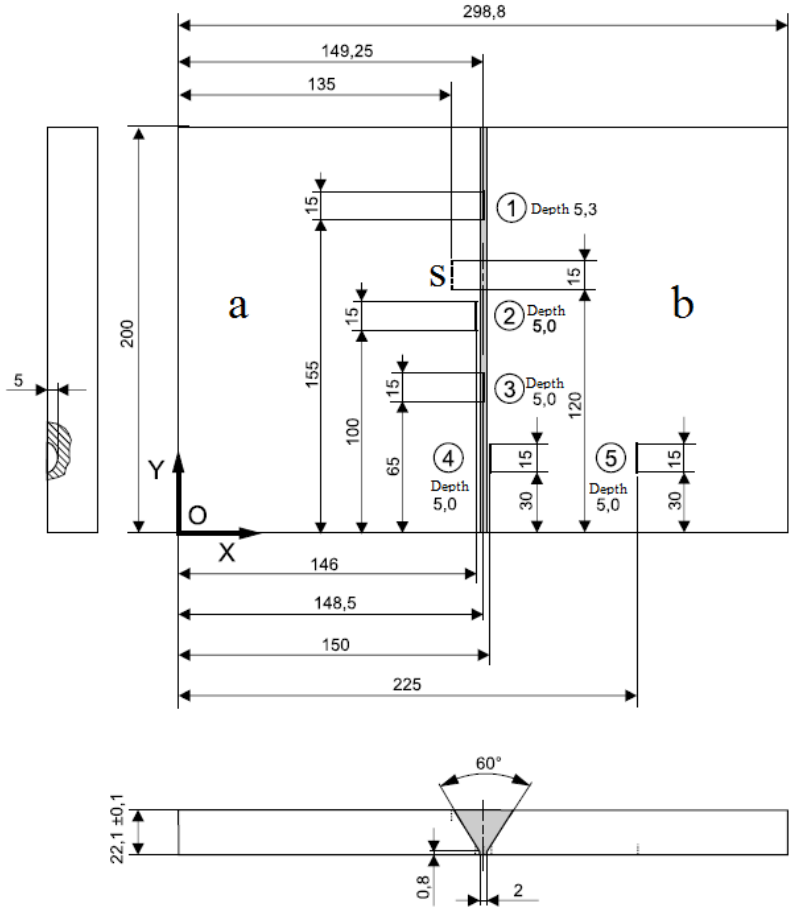

Figure 39 the test specimen described from the bottom. Letters a and b represent the side from the scan was made and s the position of the unintended surface flaw. Numbers 1-4 are the EDM notches inside the weld and number 5 in the base material.

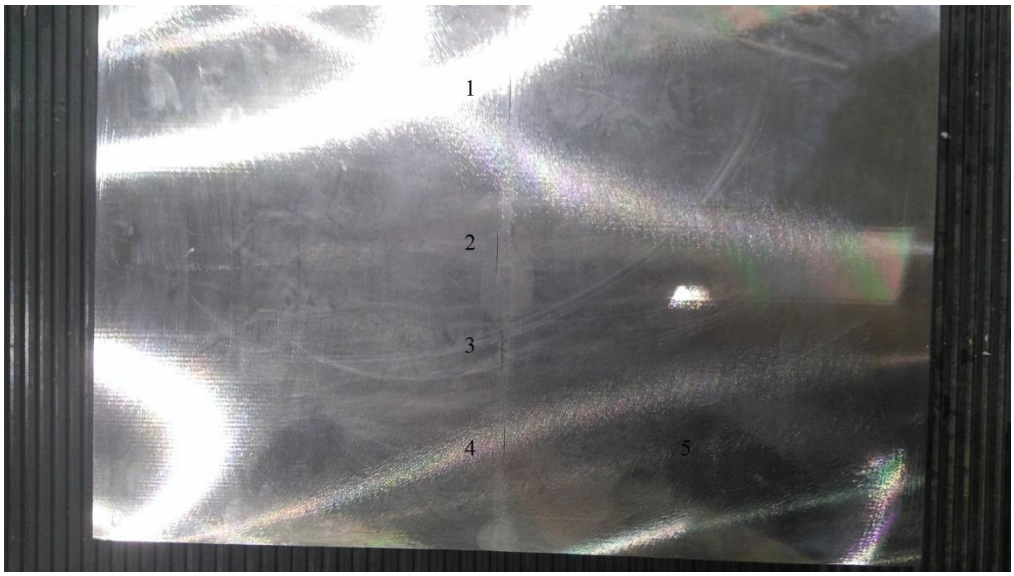

Figure 40 Test specimen and the EDM-notches from the bottom

For phased array ultrasonic inspection Zetec Omniscan MX 16/128PR flaw detector was used, which was linked to a laptop PC for data acquisition and evaluation. Manually used Zetec Manual Pipe Scanner was used to measure the probe position during scanning of the specimen. Since the scanner was operated manually, larger variations may have been caused by this factor. The scanning arrangement can be seen in Figure 41.

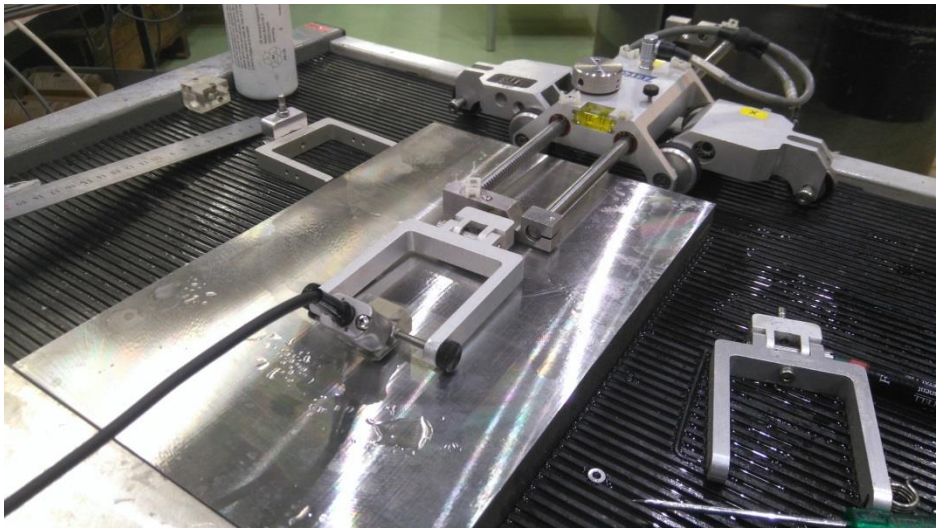

Figure 41 Scanner with a linear phased array probe attached and the specimen

6.2 Ultrasonic testing procedures

The summary of the used probes, their frequencies and wavelengths can be seen in Table 5. Longitudinal and transverse wave velocity was set to 5770 m/s and 3150 m/s [84] respectively.

Table 5 Summary of the probes, their frequencies and wavelengths

	2,25 MHz PA 40-75°	5 MHz PA 40-75°	2 MHz MWB 45° N2	2 MHz MWB 60° N2	1,5 MHz TRL 40-70°
f (MHz)	2,25	5	2	2	1,5
λ (mm)	1,37	0,61	1,54	1,54	3,83

For linear phased array inspection, a 16 element 5 MHz 5L16A10 and a 16 element 2,25 MHz 2.25L16A10 probes with SA10-N55 Rexolite wedge and shear wave were used. The focal laws were set according to an azimuthal scan between angles 40° and 75° with a step of 1° and to a true depth focus to 22 mm. Water was used as couplant and it

was applied to the surface of the specimen via spraying from a spray bottle with constant intervals. The calibration of the probes was done with calibration block for range setting according to SFS-EN ISO 22825 [59] (V2) before conducting the inspection with the probe.

For dual matrix phased array inspection, two 1,5 MHz probes with TRL Rexolite wedge and scan angles between 40° - 70° with step of 1° were used with focus to true depth of 22 mm. In addition, skew angles of -15° and 15° were applied. The calibration procedure and the couplant were the same as for linear phased array probes.

For comparison, two conventional 2 MHz MWB 45° N2 and MWB 60° N2 shear wave probes were used. The calibration was made also with the V2 block. These angles were chosen, since they are in the range of the angles of the phased array inspection and the ultrasonic beam from 60° probe would scan the weld groove perpendicularly with full skip inspection.

Maximum amplitudes were extracted from the acquired data in the positions of the flaws. The noise of the weld was measured between the flaws 1 and 2 for both a- and b-side. The noise was determined from the maximum amplitude between these two flaws, with an average of three measurements. The maximum amplitude was determined by inspecting the echo dynamics of the peak to assure it is not a random amplitude peak. When the noise for a specific technique had been determined SNR was calculated for each individual flaw and technique.

6.2.1 Scan plan

The inspection area for phased array probes and the TRL probe from the a-side was along the X-axis in between 109-139 mm and from the b-side in between 160-190 mm. Measurement was taken from the origin to the front side of the wedge. The scan covered the whole width of the weld, except for the flaw number 5 in which the width was 75 mm from the origin and the X-axis coordinates were for a-side 194-224 mm and for the b-side 226-256 mm. The probe was set perpendicular to the weld and scanned along the weld with 5 mm steps in the X-axis direction between the scan lines demonstrated in Figure 42. For each probe and each side the inspection was repeated three times. The starting position of a scan was calibrated for each separate scan with a ruler. The positional measurement for X-axis was determined from the front of the wedge and for Y-axis from the middle of the wedge. The starting point of the ultrasound was measured and taken account in the experiments.

The inspection area for the 60° probe was kept the same, only the perpendicular resolution was changed from 5 mm to 2 mm. However, for 45° probe the inspection area was changed to 125-145 mm and 155-175 mm for a-side and b-side respectively. These changes were made in order to achieve better coverage since the path of the ultrasound

is considerably steeper compared to the linear phased array, conventional 60° and TRL setup.

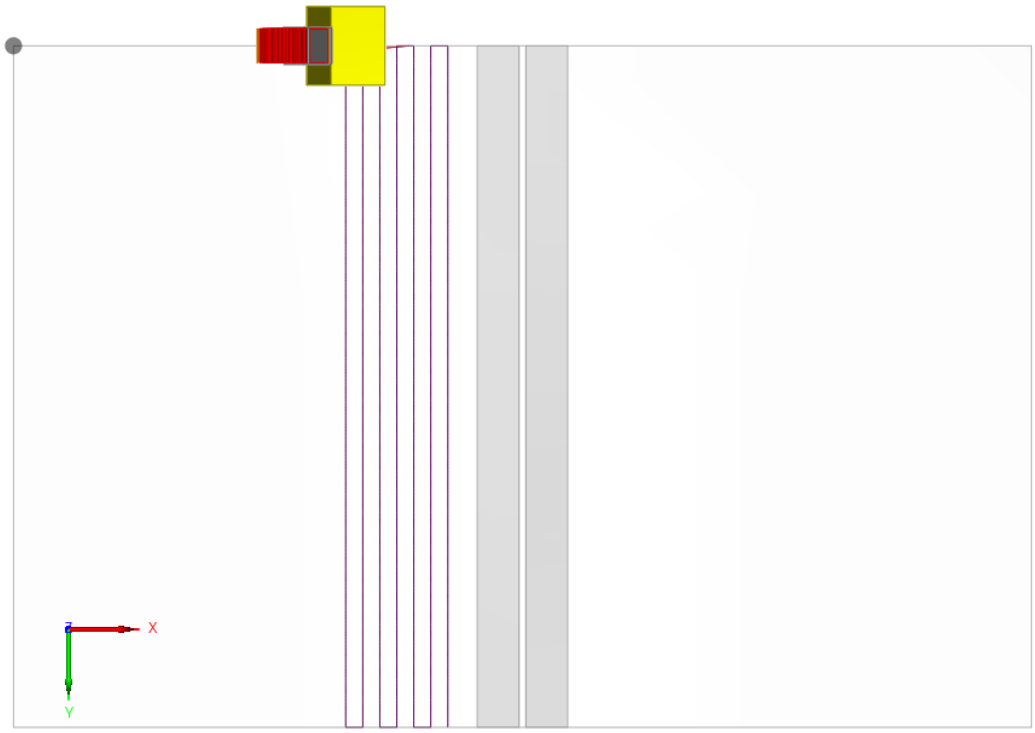

Figure 42 Visualized scan plan from the top side for a-side. Grey dot represents the origin and the purple line the probe movement along the surface

The gain was set for according to amplitude response from the flaw number 5. Aim was to set the maximum amplitude around 80%. For linear phased array probes, 8 dB was chosen for this test. For conventional and the TRL probes, the same procedure was used and the gain was set to 35 dB and for TRL probe 33 dB was chosen.

6.3 Simulation procedures

For simulation a simulation software CIVA version 11.1 was used. Simulation was made for 2,25 MHz linear phased array probe similar to the one in the conducted test. The specimen was modelled into the simulation software and the anisotropic matrix for the weld was set from an average of two 316L welds from the literature [85]. The inspection area was narrowed for y direction to the highest points of the elliptical flaws. The x-coordinates were the same as in the test specimen, with 5 mm steps. Structural noise and mode conversion were not taken into account in the computation of the model. For flaw response calculation Kirchoff & GTD model was used. The setup is demonstrated in Figure 43.

The flaw number 5 was only modeled from the one side, since the material was isotropic and the results would not be expected to change. The computation of the results

for each sample was only done once, since CIVA software does not calculate separate random seed for each ultrasonic testing so computation of the results would not have varied.

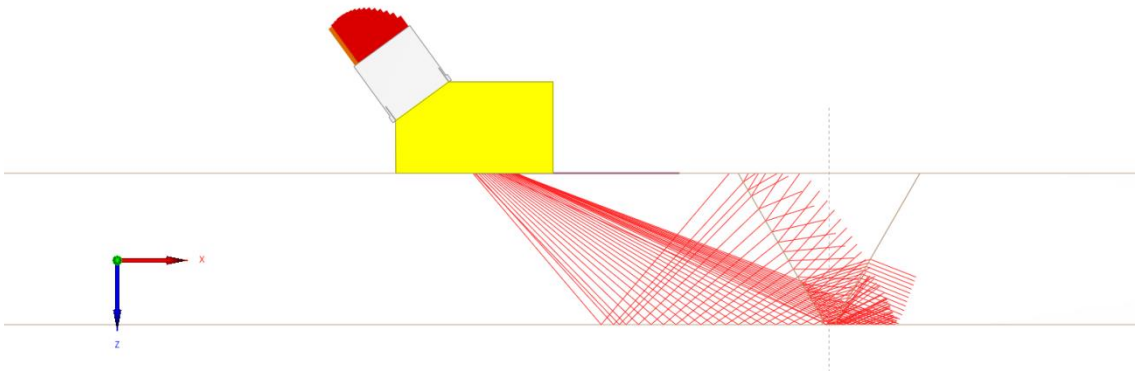

Figure 43 Civa simulation setup. Red lines represent the ray path from the delay laws

7. RESULTS AND ANALYSIS

This chapter presents the results acquired from the conducted tests. First the maximum amplitudes from the flaws are listed and compared with each other. Secondly signal-to-noise ratio was calculated from the measured noise for each flaw and compared against each technique. Letter labeling after the flaw number means the side the flaw was scanned e.g. flaw number 1a represents the average result for flaw number 1 scanned from the a side.

7.1 Maximum amplitudes

Maximum amplitude is the maximum signal response from a flaw. The lower the amplitude response is the more the ultrasonic wave has attenuated between the flaw and the ultrasonic transducer. In these tests flaw number 5 in the base material was chosen as a reference point so maximum signal response from this flaw would be approximately 80%. The scanning was repeated three times, so the represented values are the average maximum amplitudes of these results. The average maximum amplitudes from the tests can be seen summarized in Table 6 in Appendix B.

7.1.1 Linear phased array

For 2,25 MHz phased array probe there appeared slight variance in the measured data of the flaw number 5 from the a-side. It is probable that one scanning run may have suffered from the loss of couplant or the probe might not have been completely perpendicularly to the flaw. However the difference between the average of the results for sides a- and b-side is minimal. There is a large difference between the results for flaw number 2 from the a- and the b-side. This is due to the fact that on the case of 2b the scanning of the flaw is done through the weld whereas 2a is directly in front of the weld during the a-side scan, thus it is not affected by noise and attenuation from the weld. This occurrence can be observed for other probes as well with exception to the TRL probe. The results are shown in Figure 44, where also the average noise level of the two sides is represented as a line.

For 5 MHz linear phased array probe, the average of the results are shown in Figure 45. Larger deviation between the results was observed on the flaw number two from the a-side. The most probable reason for this deviation is the loss of couplant or misalignment of the probe in one of the three scanning runs in the vicinity of the flaw number two.

The assumed flawed scan was removed from the results, so for this probe on flaw number 2a is the average of only two results.

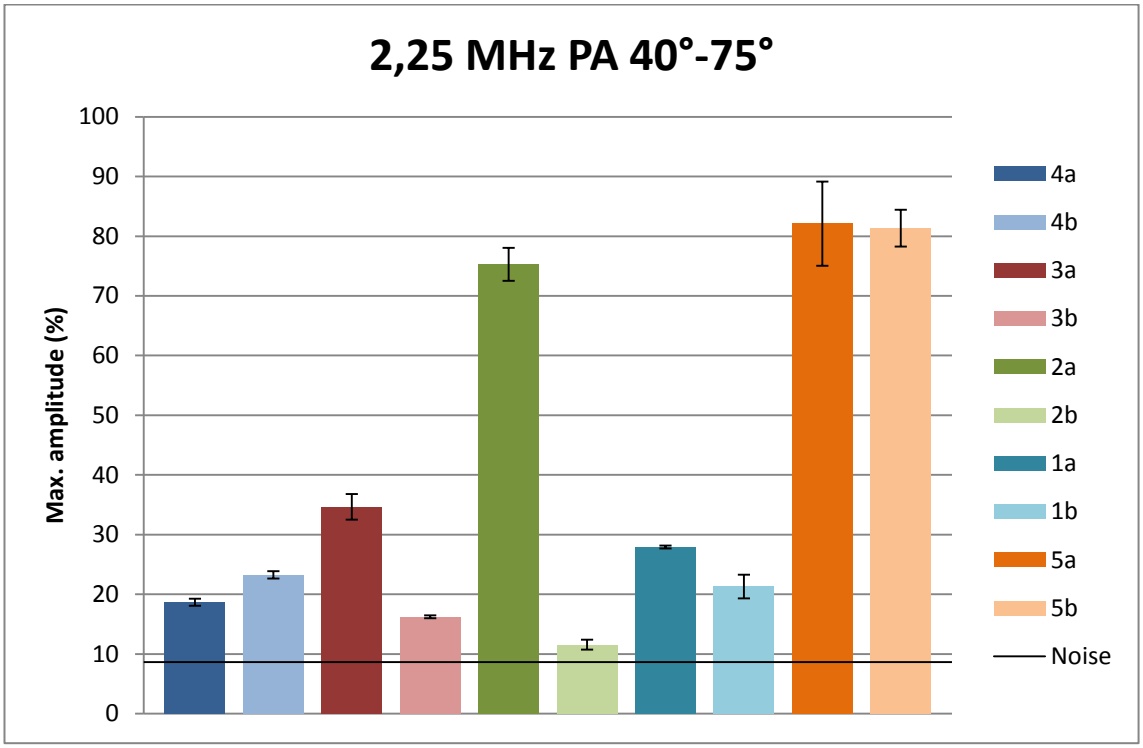

Figure 44 Average maximum amplitude with 2,25MHz probe

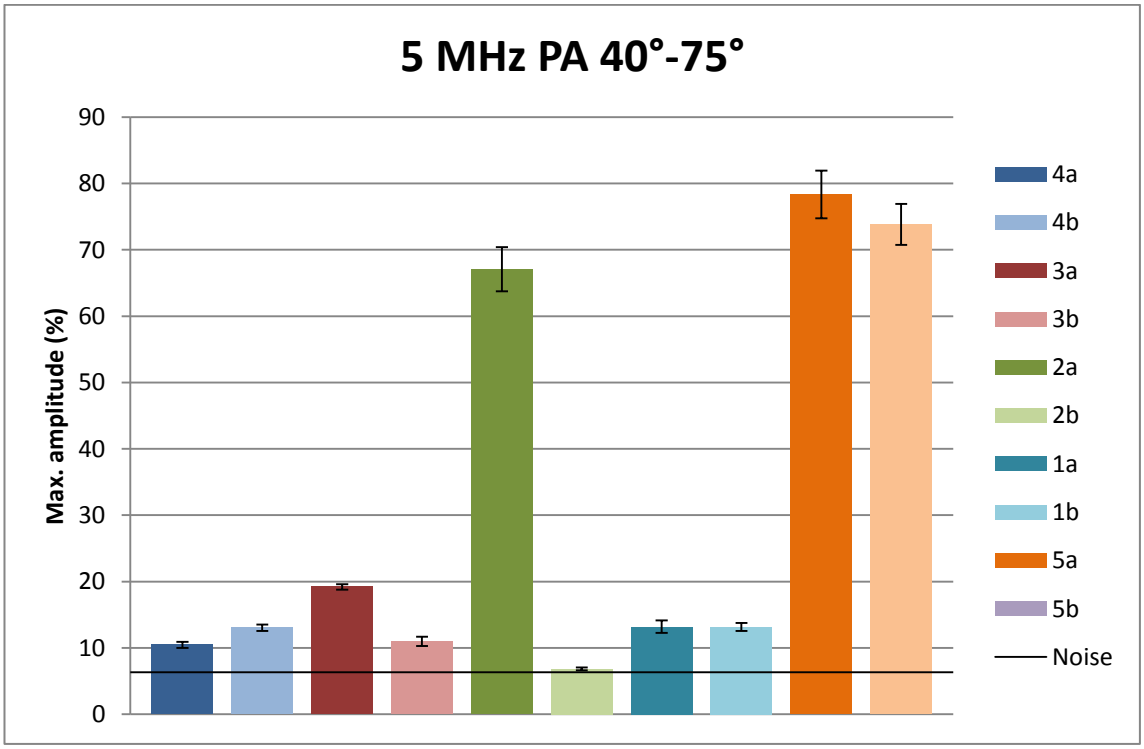

Figure 45 Maximum amplitude with 5MHz probe

When comparing the linear phased array probes together in Figure 46, the results for both linear phased array probes were consistent. The flaws closer to the probe and in front of the weld gave stronger amplitude response than the flaws further and behind the weld center.

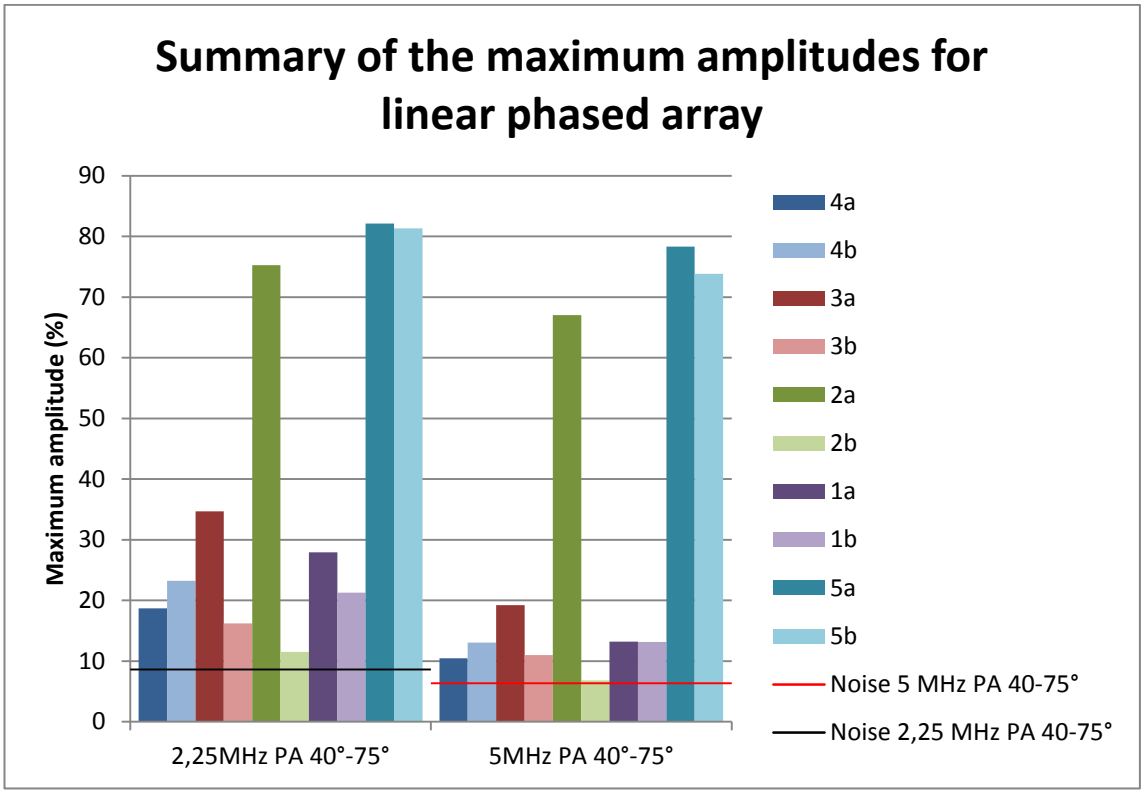

Figure 46 Summary of the two linear phased array probes

2,25 MHz probe gives overall the best maximum amplitudes of the two. This is reasonable, since according to theory, lowering the frequency lengthens the wavelength, thus the grain structure has smaller effect on the beam propagation.

7.1.2 Conventional ultrasound

The results for 2 MHz 45° conventional probe are presented in Figure 47. Stronger amplitude response was observed for flaw number 1 than for flaw number 4 from the b-side. Also, the flaw number 1 shows stronger amplitude response from the b-side than from the a-side. This contradicts the results from linear phased array inspections. Also the flaw number 4 is closer to the probe than the flaw number 1 on the b-side, so stronger maximum amplitude would be expected from the flaw number 4. The flaw number 2 on the other hand, shows stronger amplitude response than the reference flaw number 5.

Flaw number 1 was located almost in the middle of the weld (0,15 mm from the center), which would indicate that the maximum response should be roughly the same from either of the sides or slightly stronger on the a-side. Small deviation between the results

for flaw number 1 would indicate that probe may have been misaligned during the setup for the scan of the a-side or the probe used may not have been in working order.

Overall the results for 45° conventional probe do not deviate a lot from the expected results, thus the data can still be considered valid.

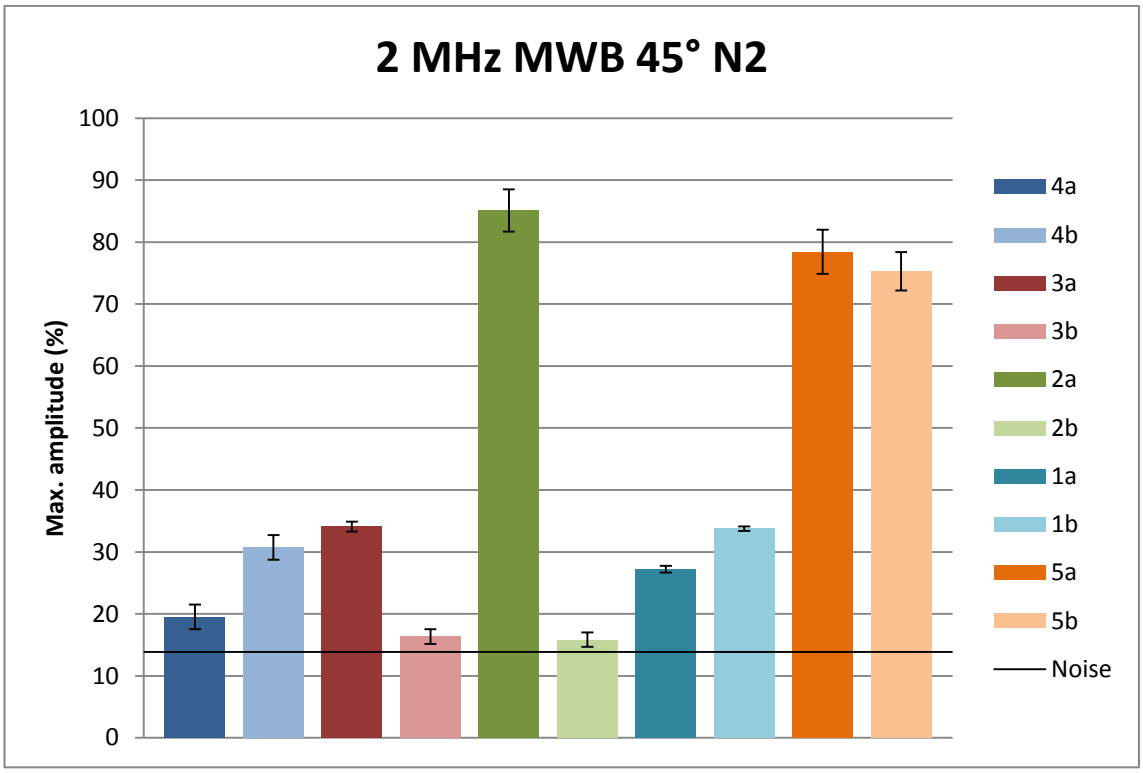

Figure 47 Maximum amplitude with conventional 45° probe

For 2 MHz MWB 60° probe, 1,5 dB soft gain was required to be added to 35 dB hardware gain in order to achieve the similar amplitude response for flaw number 5 as for 45° probe. This attenuation seems reasonable, since ultrasonic beam has to travel a longer distance from the transmitter to the flaw and back to the receiver for 60° probe than for 45° probe.

The results for 60° probe can be seen in Figure 48. Standard deviation is the strongest for flaw number 3 from the b-side. This is probably caused from the loss of couplant or slight misalignment of the probe in the vicinity of the flaw.

The flaws 3 and 1 existing roughly in the middle of the weld gave similar maximum amplitude response from the both measured sides, with b-side giving a lower response. This indication is as expected. There is not much difference between the scans from both sides for the reference flaw number 5. Hence, the results for conventional 60° probe can be considered accurate.

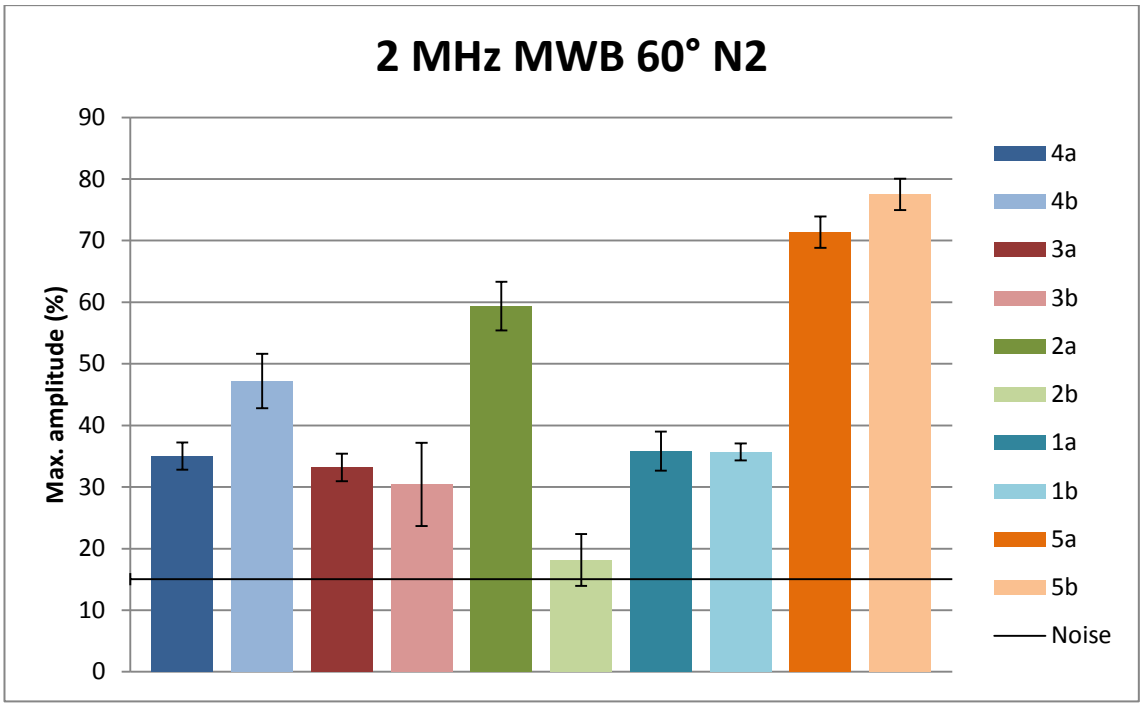

Figure 48 Maximum amplitude with conventional 60° probe

Summary of the results between conventional ultrasonic probes can be seen in Figure 49.

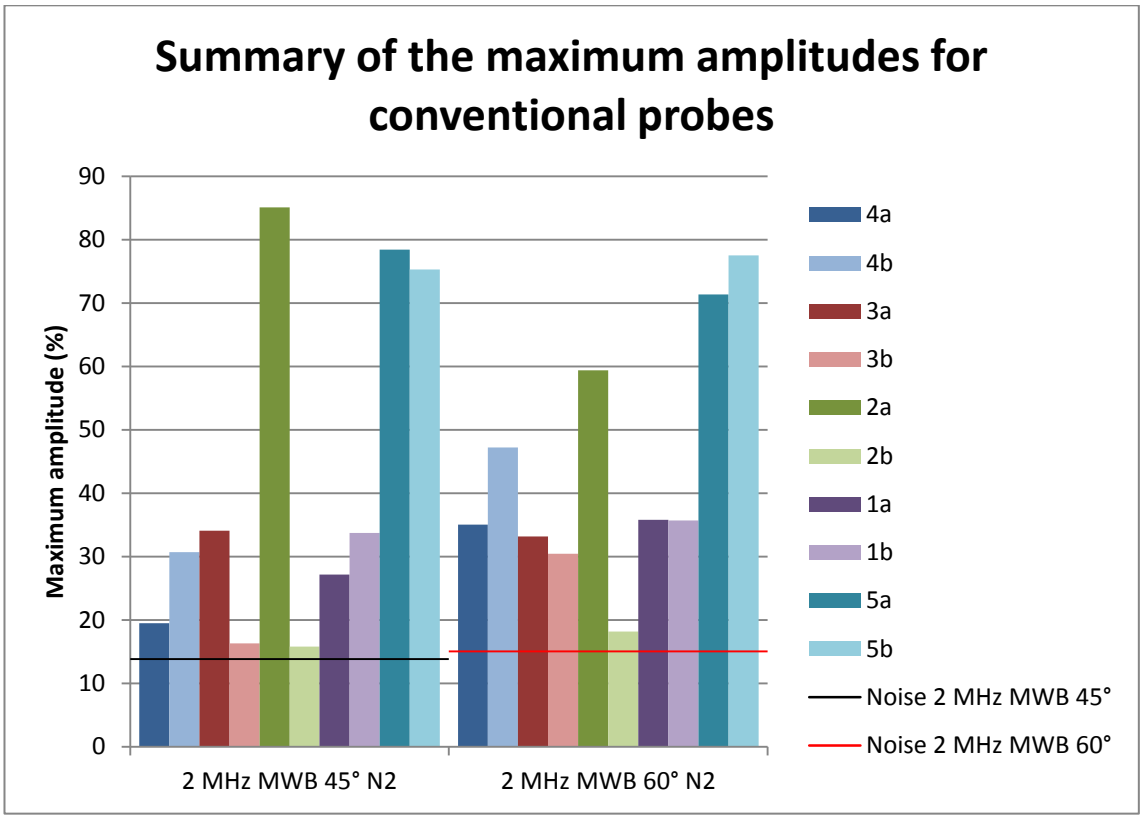

Figure 49 Summary of the two conventional probes

60° conventional probe gave roughly better amplitude responses than the 45° probe. With exception to flaw number 2 where 45° probe excelled over the 60° one from the a-side. This might be the cause of the shorter distance the ultrasonic beam from 45° probe has to travel compared to 60° probe. Also the flaw number 2 is not in the weld, but in front of it in the HAZ. Meaning ultrasonic beam does not suffer from excess attenuation at this location compared to the weld metal. From the b-side however the responses were roughly the same, with 60° probe slightly higher. For 60° the ultrasonic beam encounters the flaw in a more favorable angle than the 45° probe in this specimen, leading to stronger maximum amplitude indications.

7.1.3 Separate Transmit-Receive Longitudinal (TRL) dual-matrix phased array probe

The results from the TRL probe can be seen in Figure 50.

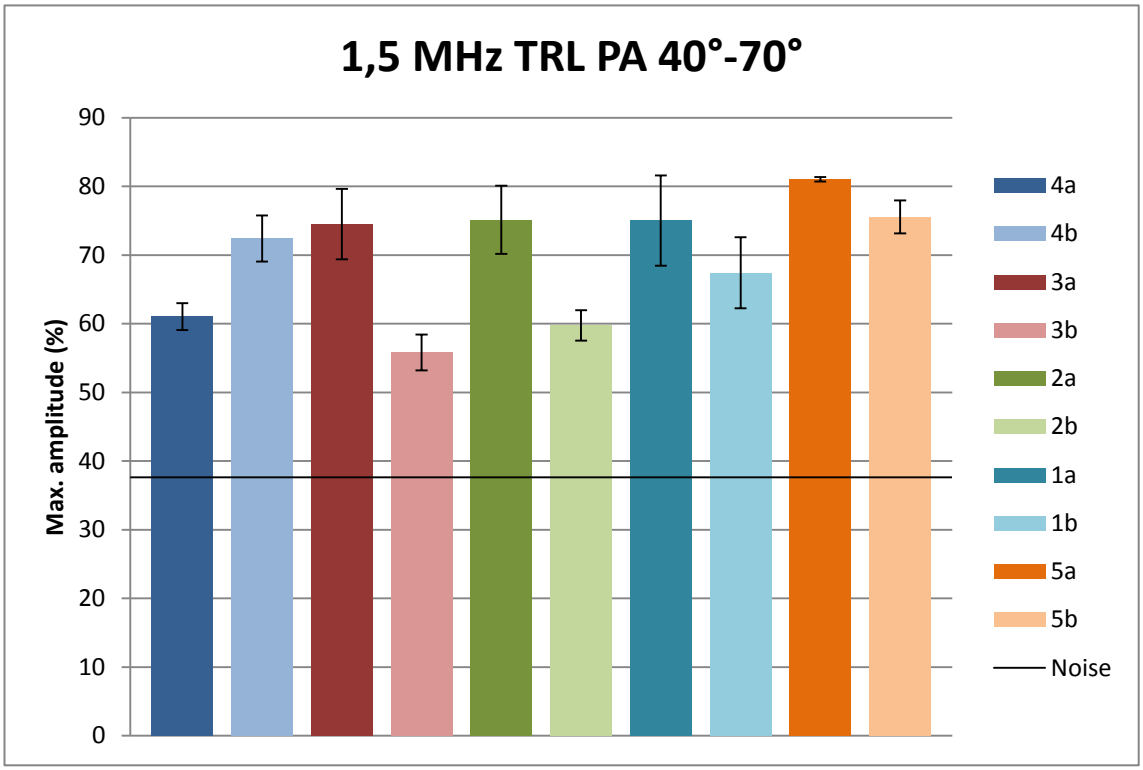

Figure 50 Maximum amplitude with TRL probe

The deviation between the results for the TRL probe seems average. Only unexpected result was from flaw number 3 having lower amplitude response from b-side than flaw number 2 from the b-side. There is not much deviation between the results acquired from flaw number 3, indicating there was no loss of couplant. It is possible that stronger amplitude response might be caused from the more favorable position of the flaw number 2 or the anisotropic structure of the weld might have been favorable at this location of the weld. For example the focus might have deviated from the weld structure straight to the flaw. Unlike the other probes, TRL gave three echo responses. First echo response was from direct longitudinal wave, because part the longitudinal wave mode converted to ~30° shear wave propagating slowly generates also the indirect longitudinal wave, which is the second echo response. The third echo response comes from the mode conversion from the shear wave to the back wall surface creeping wave. Due to mode conversions, the direct longitudinal wave has attenuated a lot thus maximum amplitude from the direct longitudinal wave is considerable low. However, the creeping wave gives really high maximum amplitudes regardless of the location of the flaw. Overall, the results can be considered reliable.

7.1.4 2,25 MHz linear phased array simulation

The results from the CIVA simulation can be seen in Figure 51.

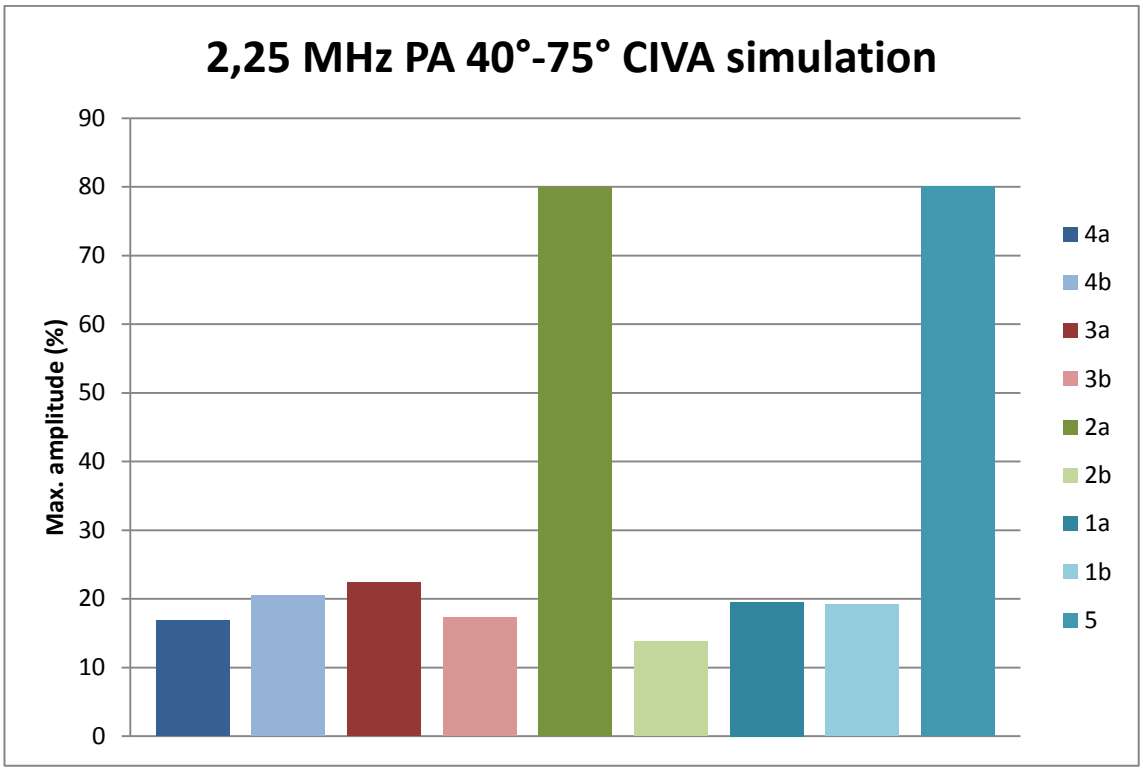

Figure 51 2,25 MHz PA 40-75° CIVA simulation

The results are consistent with the expected results. However, the difference between the a- and b-side of the simulated amplitude responses is smaller than expected. The used model might attenuate the ultrasound more than required. On the other hand, flaw number 2 and 5 gave almost the same amplitude responses. The reason for this kind of result could be that CIVA does not take into account the slight changes of the crystal structure in the HAZ and treats it as a normal base metal.

7.1.5 Summary of maximum amplitudes

The results for all the techniques for flaw numbers 1-4 can be seen in the Figure 52. In this figure the amplitude response was changed to decibels, where the acquired maximum amplitude in % was compared to a 100 % amplitude response as in equation below.

$$dB = 20 \log_{10} \frac{a_{max}\%}{100\ \%} \tag{17}$$

Weld center was chosen as a point of origin. The figure represents the distance from the weld center along the X-axis. The results are also combined to represent the scanning from the near side and the far side more clearly. This means that if the flaw location was

on the other side than the probe of the weld center, the flaw would be on the far side. If the flaw was located on the same side as the probe, the flaw would be on the near side. Near side and far side are shown in more detail in Figure 53 and Figure 54 respectively. The figures show how the austenitic weld attenuates the propagating ultrasonic wave, thus lowering the amplitude response.

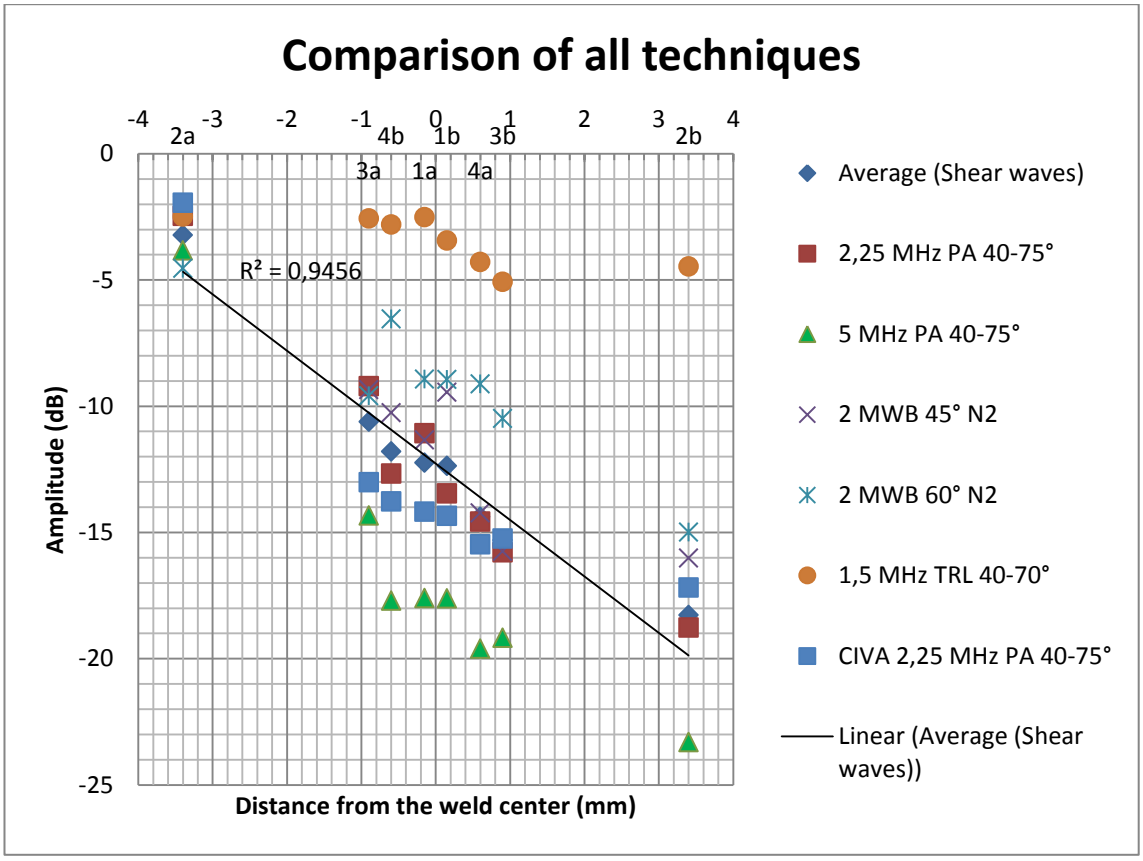

Figure 52 Comparison of all used techniques. 0 represents the weld center and the flaws are plotted along the X-axis according to their distance from the weld center. – represents the near side and + the far side

For the flaws within and in the vicinity of the weld, the flaw number 2 gave the highest amplitude response from the a-side for all probes and the lowest for the b-side, with exception of TRL probe where the flaw number 3 gave the lowest amplitude response from the b-side. This might be a consequence of a better deviation of sound beam to the flaw number 2 than flaw number 3 from the b-side. The probe had a skew angle of 15° so the deviation of the probe does not seem plausible.

When comparing all the techniques together, excluding these previous observations, the results seem consistent. TRL probe suffers the least from attenuation and the 5 MHz phased array probe the most, as expected. The reason for TRL probe to attenuate less than the other probes is due to the fact that TRL probe uses longitudinal waves whereas the other probes use shear waves. Also the frequency is lower than that of the other

probes, however this lowers the resolution and accuracy of the probe compared to other probes. The smallest detectable flaw is ~$\lambda/2$, leading to missing of smaller flaws by probes with lower frequency. The wavelengths can be seen in Table 5 in the previous chapter.

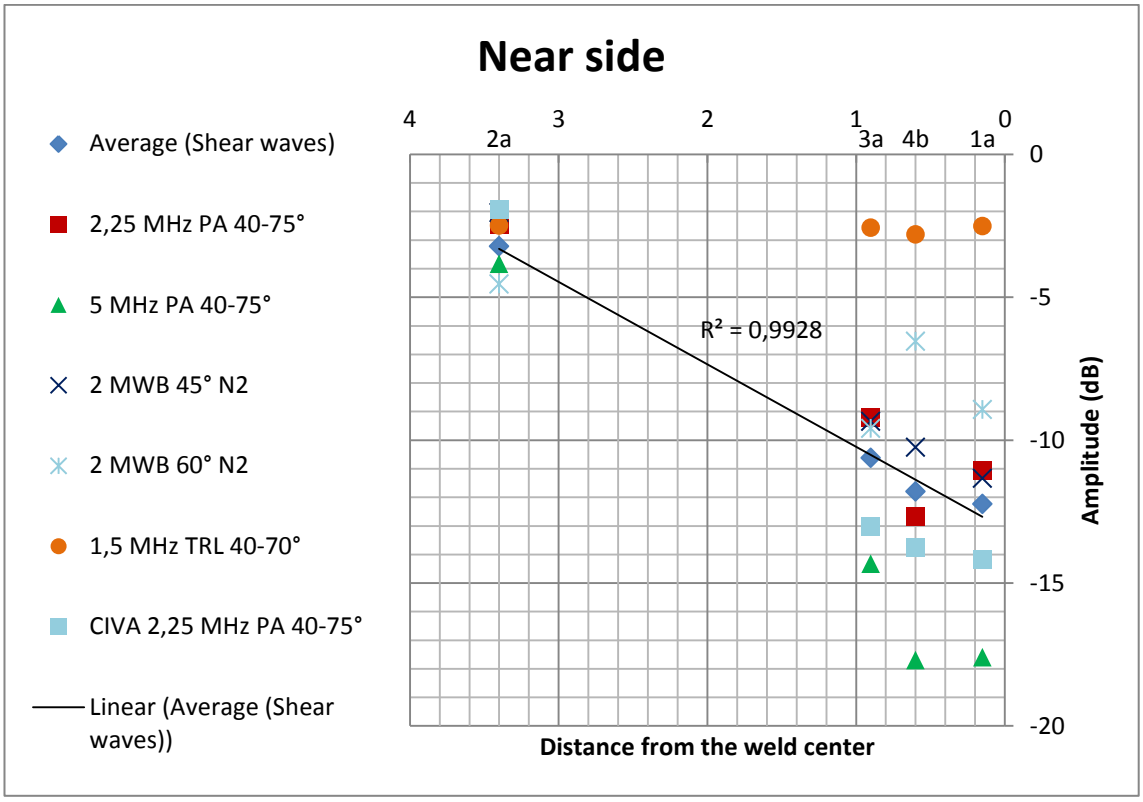

Figure 53 Results for the near side, 0 represents the weld center. Flaws 1a, 2a, 3a and 4b are considered as on the near side of the weld

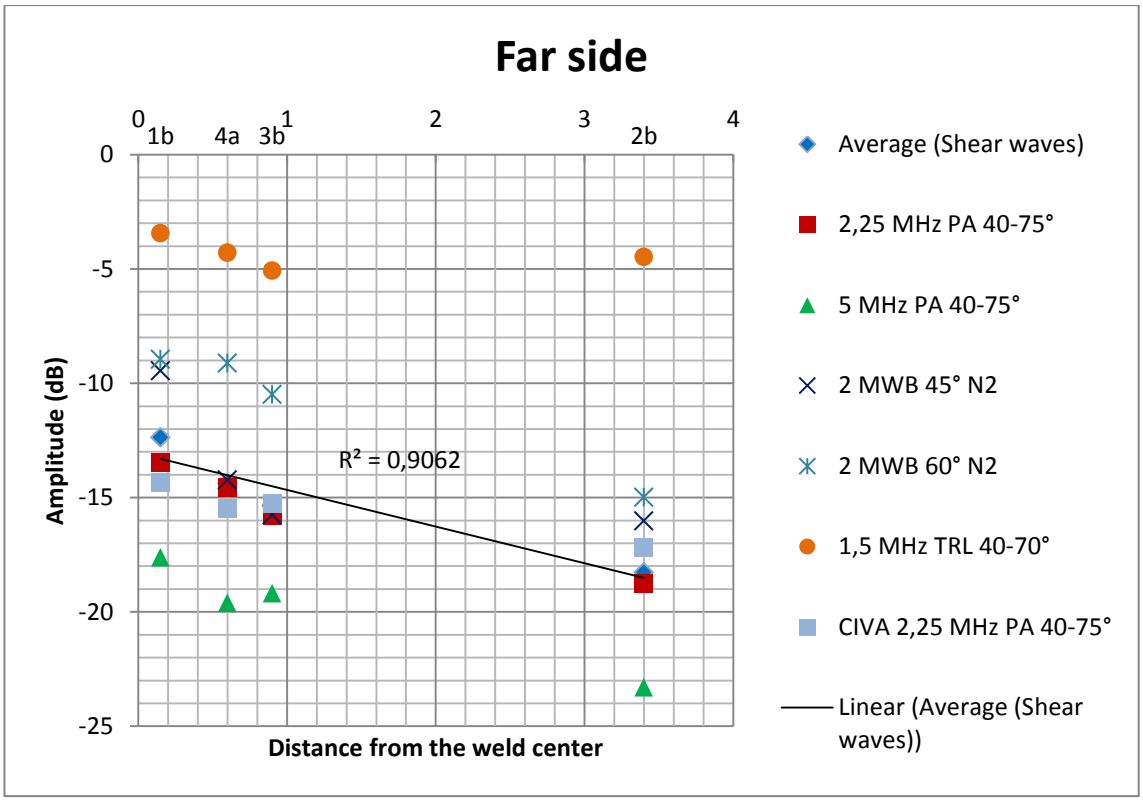

Figure 54 Results for the far side. 0 represents the weld center. Flaws 1b, 2b, 3b and 4a are considered as on the far side of the weld

The conventional 60° probe gave better amplitude response than the conventional 45° probe. The 60° probe excelled against the phased array probes while the 45° probe got roughly the same or slightly higher amplitude response as the 2,25 MHz linear phased array probe. Conventional probes had slightly lower nominal frequency than the linear phased array probes, however the difference between the results was higher than expected.

7.2 Signal-to-noise ratio (SNR)

A good SNR was determined as 3 to 1 according to the literature. It has been described as a line in the following figures. Since good SNR is usually determined 2 to 1 or 3 to 1, ratio of 3 to 1 was chosen for the most secure result. SNR is used to determine how well the flaw is distinguished from the noise, the higher the SNR the better the flaw stands out from the noise. SNR was calculated using simplified version of equation 6 with the acquired maximum amplitude response and maximum noise from the weld according to equation 18.

$$SNR = \frac{A_{flaw}}{A_{noise}} \tag{18}$$

Where A_{flaw} is the average maximum amplitude response for a flaw and A_{noise} is the average maximum noise level measured for the technique.

7.2.1 Linear phased array

SNR of the linear phased array probes 2,25 MHz and 5 MHz can be seen in Figure 55 and Figure 56 respectively.

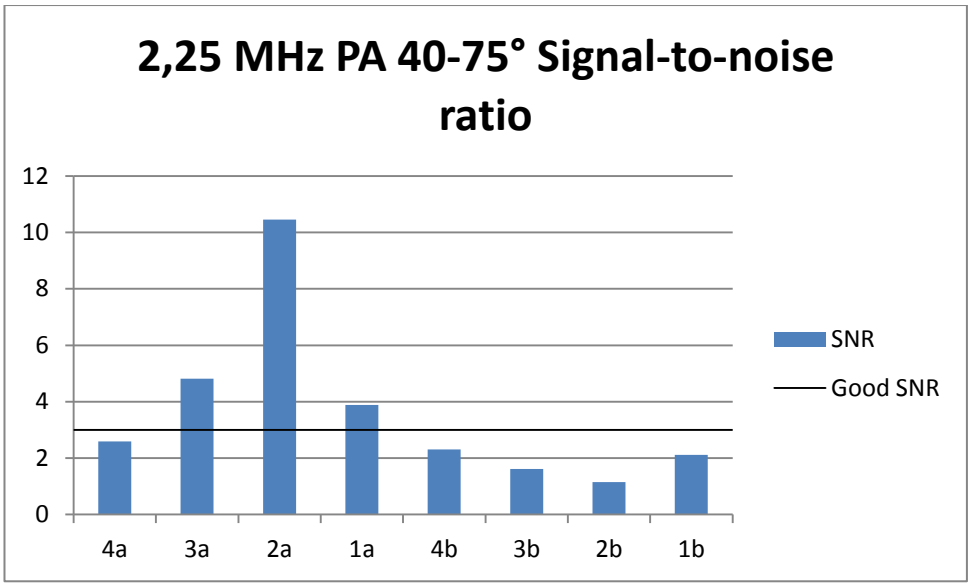

Figure 55 2.25L16A10 signal-to-noise ratio

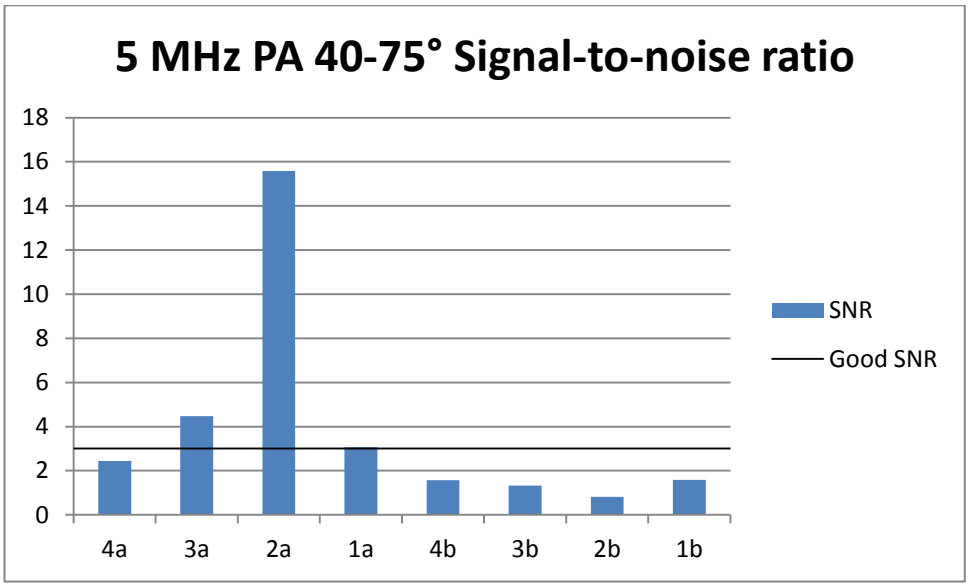

Figure 56 5L16A10 signal-to-noise ratio

For linear phased array, the flaws 3-1 achieve good SNR. Flaw number 4 is barely distinguished from the noise from both of the sides.

When comparing the scan images for linear phased array from Figure 57 and Figure 58 all the flaws are noticeable from the a-side, especially for flaw number 2. However, it is

difficult to be certain whether the flaw numbers 4 and 1 are flaws or just noise. From the b-side the flaw number 3 is barely visible and the flaw number 2 cannot be noticed at all. Even though the SNR for the flaws number 4 and 1 is less than 3, it is possible to recognize them as real flaws from the noise.

One way to enhance the scan image is to increase the soft gain. The effect is almost the same as increasing gain, but this can be done after scanning with the analysis software. In Figure 59 and Figure 60, 12 dB soft gain has been applied, rising the overall gain to 30 dB. In these figures all flaws are clearly visible from both sides in exception to flaw number 2 from b side. Soft gain raises the noise level as well, thus the flaw number 2 from the b-side cannot stand out from the noise even with the applied extra gain.

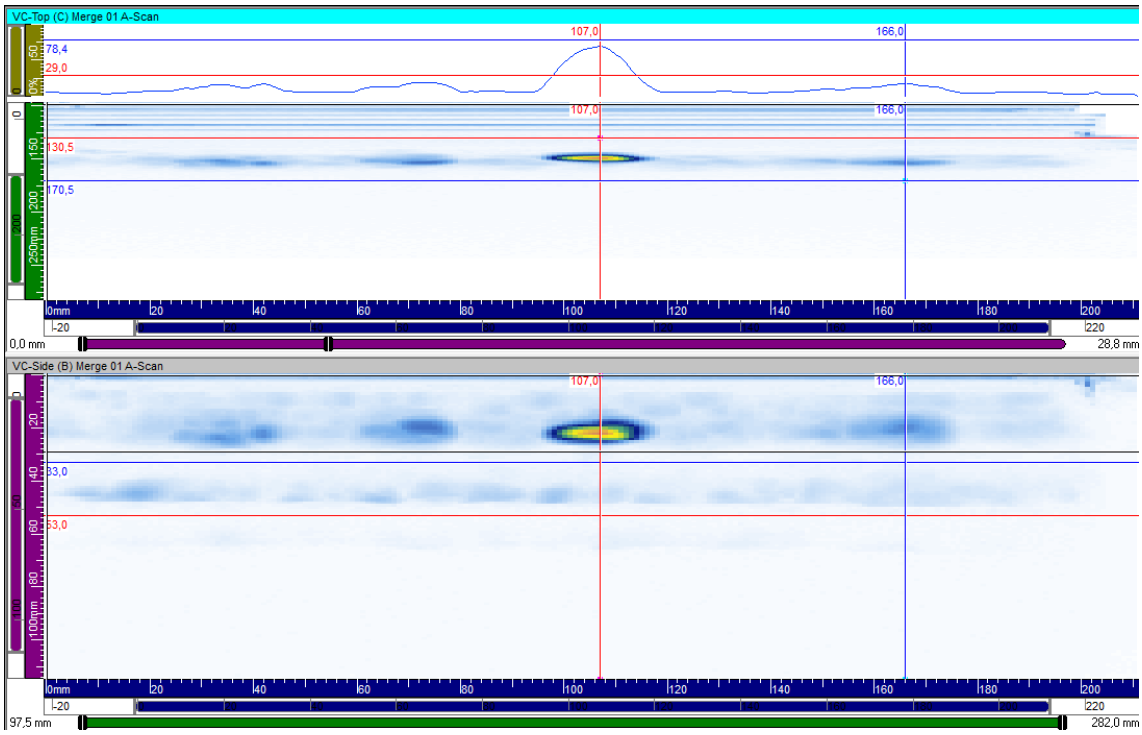

Figure 57 2L16A10 a-side volume corrected top and side image. The flaws are 4-1 from left to right respectively.

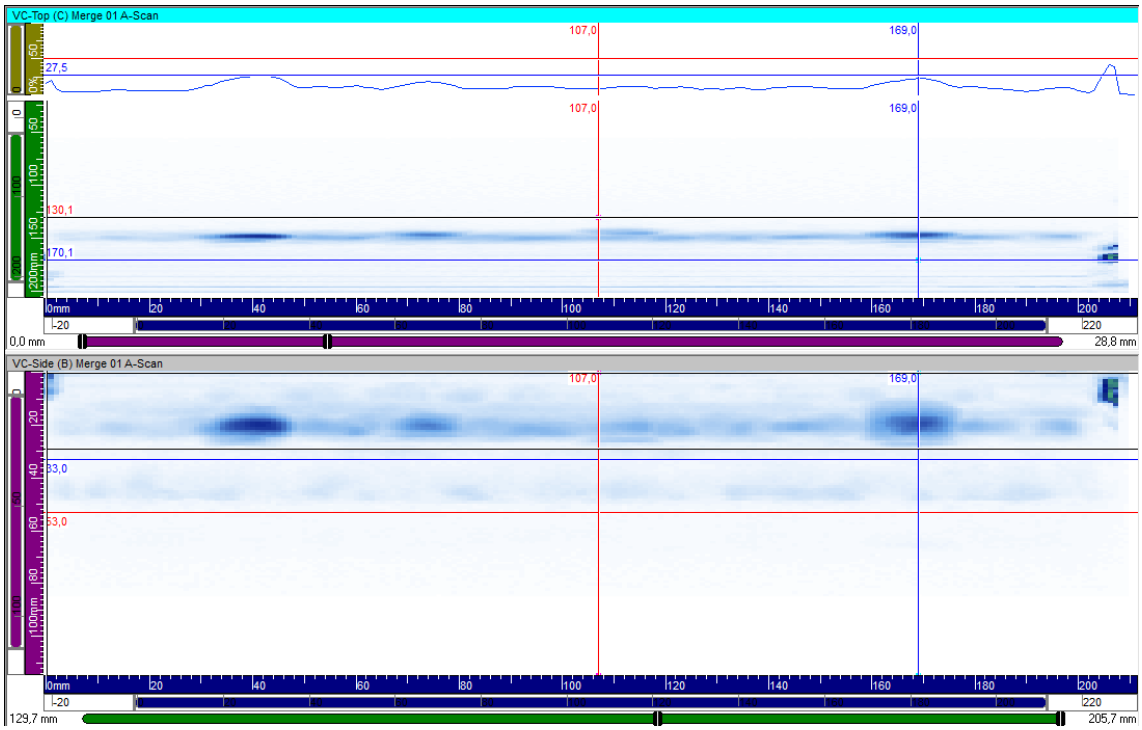

Figure 58 2L16A10 b-side volume corrected top and side image. The flaws are 4-1 from left to right respectively.

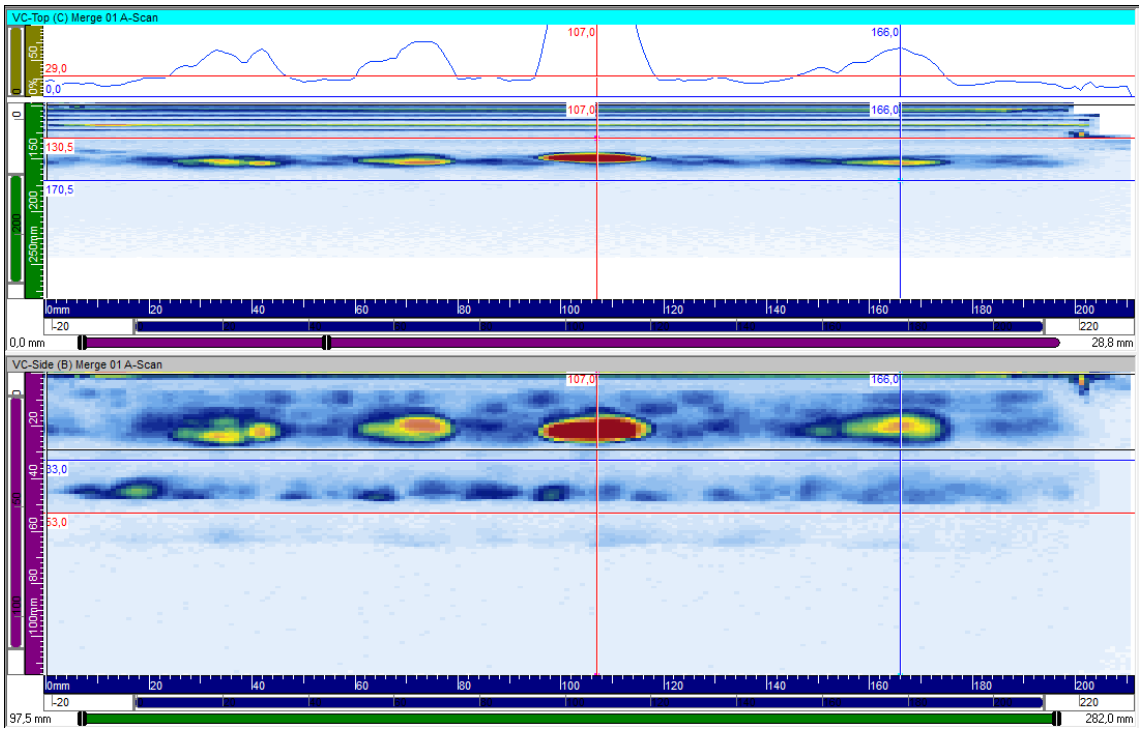

Figure 59 2L16A10 a-side volume corrected top and side image. The flaws are 4-1 from left to right respectively. 12dB soft gain

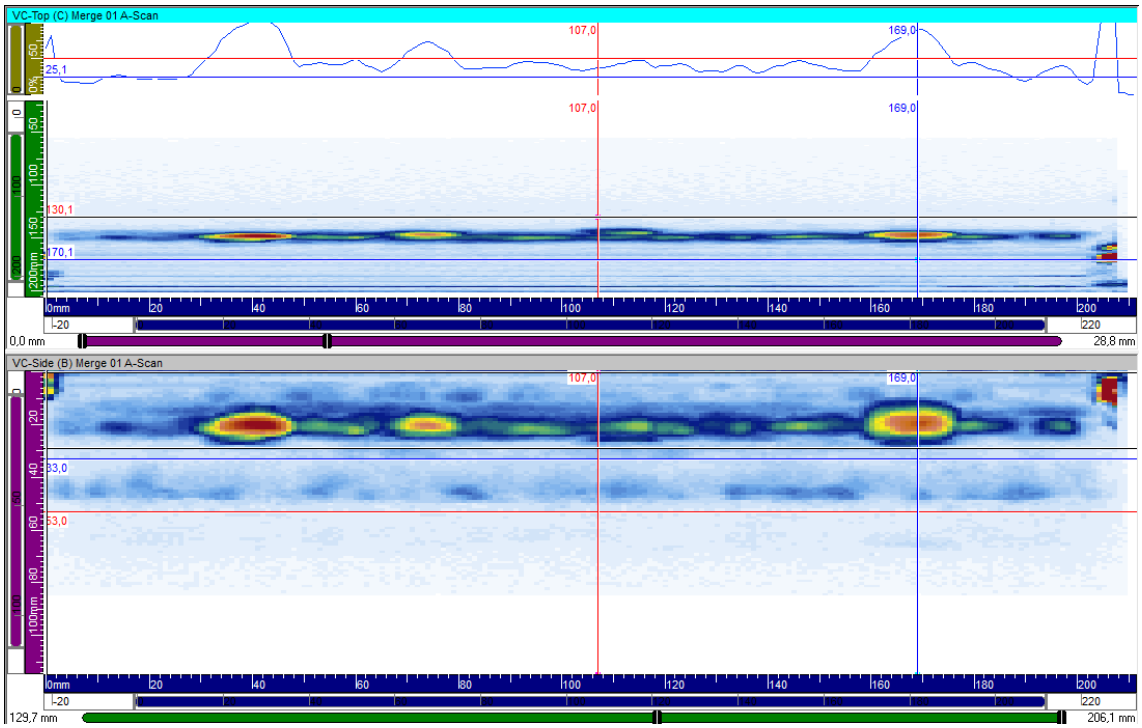

Figure 60 2L16A10 b-side volume corrected top and side image. The flaws are 4-1 from left to right respectively. 12dB soft gain

7.2.2 Conventional ultrasound

SNR for conventional 2 MHz 45° and 60° probes can be seen in Figure 61 and Figure 62 respectively

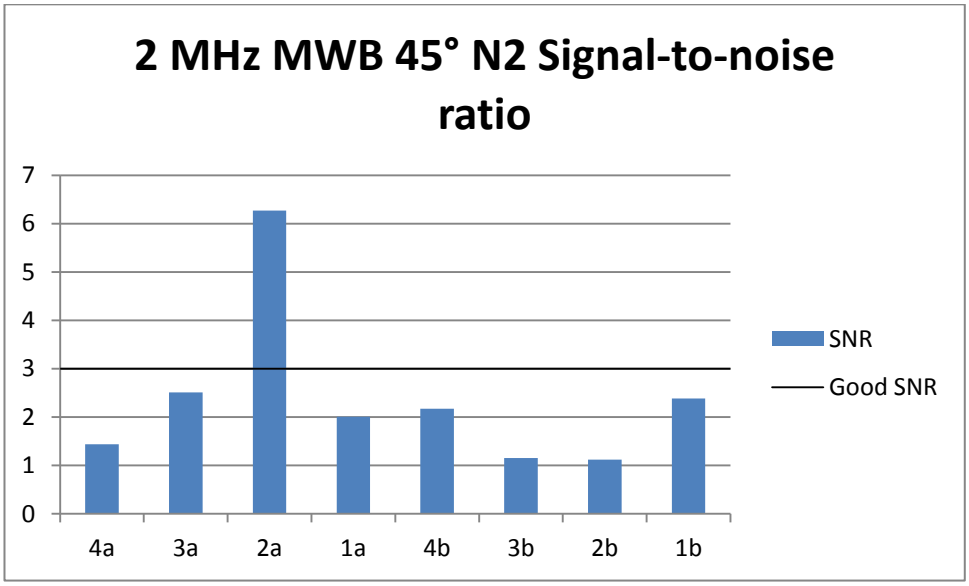

Figure 61 2 MHz MWB 45° N2 Signal-to-noise ratio

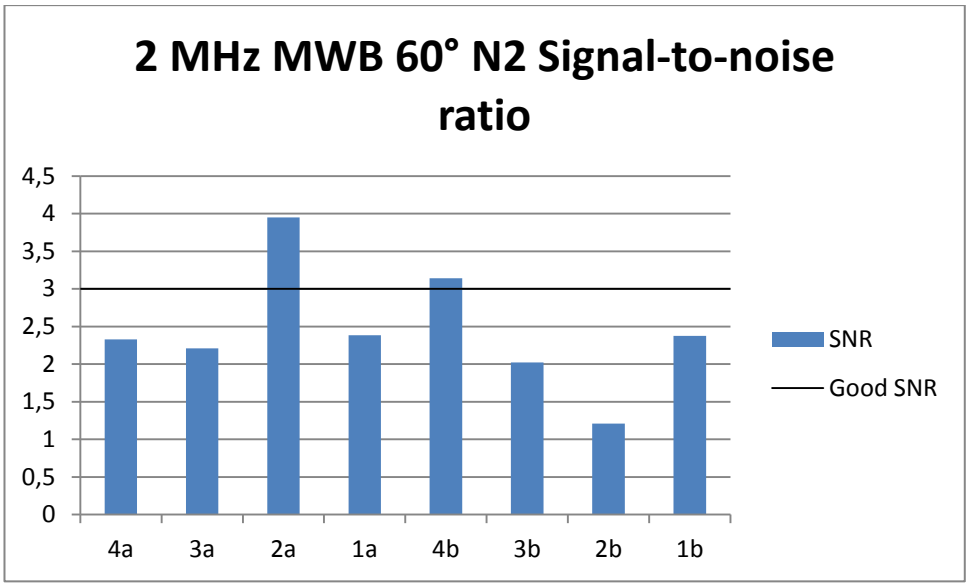

Figure 62 2 MHz MWB 60° N2 Signal-to-noise ratio

Noise was a disturbing factor for conventional probes and a good SNR was achieved only for flaw number 2 for a-side for both probes and flaw number 4 on b-side for 60° probe. It can be seen from the figures that the more there is distance between the probe and the flaw, the more the SNR seems to deteriorate.

7.2.3 Separate Transmit-Receive Longitudinal (TRL) dual-matrix phased array probe

SNR for the TRL probe can be seen in Figure 63.

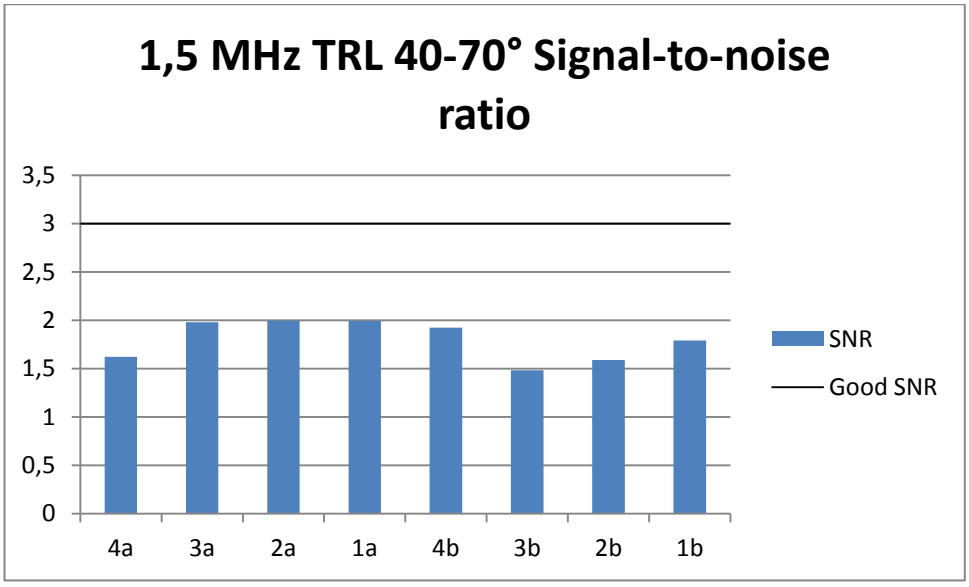

Figure 63 1,5 MHz TRL 40-70° Signal-to-noise ratio

To get a clearer view of the ultrasonic image created from the TRL measurement data, data cursor adjustments had to be made. Unadjusted result can be seen in

Figure 64 and the adjusted results can be seen in Figure 65. The depth was set to 22,1 mm in order to remove un-necessary echoes from the image. However, this still left a geometric echo from the middle of the weld groove as noise. This noise was determined as geometrical echo, since it was consistent along the weld almost completely.

Even though all the flaws can be seen clearly from the both sides with TRL probe, a good SNR cannot be achieved with any of the flaws. This is due to the noise from the middle of the weld groove, which was measured an average of over 37%. Meaning no signal response from the flaws could achieve a good SNR. This high noise level might lead to missing of smaller flaws during an inspection.

It has to be taken into account that since the exact number and the location of the flaws is known, it is easier to determine the flaw from the noise. For this reason SNR is a good measure to determine how well the flaw actually distinguishes from the structural noise.

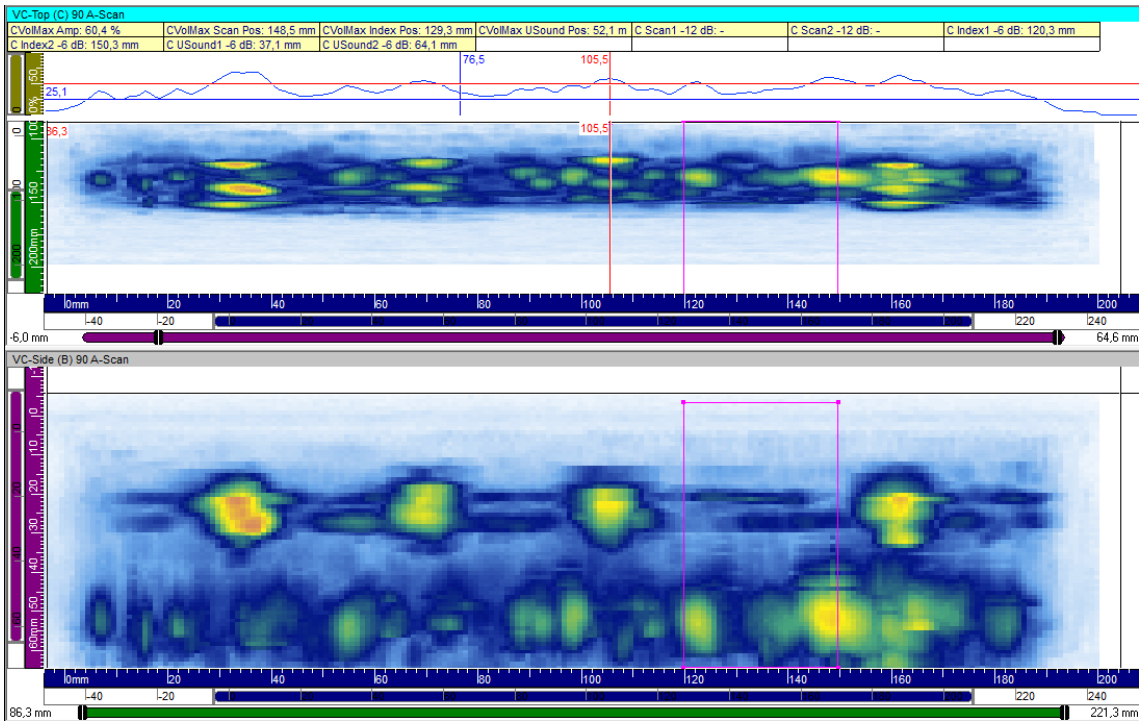

Figure 64 1,5 MHz TRL 40-70° b-side volume corrected top and side image. The flaws are 4-1 from left to right respectively. Unadjusted data

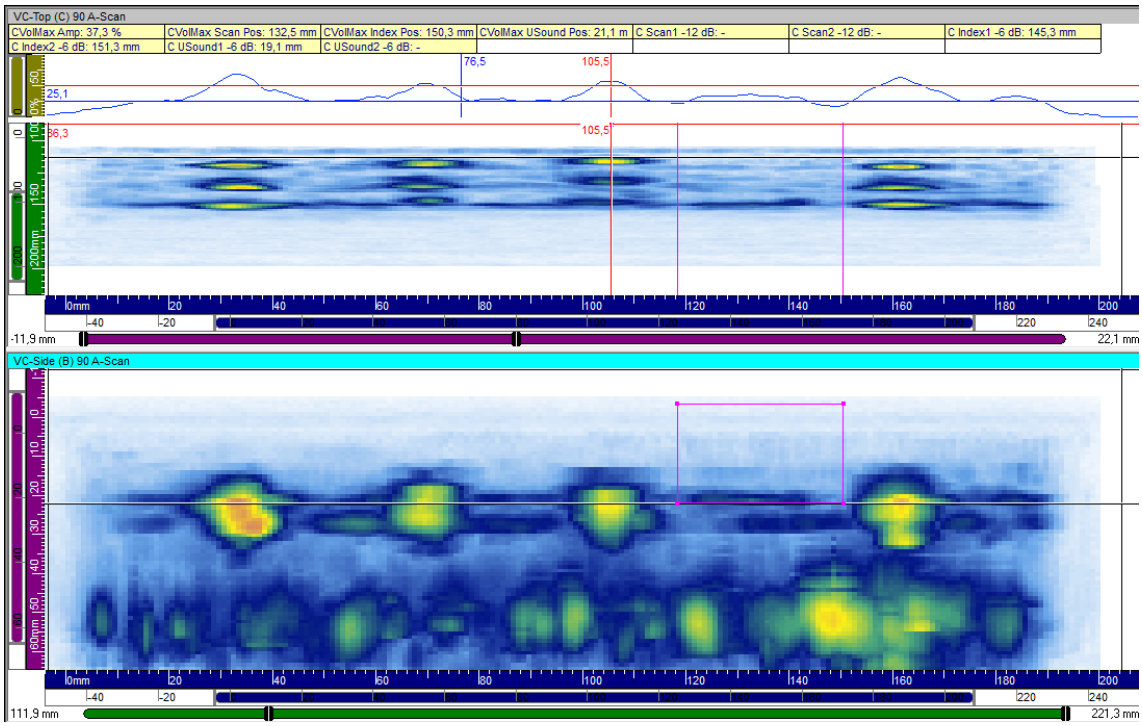

Figure 65 1,5 MHz TRL 40-70° b-side volume corrected top and side image. The flaws are 4-1 from left to right respectively. Adjusted data

7.2.4 Summary of signal-to-noise ratios

Signal-to-noise ratio (SNR) results are summarized in Figure 66.

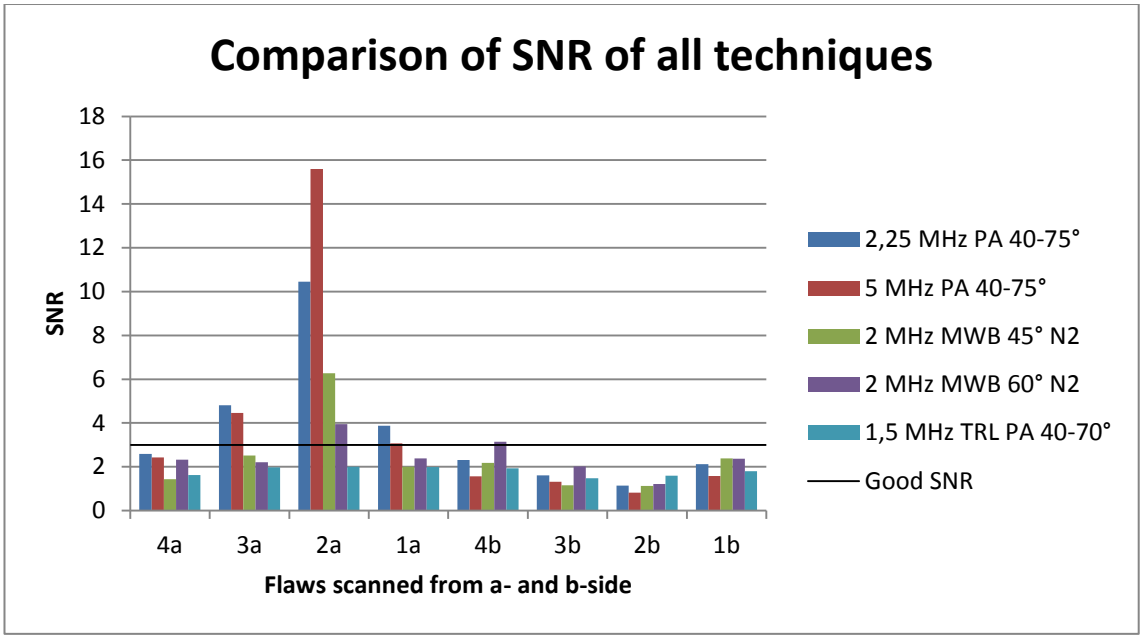

Figure 66 Comparison of signal-to-noise ratios of all techniques for a- and b-side

For linear phased array probes, flaw numbers 1-3 gave a good SNR from the a-side. However, when scanning through the weld, shear wave probes were unable to reach good SNR in any of the artificial flaws with only exception of 60° conventional probe, which was the only probe achieving a good SNR from flaw number 4.

Despite having the worst overall results for SNR, the SNR of TRL does not improve or reduce much depending on the location of the flaw. TRL actually gave the best SNR for the flaw number 2 from the b-side.

The probes are compared to each other in Table 9 in Appendix B: Results. The best SNR for each flaw was given 4 points and 0 to the worst SNR. The points were summed together and 2,25 MHz linear phased array probe achieved the best overall score. 5 MHz linear phased array probe had the best SNR when scanning the flaw number 2 from the a-side. This is expected, since there is not much noise for 5 MHz noise and the ultrasonic wave has not yet attenuated by the anisotropic weld at all since the flaw was located outside the weld.

8. DISCUSSION

8.1 Observations

The test piece was an austenitic stainless steel weld and it was scanned with linear phased array, conventional and TRL 2D matrix phased array techniques. The test piece was also modelled into CIVA software and tested with linear phased array. Maximum amplitudes from the flaws were recorded and SNR was calculated from the achieved results.

Linear phased array probes had an excellent signal-to-noise ratio compared to other probes. Furthermore, attenuation was so strong that the flaws scanned through the weld were not recognizable.

Conventional probes fared surprisingly well in the conducted experiments. However, when compared to other techniques scanning with conventional probes was significantly slower than for the phased array probes. This was due to that the beam angle stayed the same, covering a narrower area compared to the phased array sectorial scan of 40-75°. So in order to get the best possible result, the step size along the X-axis had to be changed to 2 mm. Also the conventional probes were more susceptible to amplitude loss from misalignment or loss of couplant.

TRL probe gave the strongest amplitude responses from the flaws. Its advantages were the utilization of longitudinal waves and by mode conversion creeping waves, lower frequency and separate elements transmitting and receiving. The 15° skew angle did not give much of an advantage. However it may have reduced possible amplitude loss if the probe was not completely perpendicular to the flaw. The downside of the TRL probe is also the longitudinal waves. Since longitudinal waves also mode convert to shear waves and creeping wave during the inspection at the interfaces, analysis is not as straight forward as for only shear wave probes. It was important to set the data cursors to right depth in order to prevent excess noise from mode converted signals. Still the noise level was a limiting factor for this technique.

It must be noted that the gain in the experiment was set according to the maximum amplitude response from flaw number 5. It is possible to detect the flaws 4, 3 and 1 through the weld as well with linear phased array probes and conventional probes by increasing the soft gain or normal gain. However, comparing the maximum amplitude responses with each other would be impossible since most of the flaws would have 100% amplitude response with high gain setting. One plausible way would be to record

the gain for each flaw with a constant amplitude response and compare the difference. However, this experiment method would take a lot of time to conduct.

CIVA simulation software proved to be a useful tool in simulating ultrasonic probes and welds. However, setting the parameters of the weld, probe and the specimen geometry is not a straightforward process. In order to achieve the best possible result, there is a requirement for accurate information on the microstructure of the weld. Also the HAZ needs to be taken into account separately for more accurate results. Without these values CIVA can only give indicative results.

Testing setup was not an ideal one, since the scanner was moved manually, causing some possible deviation of the results. Also the attachment point for the probes seemed to move a bit during the scanning, causing the slight misalignment of the probe during scanning. Water acted as a good couplant between the probe and the specimen. However it was applied also manually, which may have caused loss of couplant during some parts of the scan.

EDM notches performed well as artificial flaws. The flaws were hard to detect through the weld and gave strong amplitude response in front of the weld as expected. Even though they are just rough estimates of a real flaw they give an excellent and cheap option to study ultrasonic attenuation in different locations of the weld.

8.2 Improvements

8.3 Testing arrangement

The manually moved scanner could be changed to automated scanner equipment in order to remove the human factor from the moving of the probe. Also the probe should be mounted solidly and constantly perpendicular to the weld during the inspection.

Water could be applied constantly in order to assure maximum contact. Other option would be to immerse the specimen completely in water. It would be possible to immerse the specimen completely in the water, but in a way so the probe would not be completely immersed, preventing the need for specialized immersion probes.

These improvements would reduce the deviation between the results and also give as reliable results as possible.

8.4 Use of simulation to probe development

It is feasible to use simulation tools in designing probe parameters. Simulation software could be used to determine the best possible probe angle, frequency and other parame-

ters depending on the structure and the geometry of the austenitic stainless steel component. This would save costs of producing multiple test probes and wedges and also time.

8.5 3D-printing as flaw production mechanism

It might be possible to use 3D printing to produce artificial flaws more easily or more accurately. This would give the possibility to produce embedded flaws with no surface contact or cracks similar to thermal or mechanical fatigue cracks with precise values and parameters. In this case, there would be no need to destroy the test piece in order to analyze the flaws accurately or thoroughly conducting non-destructive test with various methods aka fingerprinting the test pieces since there would be an accurate CAD drawing of the flaw. However the crack tip would not be as sharp as for a mechanical or thermal fatigue flaw and there might not be stresses around the crack tip either. Also it has to be noted that the 3D-printer should also fabricate the austenitic weld structure in order to create similar propagation conditions for ultrasound. Unfortunately there is little or no research regarding the subject. [86]

9. CONCLUSIONS

Ultrasonic inspection of austenitic stainless steel welds is difficult due to the anisotropic and dendritic structure of the weld. This causes scattering, distortion, deviation and attenuation of the ultrasonic wave, complicating the conducted inspection.

Artificial flaws are used to study the capability of an ultrasonic method to detect flaws of different sizes and locations. The electric discharge machining (EDM) notches used in this thesis proved to be a reasonable way to produce rough estimates of a crack. The artificial flaws gave expected amplitude responses from different locations of the weld metal. The responses varied also with different ultrasonic techniques used in the experiments.

Maximum amplitudes were the strongest for the 1,5 MHz separate transmit-receive longitudinal wave (TRL) 40-70° matrix probe and the lowest for 5 MHz linear phased array probe. However, signal-to-noise ratio (SNR) was the best for 2,25 MHz linear phased array probe and the worst for the TRL probe. CIVA simulation represented the ultrasonic propagation of 2,25 MHz phased array probe fairly well, so it can be assumed that with more accurate modeled structure of the weld there can be reliable results from the simulation as well. When scanning through the weld, only TRL probe could detect the furthest flaw with creeping waves. This would indicate that it would be advisable to use this technique when inspection from both sides of the weld is not possible.

The results were congruent with the theory and the literature search. When frequency of the probe was lowered, the amplitude response was stronger. Also creeping wave proved to give an excellent amplitude response for TRL probe and it did not suffer from attenuation as much as the shear waves.

The aim of this thesis was to study artificial flaws in austenitic stainless steel. It can be concluded that it is feasible to study the propagation of ultrasound in austenitic stainless steel with artificial flaws and also to use simulation tools to support the achieved results from experimental tests.

REFERENCES

[1] J.K.L. Lai, C.H. Shek, K.H. Lo, A General Introduction to Stainless Steels, in: J.K.L. Lai, C.H. Shek, K.H. Lo (Eds.), Stainless Steels : An Introduction and Their Recent Developments, Bentham Science Publishers, SAIF Zone, Sharjah, UAE, 2012, pp. 3–7.

[2] J. William D. Callister, Chapter 11 Applications and Processing of Metal Alloys, in: Material Science and Engineering an Introduction, 7th ed., John Wiley & Sons, Inc, 2007, pp. 364–365.

[3] J.C. Lippold, D.J. Kotecki, 1.3 Types of Stainless Steel and Therir Application, in: Welding Metallurgy and Weldability of Stainless Steels, John Wiley & Sons, Inc, New Jersey, 2005, pp. 4–5.

[4] J.K.L. Lai, C.H. Shek, K.H. Lo, Austenitic Stainless Steels, in: J.K.L. Lai, C.H. Shek, K.H. Lo (Eds.), Stainless Steels : An Introduction and Their Recent Developments, Bentham Science Publishers, SAIF Zone, Sharjah, UAE, 2012, pp. 23–40.

[5] C. Schaschke, A Dictionary of Chemical Engineering, Oxford University Press, 2014.

[6] H. Bhadeshia, R. Honeycombe, 12 Stainless steel, in: Steels : Microstructure and Properties, Elsevier Science, Burlington, 2006, pp. 259–285.

[7] D. Féron, E. Herms, B. Tanguy, Behavior of stainless steels in pressurized water reactor primary circuits, Journal of Nuclear Materials. Vol. 427 2012 , pp. 364–377.

[8] H. Bhadeshia, R. Honeycombe, 13 Weld Microstructures, in: Steels: Microstructure and Properties, Elsevier, Burlignton, 2006, pp. 287–306.

[9] H. Bhadeshia, R. Honeycombe, 4 The Effects of Alloying Elements on Iron-Carbon Alloys, in: Steels : Microstructure and Properties, Elsevier Science, Burlington, 2006, pp. 71–92.

[10] H. Bhadeshia, R. Honeycombe, 1 Iron and its Interstitial Solid Solutions, in: Steels : Microstructure and Properties, Elsevier Science, Burlington, 2006, pp. 2–16.

[11] NDT Education Resource Center, Materials and processes: Primary Metallic Crystalline Structures (BCC, FCC, HCP), web page. Available (accessed 09/2015) https://www.nde-ed.org/EducationResources/CommunityCollege/Materials/Structure/metallic_structures.htm.

[12] M.P. Ryan, D.E. Williams, R.J. Chater, B.M. Hutton, D.S. McPhail, Why stainless steel corrodes, Nature. Vol. 415 2002 , pp. 770–774.

[13] D.L. Harrod, R.E. Gold, R.J. Jacko, Alloy optimization for PWR steam generator heat-transfer tubing, Jom. Vol. 53 2001 , pp. 14–17.

[14] J. William D. Callister, Chapter 17 Corrosion and Degradation Of Materials, in: Material Science and Engineering an Introduction, 7th ed., John Wiley & Sons, Inc, 2007, pp. 644–645.

[15] B.S. Dutt, G. Sasikala, G. Shanthi, S. Venugopal, M.N. Babu, P.K. Parida, et al., Mechanical Behaviour of SS 316 (N) Weld after Long Term Exposure to Service Temperatures, 11th International Conference on the Mechanical Behavior of Materials (ICM11). Vol. 10 2011 , pp. 2725–2730.

[16] V. From, Product Data Sheet, AK Steel, web page. Available (accessed 09/2015) http://www.aksteel.com/pdf/markets_products/stainless/austenitic/316_316l_data_sheet.pdf.

[17] J.C. Lippold, D.J. Kotecki, 6.1 Standard Alloys and Consumables, in: Welding Metallurgy and Weldability of Stainless Steels, John Wiley & Sons, Inc, New Jersey, 2005, pp. 143–146.

[18] A.K. Steel, MSDS 321 Stainless steel, AK Steel, web page. Available (accessed 09/2015) http://www.aksteel.com/pdf/markets_products/stainless/austenitic/321_data_sheet.pdf.

[19] American Iron and Steel Instiute, Welding Processes for Stainless Steels, in: Welding of Stainless Steels and Other Joining Methods, 1988, pp. 15–32.

[20] J.C. Lippold, D.J. Kotecki, 6.5 Weldability, in: Welding Metallurgy and Weldability of Stainless Steels, John Wiley & Sons, Inc, New Jersey, 2005, pp. 173–199.

[21] D. Kotecki, F. Armao, Stainless Steels Welding Guide, Lincoln Electric Company. 2003 , pp. 15–17.

[22] J.C. Lippold, D.J. Kotecki, 6.3 Welding metallurgy, in: Welding Metallurgy and Weldability of Stainless Steels, John Wiley & Sons, Inc, New Jersey, 2005, pp. 151–168.

[23] S. Kou, Solidification and liquation cracking issues in welding, Jom. Vol. 55 2003 , pp. 37–42.

[24] N.E. Nissley, M.G. Collins, G. Guaytima, J.C. Lippold, Development of the Strain-to-Fracture Test for Evaluating Ductility-Dip Cracking in Austenitic Stainless Steels and Ni-Base Alloys, Vol. 46 2002 , pp. 32–40.

[25] J.C. Lippold, D.J. Kotecki, 6.6 Corrosion resistance, in: Welding Metallurgy and Weldability of Stainless Steels, John Wiley & Sons, Inc, New Jersey, 2005, pp. 200–211.

[26] J. Cheeke, N. David, Ultrasonics: An Overview, in: Fundamentals and Applications of Ultrasonic Waves, CRC Press, Boca Raton, 2002, pp. 1–11.

[27] SFS-EN ISO 16810 Non-destructive testing. Ultrasonic testing. General principles, 2012 , pp. 23.

[28] G. Belingardi, P. Torino, Fundamentals of Ultrasonic Phased Arrays, Solid Mechanics and Its Applications . Vol. 215 2013 , pp. 1–389.

[29] M. Mansfield, C. O'Sullivan, 12 Wave motion, in: Understanding Physics, 2011, pp. 277–305.

[30] D. Williams, The physics of ultrasound, Intensive Care / Transplantation. Vol. 13 2012 , pp. 264–268.

[31] P. Palanichamy, A. Joseph, T. Jayakumar, B. Raj, Ultrasonic velocity measurements for estimation of grain size in austenitic stainless steel, NDT & E International. Vol. 28 1995 , pp. 179–185.

[32] L. Cartz, Ultrasonic Testing, in: Nondestructive Testing, ASM International, Materials Park, OH, USA, 1995, pp. 81–126.

[33] E.I. Henneke, D. Chimenti, E. Papadakis, Fundamental Principles of Ultrasonic Wave Propagation, in: Nondestructive Testing Handbook Volume Seven Ultrasonic Testing, American Society for Nondestructive Testing, Inc., 1996, pp. 33–63.

[34] E.N. Economou, 22.2.6 Ultrasound Attenuation, in: The Physics of Solids: Essentials and Beyond, Springer, 2010, p. 635.

[35] S.P. Gornaja, N.P. Aljoshin, Attenuation of Ultrasonic Waves in Austenitic Steel Welds, Nondestr. Test. Eval. Vol. 13 1997 , pp. 149–168.

[36] D. Ensminger, L.J. Bond, Elastic Wave Propagation and Associated Phenomena, in: Ultrasonics : Fundamentals, Technologies, and Applications, Third Edition, CRC Press, Boca Raton, 2011, pp. 27–100.

[37] L. Adler, A. Jungman, P. Nagy, J. Rose, Waveform and Data Analysis Techniques, in: Nondestructive Testing Handbook Volume Seven Ultrasonic Testing, 2nd ed., American Society for Nondestructive Testing, Inc., 1996, pp. 131–186.

[38] S. Kolkoori, Chapter 5 Ray Tracing Model for Ultrasonic Wave Propagation in Inhomogeneous Anisotropic Austenitic Weld, in: Quantitative Evaluation of Ultrasonic Wave Propagation in Inhomogeneous Anisotropic Austenitic Welds Using 3D Ray Tracing Method: Numerical and Experimental Validation, Berlin, 2014, pp. 95–127.

[39] Sfs-En Iso 16828 Non-Destructive Testing . Ultrasonic Testing . Time-of-Flight Diffraction Technique As a Method for Detection and Sizing of Discontinuities (Iso, 2016.

[40] J. Cheeke, N. David, Crystal Acoustics, in: Fundamentals and Applications of Ultrasonic Waves, CRC Press, Boca Raton, 2002, pp. 175–186.

[41] E. Jr. Robert Green, Introduction to Ultrasonic Testing, in: Nondestructive Testing Handbook Volume Seven Ultrasonic Testing, 2nd ed., American Society for Nondestructive Testing, Inc., 1996, pp. 1–22.

[42] R. de Nale, C. Lebowitz, Comparison of Ultrasonics and Radiography for Weld Inspection, Review of Progress in Quantitative Nondestructive Evaluation. Vol. 8B 1988 , pp. 2003–2010.

[43] J. Krautkrämer, H. Krautkrämer, Methods and Instruments for the Ultrasonic Testing of Materials, in: Ultrasonic Testing of Materials, Springer-Verlag, New York, 1983, pp. 174–288.

[44] W.S. Lester, S. Sung-Jin, Applications of Ultrasonic Modeling, in: Ultrasonic Nondestructive Evaluation Systems, 2007, pp. 389–438.

[45] D. Ensminger, L.J. Bond, Use of Ultrasonics in the Nondestructive Testing and Evaluation of Metals, in: Ultrasonics : Fundamentals, Technologies, and

Applications, Third Edition, CRC Press, Boca Raton, 2011, pp. 305–370.

[46] T. Mansour, W. McGaughey, Ultrasonic Testing Applications in Welding, in: Nondestructive Testing Handbook Volume Seven Ultrasonic Testing, 2nd ed., American Society for Nondestructive Testing, Inc., 1996, pp. 551–568.

[47] E.A. Ginzel, Weld Inspection of Ultrasonic Inspection 2 - Training for Nondestructive Testing, web page. Available (accessed 01/2016) http://www.ndt.net/article/0498/ginz_wel/ginz_wel.htm.

[48] A. Bulavinov, M. Kröning, F. Walte, Ultrasonic Inspection of Austenitic and Dissimilar Welds, 2007 , pp. 1–13.

[49] J. Prager, J. Kitze, C. Acheroy, D. Brackrock, G. Brekow, M. Kreutzbruck, SAFT and TOFD—A Comparative Study of Two Defect Sizing Techniques on a Reactor Pressure Vessel Mock-up, Journal of Nondestructive Evaluation. Vol. 32 2012 , pp. 1–13.

[50] K. Manjula, K. Vijayarekha, B. Venkatraman, Weld Flaw detection Usig Various Ultrasonic Techniques: A Review, Journal of Applied Sciences. Vol. 14 2014 , pp. 1529–1534.

[51] Charlesworth, Engineering applications of ultrasonic time-of-flight diffraction, 2002.

[52] J. Wåle, SKI Report 2006 : 24 Crack Characterisation for In-service Inspection Planning – An Update, 2006.

[53] G. Mathers, Ultrasonic Examination: Part 2 - Job Knowledge 128, web page. Available (accessed 02/2016) http://www.twi-global.com/technical-knowledge/job-knowledge/ultrasonic-examination-part-2-128/.

[54] Sfs-En Iso 16827 Non-Destructive Testing . Ultrasonic Testing . Characterization and Sizing of Discontinuities (Iso 16827 : 2012), 2016.

[55] Sfs-En Iso 10863 Non-Destructive Testing of Welds. Ultrasonic Testing. Use of Time-of-Flight Diffraction Technique (Tofd) (Iso 10863 : 2011), 2011.

[56] Anderson, Crawford, Diaz, Prowant, Cinson, Doctor, Final Assessment of Manual Ultrasonic Examinations Applied to Detect Flaws in Primary System Dissimilar Metal Welds at North Anna Power Station, 2014.

[57] Signal-to-Noise Ratio, web page. Available (accessed 01/2016) https://www.nde-ed.org/EducationResources/CommunityCollege/Ultrasonics/Physics/signaltonoise.htm.

[58] S. Kolkoori, Quantitative Evaluation of Ultrasonic Wave Propagation in Inhomogeneous Anisotropic Austenitic Welds using 3D Ray Tracing Method: Numerical and Experimental Validation, 2014.

[59] Sfs-En Iso 22825 Non-Destructive Testing of Welds . Ultrasonic Testing . Testing of Welds in Austenitic Steels and Nickel-Based Alloys (Iso 22825 : 2012), 2016.

[60] Olympus, Ultrasonic Weld Inspection Solutions, 2015.

[61] P. Dombret, Methodology for the ultrasonic testing of austenitic stainless steel, SMIRT - 10 Post_conference Seminar 3 on NDE in Relation to Structural

Integrity. 1989.

[62] P. Mares, Simulation as a Support for Ultrasonic Testing, Journal of Modern Physics (21531196). Vol. 5 2014 , pp. 1167–1172.

[63] S.R. Kolkoori, M.-U. Rahman, P.K. Chinta, M. Ktreutzbruck, M. Rethmeier, J. Prager, Ultrasonic field profile evaluation in acoustically inhomogeneous anisotropic materials using 2D ray tracing model: Numerical and experimental comparison, Ultrasonics. Vol. 53 2013 , pp. 396–411.

[64] B. Bandawar, A. Dahasahastra, NDT Simulation Software - CIVA, Navi Mumbai, 2015.

[65] S.R. Kolkoori, P. Shokouhi, C. Hoehne, M.-U. Rahman, M. Kreutzbruck, J. Prager, A comparative study of ray tracing and CIVA simulation for ultrasonic examination of anisotropic inhomogeneous austenitic welds, in: 2013, pp. 1043–1050.

[66] CEA, Civa 2015 User Manual, CEA, 2015.

[67] The Use of Modelling in Inspection Qualification, 2011.

[68] B. Chassignole, O. Dupond, T. Fouquet, A. Le Brun, J. Moysan, P. Benoist, Application of Modelling for Enhanced Ultrasonic Inspection of Stainless Steel Welds, Welding in the World. Vol. 55 2011 , pp. 75–82.

[69] I. Aizpurua, I. Ayesta, I. Castro, Characterization of anisotropic weld structure for nuclear industry, in: 2014, pp. 1–13.

[70] V. Dorval, F. Jenson, G. Corneloup, J. Moysan, A.G. Berger, Accounting for Structural Noise and Attenuation in the Modeling of the Ultrasonic Testing of Polycrystalline Materials, Vol. 29 2015 , pp. 1887–1894.

[71] M. Kemppainen, I. Virkkunen, Crack characteristics and their importance to NDE, Journal of Nondestructive Evaluation. Vol. 30 2011 , pp. 143–157.

[72] EPRI, Abstract, in: Nondestructive Evaluation: Recommendations for Single Sided UT Examinations of Austenitic Stainless Steel Piping Welds, 2009.

[73] A. Koskinen, E. Leskelä, Comparison of Artificial flaws in Austenitic Steel Welds with NDE Methods, Espoo, VTT Technical Research Centre of Finland, 2014.

[74] International Atomic Energy Agency, Guidebook for the Fabrication of Non-Destructive Testing (NDT) Test Specimens, Iaea-Tecdoc-Tcs-13. 2001.

[75] M. Kemppainen, I. Virkkunen, J. Pitkänen, R. Paussu, H. Hänninen, Comparison of Realistic Artificial Cracks and In-Service Cracks, in: 8th ECNDT, Barcelona, 2002.

[76] F.C. Campbell, Fatigue of Metals, in: Fatigue and Fracture: Understanding the Basics, ASM International, Materials Park, OH, USA, 2012, pp. 147–208.

[77] M. Kemppainen, I. Virkkunen, J. Pitkänen, R. Paussu, H. Hänninen, Advanced flaw production method for in-service inspection qualification mock-ups, Nuclear Engineering and Design. Vol. 224 2003 , pp. 105–117.

[78] P.J. Herman, Manufacturing NDT Reference Standards, The NDT Technician. 2005 , pp. 1–4.

[79] X.E. Gros, 3.12 Performance Assessment of NDT Methods Page, in: NDT Data Fusion, Hanser Publishers, 1997, pp. 73–81.

[80] J.H. Kurz, A. Jüngert, S. Dugan, G. Dobmann, C. Boller, Reliability considerations of NDT by probability of detection (POD) determination using ultrasound phased array, Engineering Failure Analysis. Vol. 35 2013 , pp. 609–617.

[81] G.A. Georgiou, Probability of Detection (PoD) curves: Derivation, applications and limitations, London, 2006.

[82] M. Carboni, S. Cantini, Advanced ultrasonic "probability of detection" curves for designing in-service inspection intervals, International Journal of Fatigue. 2015 , pp. 1–11.

[83] C. Müller, M. Elaguine, C. Bellon, U. Ewert, U. Zscherpel, M. Scharmach, et al., POD (Probability of Detection) Evaluation of NDT Techniques for Cu-Canisters for Risk Assessment of Nuclear Waste Encapsulation, Ecndt. 2006 , pp. 1–22.

[84] J. Berlanger, F. Laprise, Procedure for Encoded, Manually Driven, Phased Array Ultrasonic Flaw Detection and Length Sizing in Ferritic and Wrought Austenitic Piping Welds Document: Zetec_OmniScanPA_01_revC.doc, 2006.

[85] S. Bannouf, D. Elbaz, B. Chassignole, N. Leymarie, P. Recolin, Validation of simulation tools for ultrasonic inspection of austenitic welds in the framework of the MOSAICS project, 2014.

[86] T. Grünberger, R. Domröse, Direct Metal Laser Sintering, Laser Technik Journal. Vol. 12 2015 , pp. 45–48.

APPENDIX A: EQUATION CLARIFICATION

Log-logistic hit/miss

$$POD(a) = \frac{e^{\frac{\pi}{\sqrt{3}}(\frac{\ln a - m}{\sigma})}}{1+e^{\frac{\pi}{\sqrt{3}}(\frac{\ln a - m}{\sigma})}} \tag{A.1}$$

Where:

$$m = -\frac{\alpha}{\beta} \tag{A.2}$$

And

$$\sigma = \frac{\pi}{\beta\sqrt{3}} \tag{A.3}$$

Which leads to:

$$\frac{\pi(\ln a + \frac{\alpha}{\beta})}{\sqrt{3}\frac{\pi}{\beta\sqrt{3}}} = \frac{(\ln a + \frac{\alpha}{\beta})}{\frac{1}{\beta}} = \beta \ln a + \alpha \tag{A.4}$$

Thus:

$$POD(a) = \frac{e^{(\alpha+\beta \ln a)}}{1+e^{(\alpha+\beta \ln a)}} \tag{A.5}$$

Probability related to size of the flaw

p=POD(a)

$$p\left(1 + e^{\alpha+\beta \ln a}\right) = e^{\alpha+\beta \ln a}$$

$$\therefore p = e^{\alpha+\beta \ln a}(1-p)$$

$$\therefore \frac{p}{1-p} = e^{\alpha+\beta \ln a}$$

$$\therefore \ln(\frac{p}{1-p}) = \alpha + \beta \ln a$$

$$\therefore \ln(odds) \propto \ln a \tag{A.6}$$

Signal response approach:

F is the cumulative log-normal distribution

$$POD(a) = 1 - F\left\{\frac{\ln(a_{th}) - [\alpha + \beta \ln(a)]}{\sigma_\gamma}\right\}$$

$$= F\left\{\frac{\ln(a) - \left[\frac{ln\, a_{th} - \alpha}{\beta}\right]}{\frac{\sigma_\gamma}{\beta}}\right\} \quad \text{(A.7)}$$

Where:

$$\mu = \frac{\ln(a_{th}) - \alpha}{\beta} \quad \text{(A.8)}$$

and

$$\sigma = \frac{\sigma_\gamma}{\beta} \quad \text{(A.9)}$$

thus

$$POD(a) = F\left[\frac{\ln(a) - \mu}{\sigma}\right] \quad \text{(A.10)}$$

APPENDIX B: RESULTS

Table 6 Summary of the results, gain and maximum amplitude (%)

Probe	2,25 MHz PA 40-75°	5 MHz PA 40-75°	2 MHz MWB 45° N2	2 MHz MWB 60° N2	1,5 MHz TRL PA 40-70°
Gain (dB)	8	8	35	35	33
Soft Gain (dB)	0	0	0	1,5	0
Tot. Gain (dB)	8	8	35	36,5	33
1a amplitude (%)	27,93	13,20	27,20	35,83	75,03
2a amplitude (%)	75,27	67,05	85,10	59,37	75,13
3a amplitude (%)	34,67	19,20	34,10	33,20	74,50
4a amplitude (%)	18,67	10,47	19,50	35,03	61,03
5a amplitude (%)	82,10	78,33	78,43	71,37	81,03
1b amplitude (%)	21,30	13,17	33,73	35,70	67,43
2b amplitude (%)	11,53	6,83	15,83	18,17	59,87
3b amplitude (%)	16,23	11,00	16,33	30,43	55,93
4b amplitude (%)	23,23	13,03	30,73	47,20	72,40
5b amplitude (%)	81,33	73,83	75,30	77,50	75,53

Table 7 Summary of the results, Signal-to-Noise ratio (SNR)

Probe	2,25 MHz PA 40-75°	5 MHz PA 40-75°	2 MHz MWB 45° N2	2 MHz MWB 60° N2	1,5 MHz TRL PA 40-70°
1a SNR	3,88	3,07	2,00	2,38	1,99
2a SNR	10,45	15,59	6,27	3,95	2,00
3a SNR	4,81	4,47	2,51	2,21	1,98
4a SNR	2,59	2,43	1,44	2,33	1,62
1b SNR	2,12	1,58	2,39	2,37	1,79
2b SNR	1,15	0,82	1,12	1,21	1,59
3b SNR	1,61	1,32	1,16	2,02	1,49
4b SNR	2,31	1,56	2,17	3,14	1,92

Average noise level was measured between the flaws number 1 and 2. Maximum amplitude between the flaws was considered noise if the echo dynamics of the amplitude proved the amplitude as noise and not a random amplitude peak. As for the maximum amplitudes the average noise level is the average of three measurements. The average noise levels are in Table 8.

Table 8 Average noise levels

Probe	2,25 MHz PA 40-75°	5 MHz PA 40-75°	2 MHz MWB 45° N2	2 MHz MWB 60° N2	1,5 MHz TRL PA 40-70°
Average noise (%)	8,63	6,32	13,85	15,03	37,63

In Table 9 there is a comparison matrix between the techniques used in this thesis. The signal-to-noise ratios (SNR) of the probes were compared to each other for each flaw. The highest SNR for a flaw was evaluated to 4 points and the lowest was evaluated as 0 points. Then the points were summed together and the highest score would represent the highest overall SNR between the used techniques.

Table 9 SNR comparison matrix

	2,25 MHz PA 40-75°	5 MHz PA 40-75°	2 MHz MWB 45° N2	2 MHz MWB 60° N2	1,5 MHz TRL PA 40-70°
4a	4	3	0	2	1
3a	4	3	2	1	0
2a	3	4	2	1	0
1a	4	3	1	2	0
4b	3	0	2	4	1
3b	3	1	0	4	2
2b	2	0	1	3	4
1b	2	0	4	3	1
tot.	25	14	12	20	9